

الجمهورية الجزائرية الديمقراطية الشعبية
République Algérienne Démocratique et Populaire
وزارة التعليم العالي والبحث العلمي

Ministère de l'Enseignement Supérieur et de la Recherche Scientifique

Université Mohamed Khider – Biskra

Faculté des Sciences et de la Technologie

Département : Génie Mécanique

Ref :.....



جامعة محمد خيضر بسكرة

كلية العلوم والتكنولوجيا

قسم: الهندسة الميكانيكية

المرجع:

Thèse présentée en vue de l'obtention
du diplôme de

Doctorat en Sciences en : Génie Mécanique

**Effet Des Traitements Thermiques sur Les
Propriétés Mécaniques et la Résistance à La
Corrosion D'un Acier Inoxydable Duplex**

Présentée par :
BERGUIGA Talha

Soutenu publiquement le 29-Septembre-2020 devant le jury composé de :

Mr. ZIDANI Mosbah	Professeur	Président	Université de Biskra
Mr. BOUMERZOUG Zakaria	Professeur	Rapporteur	Université de Biskra
Mr. NESSARK Belkacem	Professeur	Examineur	Université de Sétif
Mr. DIHA Abedallah	Maitre de conférence	Examineur	Université de Tébessa

Remerciements

Je remercie tout d'abord Allah le tout puissant, de m avoir donné le courage et la patience afin de mener à bien ma thèse de doctorat.

J'exprime ma profonde gratitude à mon Directeur de thèse, Monsieur BOUMERZOUG Zakaria Professeur à l'université de Biskra; d'avoir accepté de m'encadrer, de m'aider durant toutes ces années. Je lui suis reconnaissant pour le temps conséquent qu'il m'a accordé, pour l'encadrement, la transmission de son savoir, mais également pour les différentes conversations professionnelles. Je salue sa patience et son aide tout au long de cette thèse.

J'adresse mes vifs remerciements à Monsieur ZIDANI Mosbah, Professeur à l'université de Biskra, qui m'a fait l'honneur de présider le jury de thèse et de juger mon travail.

Je tiens aussi à remercier tous les membres de jury pour avoir accepté d'évaluer mon travail et aussi pour leurs remarques enrichissantes. Merci donc à Monsieur *NESSARK Belkacem*, Professeur à l'université de Sétif, et merci à Monsieur DIHA Abedallah Maître de conférences à l'université de Tébessa.

Je tiens à remercier également tous les responsables et personnels du laboratoire de Génie mécanique, laboratoire de chimie industrielle et du laboratoire des rayons X au sein de la faculté des sciences et technologie à l'université de Biskra.

Mes sincères remerciements s'adressent également à Monsieur Lanez Touhami, Professeur à l'université de El-Oued, pour avoir accepté m'accueillir au sien de son laboratoire pour réaliser les essais de corrosion.

Mes remerciements à tous ceux qui ont contribué à ma formation depuis mon jeune âge et aux enseignants de l'École Nationale Polytechnique d'Alger et de l'université de Biskra.

Enfin, je remercie tous les membres de ma famille, et en particulier mes parents, pour leurs soutiens durant la thèse et sur l'ensemble de mon parcours universitaire. Je n'aurai jamais pu arriver jusque-là sans leurs encouragements.

BERGUIGA Talha

Table of Contents

General Introduction	1
----------------------------	---

Chapter I: Literature Review

1. General Introduction to Stainless Steels.....	4
1.1 Introduction and Historical developments.....	4
1.2 Classification of Stainless Steels	5
1.2.1 Ferritic stainless steel	6
1.2.2 Martensitic and precipitation hardening stainless steel	7
1.2.3 Austenitic stainless steel.....	7
1.2.4 Duplex stainless steel	7
1.3 Production of Stainless Steels	7
2. Duplex stainless steel	9
2.1 A brief history	9
2.2 Modern Development of DSS:	10
2.3 Mechanical proprieties of DSS:.....	11
2.4 Physical proprieties of DSS.....	13
2.5 Pitting Resistance Equivalent number PRE_N :.....	13
2.6 Applications of DSS	14
2.7 Limit of use of DSS:.....	15
2.8 Chemical composition: effect of main alloying elements:	16
2.9 Effects of alloying elements on phase balance.....	21
3. Precipitation of secondary phases.....	24
3.1 Secondary austenite (γ_2)	26
3.2 Chi (χ) phase.....	27
3.3 Chromium nitrides (CrN/Cr_2N).....	28
3.4 R-phase.....	28

3.5	Π-phase.....	29
3.6	τ-phase.....	29
3.7	Carbides $M_{23}C_6$ and M_7C_3	29
4.	Sigma phase precipitation:	29
4.1	Development Progress of the σ Phase:.....	29
4.2	Precipitation Characteristic of the σ Phase:.....	30
4.3	Isothermal Kinetics Modeling of Sigma Phase Formation.....	33
4.1	Effect of the σ Phase on the Properties of Duplex Stainless Steels.....	36
5.	Alpha Prime (α') phase	38
5.1	Spinodal decomposition and nucleation – growth mechanism:	39
5.2	Activation energy of ferrite spinodal decomposition:	41
6.	Solution annealing heat treatment:.....	42
7.	Pitting corrosion properties.....	43
7.1	Mechanism and Stages of Pitting Corrosion	44
7.2	Pitting potential	45
7.3	Relationship between E_p and $PREN$:	47
7.4	Effect of secondary phases on pitting potential:.....	49

Chapter II: Experimental Techniques

1.	Introduction:.....	52
2.	Material presentation:.....	52
2.1	Chemical composition.....	53
2.2	Mechanical characteristics.....	54
3.	Heat Treatment (Aging) program:	54
4.	Metallographic examinations	55
5.	Microhardness Measurements	56
6.	X-ray diffraction analysis	58
7.	Scanning electron microscopy (SEM).....	59

8. Differential Scanning Calorimetry (DSC)	61
9. Corrosion Tests and pitting potential measurement:	64
9.1 Potentiodynamic polarization:.....	64
9.2 Scan rate:.....	66
9.3 Test Solution:.....	66
9.4 Sample identification.....	67
9.5 Pitting potential determination method.....	67

Chapter III: Results and Discussions

1. Introduction	68
2. Characterization of the investigated material at the as received condition	69
2.1 Metallographic examination.....	69
2.2 Estimation of phase fraction.....	69
2.3 XRD analysis of solution treated DSS sample.....	69
3. Aging treatments at 850°C and Sigma (σ) phase characterization	70
3.1 Sigma phase formation process.....	71
3.2 SEM observations of Sigma phase.....	72
3.3 Effect of holding time on sigma (σ) evolution.....	74
3.3.1 Metallography of aged samples.....	74
3.3.2 Quantitative analysis of sigma phase.....	75
3.3.3 Application of the classical Johnson-Mehl-Avrami (JMA) Analysis for sigma phase.....	76
3.3.4 Comparison of experimental data and the classical JMA analysis for sigma volume fraction.....	79
3.3.5 Application of the modified JMA analysis model.....	80
3.3.6 XRD analysis of aged samples.....	84
4. DSC analysis Results	85
4.1 Study of "475 °C Embrittlement" by DSC analysis.....	85
4.2 Activation Energy calculation.....	88

4.3	Kinetic of embrittlement and End of life prediction.....	92
5. Corrosion Tests		97
5.1	Potentiodynamic polarization results of solution treated sample (in the as received condition) 97	
5.1.1	Simulated seawater solution	97
5.1.2	Produced water solution	98
5.2	Potentiodynamic polarization results of aged sample	99
5.2.1	Simulated seawater solution:.....	99
5.2.2	Produced water solution	100
5.3	Engineering significance of pitting potentials in the aged samples.....	103
5.4	Pitting morphology and its relation to sigma phase	105
6. Impact of sigma phase on hardness		107
General Conclusions and Future Works.....		108
References.....		111
Annex A (Miscellaneous information on the metallography of DSS).....		124

List of Figures

Figure Number	Title	Page
I.1	Composition and property linkages in the stainless steel family of alloys.	6
I.2	Stainless steel manufacturing routes.	9
I.3	Comparison of typical yield strength of duplex stainless steels and Type 316L between room temperature and 300°C (572°F).	12
I.4	Effect of alloying elements on passive range.	17
I.5	The Fe–Cr equilibrium diagram.	18
I.6	Schematic TTP, time-to-precipitation, diagram for duplex stainless steels with secondary phases and influence of alloying elements.	18
I.7	Effect of carbon on the Fe–Cr diagram: (a) 0.05C wt%.	21
I.8	Schaeffler diagram illustrating the Stainless Steels families positions.	22
I.9	Intermetallic phase precipitations for UNS S31803 DSS.	24
I.10	Section through the Fe-Cr-Ni ternary phase diagram at 68% iron	26
I.11	Chi phase precipitation in DSS.	28
I.12	Schematic diagram of the σ phase precipitation.	32
I.13	Precipitation mechanism of the σ phase in UNS S31803 stainless steel.	33
I.14	Time-Temperature Transformation diagram for alloy S32404.	38
I.15	Fe–Cr binary phase diagram.	39
I.16	Formation of precipitates by a classical mechanism of nucleation and growth or by spinodal decomposition.	40
I.17	Example of a solution annealing cycle. The critical temperature ranges are strongly dependent on the steel grade.	43
I.18	Schematic diagram of the role of pitting.	44
I.19	Typical schematic for pitting corrosion process.	45
I.20	Schematic polarization curve for a stainless steel in a sulphuric acid solution.	47
I.21	Relationship between E_p & PREN.	48
II.1	Flow Diagram for Stainless Steel Materials Selection for Process Piping.	53
II.2	Some definitions from the stress strain curve.	54
II.3	Scheme of applied aging treatment.	55
II.4	Schematic for electrolytic etching cell.	56
II.5	Vickers Microhardness test principle.	57
II.6	Microhardness apparatus.	57
II.7	Schematic illustration of Bragg condition and Bragg's law.	58
II.8	Bruker D8- Advanced diffractometer.	59
II.9	Schematic diagram of major components of SEM.	60
II.10	Schematic illustration of power compensation DSC.	62
II.11	Schematic illustration of heat-flux DSC cell. R and S refer to reference and sample pans.	62
II.12	Typical DSC signal for a Low Alloy Steel.	63
II.13	Photograph of the DSC Q20 used in this study.	63

Figure Number	Title	Page
II.14	Principle of determination of pitting Potential (E_p).	64
II.15	Schematic of the electrochemical cell used for corrosion testing.	65
II.16	The VOLTALAB PGZ-301 potentiostat.	66
III.1	Micrograph of the investigated metal at the as received state.	69
III.2	X-Ray diffraction pattern of the studied material in the as received condition.	70
III.3	Optical microstructure corresponding to the aged specimen at 850°C for 5 min.	71
III.4	SEM micrograph corresponding to the aged specimen at 850 °C for 360 min.	73
III.5	SEM micrograph corresponding to the aged specimen at 850 °C for 360 min, Morphology of secondary austenite (γ_2) and sigma phase.	74
III.6	Optical micrographs showing the aged specimens at 850°C for (a) 5 min, (b) 60min and (c) 360min.	75
III.7	Variation of the volume fraction of sigma phase in UNS S31803 as a function of aging time at 850 °C.	76
III.8	Application of the classical JMA model for sigma phase formation mechanism in at 850°C.	77
III.9	Comparison between experimental data and the classical JMA analysis of sigma volume fraction during aging at 850°C.	80
III.10	Application of the modified JMA model to the sigma phase precipitation during aging at 850 °C.	82
III.11	Comparison between experimental data and the modified JMA analysis of sigma volume fraction during aging at 850°C.	83
III.12	X-Ray diffraction patterns of samples aged at 850°C.	84
III.13	DSC curve of heating measurement duplex stainless steel. Heating rate 30°C/min.	86
III.14	Fe–Cr binary phase diagram.	87
III.15	DSC curves of heating measurement duplex stainless steel. Heating rate 30, 40 and 60°C/min.	89
III.16	Plot of $\ln(T_p^2/S)$ as function of $1/T_p$.	90
III.17	Predicted Microhardness surface for aged 2205 DSS grade.	95
III.18	Potentiodynamic polarization curves for the solution treated sample in simulated seawater solution.	98
III.19	Potentiodynamic polarization curves for the solution treated sample in Produced water solution.	98
III.20	Potentiodynamic polarization curves for the aged samples at 850°C in for different times in simulated seawater solution.	99
III.21	Potentiodynamic polarization curves for the aged samples at 850°C in for different times in Produced Water solution.	101
III.22	E_p as a function of sigma volume fraction (%).	102
III.23	Potential diagram for Lean Duplex SS (LDX 2101) at the different selected potentials.	104
III.24	SEM images of pitted samples (a) and (b) solution treated sample, (c) and (d) aged samples for 60 min at 850°C.	106
III.25	Microhardness evolution as a function of aging time at 850°C for the studied DSS (UNS S31803).	107

Figure Number	Title	Page
A.1	Optical micrograph of DSS at solution treated condition, after electrochemical etching is with a 32 N KOH.	125
A.2	Optical micrograph corresponding to a longitudinal section of aged DSS at 850°C for 2h, electrolytically etched in 30% KOH solutions.	125
A.3	Micro-section showing sigma phase precipitates in a super DSS fitting.	126
A.4	Scanning electron micrographs showing σ phase located at the δ/γ interface.	126
A.5	SEM micrographs of the DSS after aging at 750 °C for 1 h.	127
A.6	SEM micrograph of HAZ solution treated at 1150 °C for 1 h then aged at 850 °C for 3 h.	127
A.7	Typical pitting morphologies of UNS S31803 DSS after polarization at 0.6M NaCl solution, aged for 6h@750°C.	128
A.8	Pit morphology of DSS 2205 after corrosion test in 0.1 M NaCl + 0.01 M MoO_4^{-2} at 80°C.	128

List of Tables

Table Number	Title	Page
I.1	Chemical composition in wt. % of wrought Duplex Stainless Steel grades with the corresponding Unified Numbering System and European Norm.	11
I.2	Minimum ASTM and EN mechanical property limits for duplex stainless steel plate.	12
I.3	Ambient temperature physical properties of duplex stainless steels compared with carbon steel and austenitic stainless steels.	13
I.4	Upper temperature limits for duplex stainless steel for maximum allowable stress values in pressure vessel design codes.	16
I.5	Observed intermetallic phases in DSS.	25
I.6	Chemical composition and lattice constant of the σ phase.	31
I.7	Some failure cases involving sigma phase precipitation, from [FAR 19].	36
II.1	Chemical composition of the studied Material.	53
II.2	The mechanical characteristics of the investigated DSS.	54
II.3	Chemical Analysis of Produced Water.	67
II.4	Specimens identification.	67
III.1	Summary of detected peaks in solution treated DSS sample.	70
III.2	Values of n and k Parameter from J-M-A Calculations.	78
III.3	value of Avrami exponent (n) obtained in previous works.	79
III.4	Kinetic parameters of the modified JMA model.	82
III.5	Previous works using the modified JMA model for sigma precipitation kinetic.	83
III.6	Summary of calculated diffraction peaks.	84
III.7	Activation energies and k_0 values characterizing the phase transformation processes of the DSS grade in the temperature range 300 and 525°C.	90
III.8	Activation Energy of separation process as measured during previous works.	91
III.9	KJMA parameters for hardness prediction during embrittlement.	94
III.10	Hardness prediction at 280°C and 315°C during service life.	95
III.11	Pitting potentials for the tested samples in Simulated seawater.	99
III.12	Pitting potentials for the tested samples in Produced Water.	102
III.13	Matrix of acceptable and unacceptable pitting potentials at 25°C based on the concept of Engineering diagrams.	105
A.1	Recommended etchants for duplex stainless steels and their applications.	124

Nomenclature and Abbreviations

γ	Austenite
γ_2	Secondary Austenite
AOD	Argon Oxygen Decarburization
c	Impingement Exponent
χ	Chi Phase
CPT	Critical Pitting Potential
C_{req}	Chromium Equivalent
δ	Ferrite
DSC	Differential Scanning Calorimetry
DSS	Duplex Stainless Steel
EAF	Electric-Arc Furnace
E_p	Pitting Potential
HAZ	Heat-Affected Zone
JMA	Johnson-Mehl-Avrami
k_0	Pre-Exponential Factor
n	JMA Exponent
Ni_{eq}	Nickel Equivalent
<i>PREN</i>	Pitting Resistance Equivalent Number
Q	Activation Energy (J/mol)
R	Gas Constant
σ	Sigma Phase
σ_{eq}	Sigma Equivalent
S	Heating Rate
SCC	Stress Corrosion Cracking
SCE	Saturated Calomel Electrode
SEM	Scanning Electron Microscopy
TEM	Transmission Electron Microscopy
T_p	Peak Temperature (K)
wt. %	concentration in weight percent
XRD	X Ray Diffraction

General Introduction

Duplex stainless steels (DSS) are Fe-Cr-Ni alloys having an approximately volumetric fraction of 50% ferrite and 50% austenite in their microstructures . DSS combine some characteristics of each of these phases. They have been introduced into the market during 1930s; since that time there has been an accentuated development and rapid spreading of their use.

They have been widely used in various industrial sectors due to their higher strength, better weldability, and higher resistance to stress corrosion and pitting . Hence, DSS are attractive material for applications where these properties are desired like in off-shore industries, food industries, chemical industries, paper industries, nuclear industries and in structural applications as well . In particular, the UNS S31803 alloy (also known as steel SAF 2205) is the most widely employed duplex stainless steels nowadays. This material grade found widespread use in oil and gas industry, especially for high chloride containing process fluids like oily produced water and injection process systems. The superior properties of the duplex stainless steels come primarily from approximately equivalent amounts of austenite (γ) and δ -ferrite .

However, the use of DSS at high temperature is a typical concern to users of duplex stainless steels owing to their susceptibility to the formation of dangerous intermetallic phases, such as σ - and χ -phase, which form after ageing the material in a temperature range over 600°C. Furthermore, DSS components are generally subject to thermal embrittlement which takes place at intermediate temperatures (\sim 475°C) via α - α' phase separation . Therefore, the use of duplex stainless steels has been usually limited to temperatures not exceeding approximately 500 °C. For instance, according to ASME B31.3 Process Piping Code, the limit of use of UNS31803 Duplex stainless steel grade is 315°C.

It is supposed that among intermetallic precipitates, Sigma phase is the most detrimental one, as it causes a considerable drop in toughness as well as corrosion resistance . Even small amounts of sigma phase influence the resistance against most corrosion forms such as pitting, sulfide stress corrosion cracking, intergranular corrosion and hydrogen embrittlement. Consequently, the standard criterion is that no sigma phase is allowed in produced duplex materials. Sigma phase is a Cr-Mo rich hard precipitate which occurs at temperatures between

600-1000°C . The fastest sigma phase precipitation kinetics occurs at 850°C. Once sigma phase is introduced in the microstructure it is difficult to recover the optimum microstructure . The detrimental effect of sigma phase on corrosion resistance was usually associated to the formation of Cr- Mo depleted regions adjacent to sigma phase as a consequence of the eutectoid mechanism generating sigma phase. Concentration can fall below the minimum 12wt.% to 13wt.% of chromium required to ensure the passivation process. Regions with quantities below the minimum Cr range undergo active dissolution and usually corrode at rates close to those of carbon steel and pure iron .

From a practical standpoint, sigma phase precipitation can be encountered during the welding process if the cooling rate from 1200 to 800°C is too slow. This usually occurs because either the heat input is too great or the interpass temperature is too high. Incorrectly heat treated DSS may also suffer from sigma phase precipitation. Even though strict specifications and qualification tests are usually required for such grades, the delivery of "*Sigmatized*" (aged) duplex stainless steel components still occurs at times .Recently, it was reported that there have been a large number of sigmatized DSS fittings that were delivered and installed in several projects related to offshore production facilities .

Numerous studies have been published about the impact of sigma phase on the corrosion resistance. However, most of the available studies have been conducted using a various electrochemical tests in chloride containing solutions (NaCl, CaCl₂,...). On the other hand there is no published studies examining the electrochemical behavior of sigmatized DSS when exposed to oil and gas field environment. There have been only a limited number of studies related to Super Duplex stainless steel (SDSS) materials tested in a simulated oil field environment. Also the amount of literature on the seawater pitting of aged DSS is limited, more specifically in term of correlation between sigma phase content and pitting potential values.

Given the above facts, and knowing that most of Oil and Gas companies base their materials selection on field experience data coupled with laboratory tests, this research work was mainly conducted to contribute to enhance the understanding of corrosion behavior of sigmatized DSS in oil field environments. Therefore the investigated materials were exposed to two different chloride containing environments: simulated seawater solution and produced water solution. It is expected from this study to show the relationship between sigma phase content and pitting potential values. The sigmatized samples were obtained by aging treatment at 850°C during various holding times to introduce varied levels of sigma phase. Therefore, as

part of this study, the microstructural evolution after ageing and the effect of sigma phase on the hardness behaviour were also investigated.

The kinetic of embrittlement process associated with α - α' phase separation was also investigated in the current study using DSC technique coupled with Kissinger analysis. Again, according to our literature survey, there is no published work up to date investigating the kinetic of thermal embrittlement of DSS via DSC technique. The obtained activation energy governing the embrittlement process has been compared with the results of some previous works as demonstrated on Chapter III. This activation energy has been used as "Prediction Tool" through the JMA model to estimate the end of life of DSS components operating at intermediate temperatures.

This thesis is structured in three (03) Chapters and General Conclusions as follows:

- In chapter I, we have introduced briefly the stainless steel families then we have given more care on the Duplex stainless steels and related concerns and more specially the issue of sigma phase precipitation and its resulting effects on mechanical and corrosion behaviour. Some definitions, prediction equations and models are also provided in order to support Chapter III.
- Chapter II, is aimed to detail the investigated material grade in this study and the used technical procedure of characterizations.
- In Chapter III, we have presented our findings with some explanations and comparison with previous works documented in literature where necessary.

And finally, concluding remarks and suggestions for future works are given on last part.



Literature Review

1. General Introduction to Stainless Steels

1.1 Introduction and Historical developments

STAINLESS STEELS are iron-base alloys that contain a minimum of about 12% Cr, the amount needed to prevent the formation of rust in unpolluted atmospheres (hence the designation stainless). Few stainless steels contain more than 30% Cr or less than 50% iron. They achieve their stainless characteristics through the formation of an invisible and adherent chromium-rich oxide film. This oxide forms and heals itself in the presence of oxygen. [ASM 00].

The history of stainless steels starts around 1910, in Germany with Friedrich Krupp AG and in England with Thomas Firth & Sons [ARO 10, STE 13]. But the scientific background was started as early as 1821 in France; where the French mineralogist Berthier reported about Cr-steels resistance to acid attack. The situation was for some time obscured by the famous English metallurgist Robert Hadfield who reported in 1892 that Cr was not beneficial for the corrosion resistance. He based this statement on tests in 50 % sulphuric acid. In 1911 Monnartz published a thorough article on Fe-Cr-alloys and specially their acid-resistance and pointed out that the results from traditional testing with sulphuric acid could not be generalized. He was also the first to point out the beneficial effect of Mo on the corrosion resistance of Cr-steel[OUT 13].

At the same time in Sheffield, England, Brearley was experimenting with 12–14 % Cr steels and observed that they did not etch in normal etching acids. He also noticed that Cr steels resisted corrosion much better in the hardened than in the annealed condition. Brearley saw

commercial possibilities of this material in cutlery and gave non-rusting steel the name Stainless Steel [OUT 13].

The earliest stainless steel grades were martensitic and ferritic Fe-Cr steels, but quite soon the austenitic Fe-Cr-Ni steels became the largest group. The first reference for duplex stainless steel group appears in 1927, when Bain and Griffith' published data on ferritic -austenitic structures [GUN 03].

1.2 Classification of Stainless Steels

Historically, stainless steels have been classified by microstructure and are described as austenitic, martensitic, ferritic, or duplex (austenitic plus ferritic). In addition, a fifth family, the precipitation- hardenable (PH) stainless steels, is based on the type of heat treatment used rather than the microstructure [ASM 00].

Figure I.1 provides a useful summary of some of the compositional and property linkages in the stainless steel family.

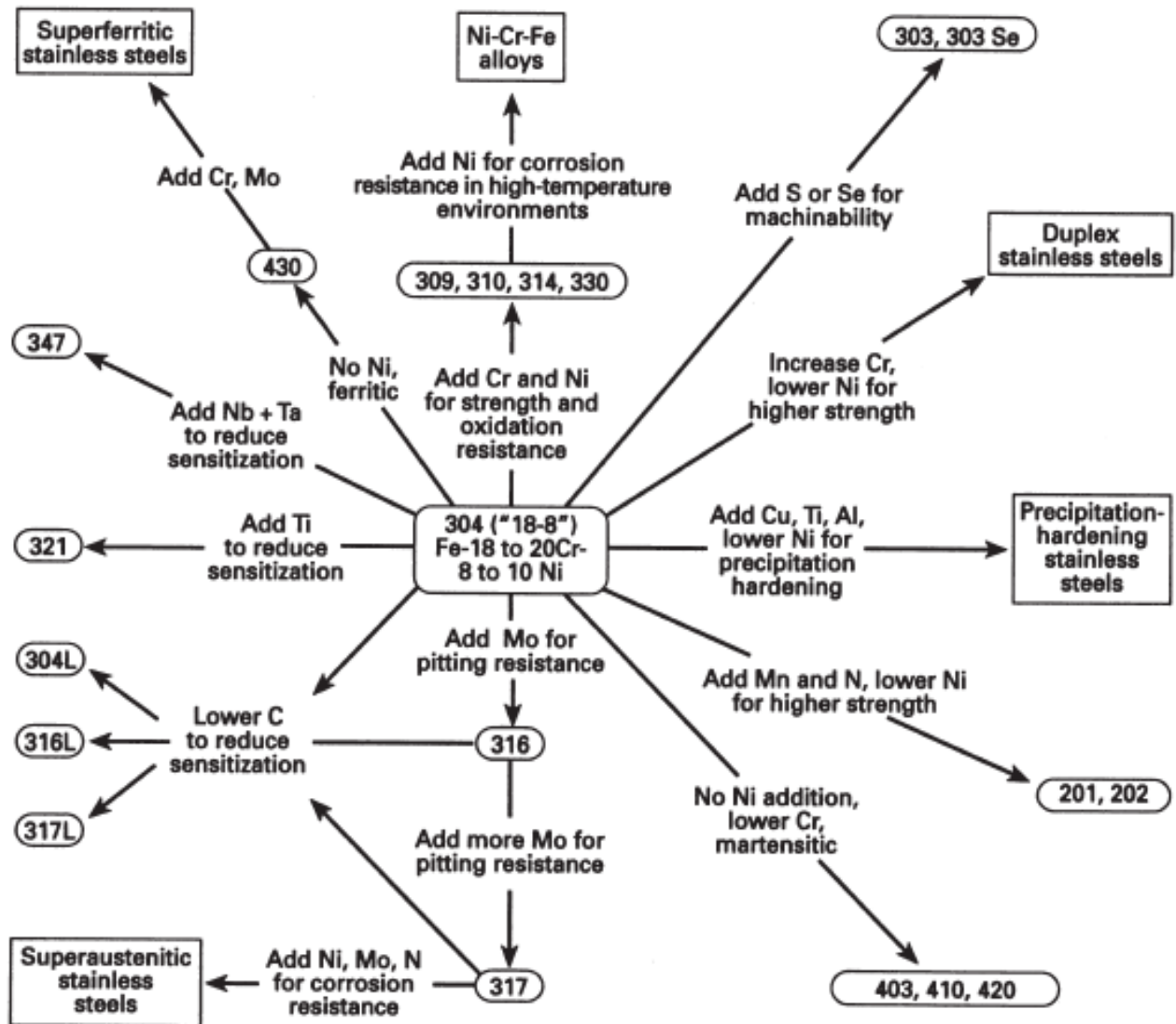


Figure I.1: Composition and property linkages in the stainless steel family of alloys [ASM 00].

1.2.1 Ferritic stainless steel

The standard ferritic grades are alloyed with chromium (11.2–19 %), but with no, or very small addition of nickel. As nickel is one of the most expensive alloying elements and has demonstrated high price volatility, the low nickel content of the ferritic grades make them more price stable compared to grades with high nickel content.

Molybdenum is added to some grades to improve the corrosion resistance, while alloying with niobium and/or titanium improves the weldability [OUT 13].

1.2.2 Martensitic and precipitation hardening stainless steel

The martensitic grades are the smallest group of stainless steel. To improve the strength and hardenability of the martensitic grades they have higher carbon content compared to other grades, and nitrogen is sometimes added to further improve the strength. These grades contain no or rather small amounts of nickel, and molybdenum is seldom added. By adding some nickel and reducing the carbon content the rather poor weldability of martensitic grades can be improved. Sometimes sulphur is added to improve the machinability. The martensitic grades are magnetic and hardenable.

The precipitation hardening grades are hardened by a special mechanism involving the formation of precipitates within the microstructure [OUT 13].

1.2.3 Austenitic stainless steel

The austenitic grades are the largest group of stainless steels, and can be divided into five sub-groups, Cr-Mn grades, Cr-Ni grades, Cr-Ni-Mo grades, high performance austenitic grades and high temperature austenitic grades. The austenitic grades have good, to excellent corrosion resistance, good formability and weldability.

Their good impact strength at low temperatures is often exploited in cryogenic applications. The austenitic grades are non-magnetic in the solution annealed condition due to the austenitic microstructure [OUT 13].

1.2.4 Duplex stainless steel

Duplex stainless steels have a mixed structure of austenite and ferrite and typically contain chromium (20 – 25 wt%) and nickel (1.5 – 7 wt%) as the main alloying elements [ASM 05]. Further details on this alloy grade are provided on **Section 2**, as the instigated steel in the current work is belonging to duplex stainless steels family.

1.3 Production of Stainless Steels

With specific restrictions in certain types, the stainless steels can be shaped and fabricated in conventional ways. They are produced in cast, powder metallurgy (P/M), and wrought forms.

Available wrought product forms include plate, sheet, strip, foil, bar, wire, semi-finished products (blooms, billets, and slabs), and pipe and tubing. Cold rolled flat products (sheet, strip, and plate) account for more than 60% of stainless steel product forms.

Figure I.2 illustrates the most commonly employed mill processes for making various wrought stainless steel products.

Production of stainless steels is a two-stage process involving the melting of scrap and ferroalloys in an electric-arc furnace (EAF) followed by refining by argon oxygen decarburization (AOD) to adjust the carbon content and remove impurities. Alternative, melting and refining steps include vacuum induction melting, vacuum arc remelting, electroslag remelting, and electron beam melting.

Melting and refining of stainless steels is, however, most frequently accomplished by the EAF/AOD processing route. In fact, about 90% of all stainless steel produced in the United States is processed by EAF melting followed by AOD.

During the final stages of producing basic mill forms—sheet, strip, plate and bar—and bringing these forms to specific size and tolerances, the materials are subjected to hot reduction with or without subsequent cold rolling operations, annealing, and cleaning. Further steps are required to produce other mill forms, such as wire and tube [ASM 00].

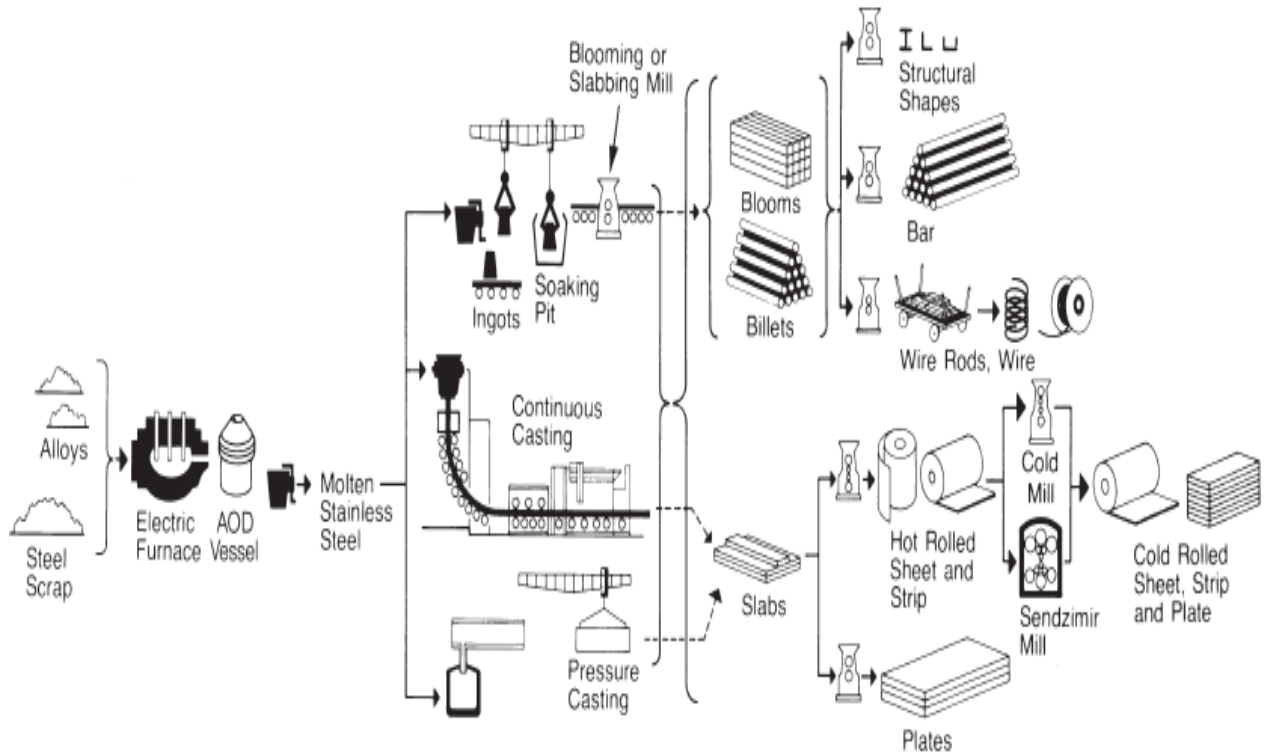


Figure I.2: Stainless steel manufacturing routes [ASM 00].

2. Duplex stainless steel

2.1 A brief history

The first reference to such alloys appears in 1927 [BAI 27], when Bain and Griffith published data on ferritic: austenitic structures. Within the next few years, several foundries in France, Germany, Sweden and the USA explored such steels, initially in the cast form [GUN 03].

Possibly the first commercial product dates from 1929 [LEF 97] when Avesta Jernverk produced a grade called 453E with approximate composition 25%Cr-5%Ni. Soon after in 1932 and 1933 a modified grade with 25/0Cr-50/0Ni-1%Mo (grade 453S) was marketed. Applications included coolers of the Brobeck type (plate and forgings), autoclaves for gunpowder production (castings) and valves for sulphite pulping (castings) [GUN 03].

Another record of early duplex products dates back to 1933, when an error during the melting of an 18%Cr-9%Ni-2.5%Mo grade at the Firminy works of the J. Holtzer Company, France, led to a 20/0Cr-8%Ni-2.5%Mo steel. Subsequent analysis [HOC 50] of the casting found it had a high volume fraction of ferrite in an austenitic matrix and was not sensitive to

intergranular corrosion (IGC) in various corrosive media. This was a significant discovery, as the high carbon austenitic grades of the time tended to form a continuous chromium carbide network, leading to rapid corrosion in the surrounding chromium depleted zones.

Research was undertaken at several laboratories so that, by the late 1940s, a new family of stainless steel was available which was patented and marketed simultaneously in France, Sweden and the USA [HOS 86, GUN 03].

The Korean war (1950-51) encouraged a nickel shortage, which led to further research into the relatively low nickel-content duplex alloys.

During the late 1960s and early 1970s, there were two main factors which advanced the development and use of duplex alloys. First, there was another nickel shortage that pushed up the price of austenitic alloys, combined with increased activity in the offshore oil industry which demanded a stainless material to handle aggressive environments. Second, steel production process techniques improved dramatically with the introduction of the vacuum and argon oxygen decarburization (VOD and AOD) practices. These techniques led to steels with simultaneously low carbon, sulphur and oxygen contents etc., while allowing for greater control of composition, especially nitrogen [GUN 03].

2.2 Modern Development of DSS

In the early 1980's, a second generation of duplex steels was introduced with improved welding properties mainly through nitrogen alloying. The most common duplex grade today is EN 1.4462 or 2205 (UNS S31803), which has a nominal composition of 22% Cr, 5%Ni, 3% Mo, and 0.16% N. The success of the 2205 grade led to the development of an entire family of duplex alloys, which range in corrosion resistance depending on their alloy content [CER 10]. The modern duplex stainless steels can be divided into four groups [NIL 95, CER 10]:

- Lean duplex as 2304, with 0.05-0.6 wt% of Mo
- 2205, the work-horse grade accounting for more than 80% of duplex use.
- 25Cr duplex as Alloy 255 and DP-3
- Super duplex, with 25-26 Cr and increased Mo and N compared with the 25 Cr grades, including grades such as 2507, Zeron 100, UR52N+, and DP-3W.

Table III.1 lists the chemical composition of the modern wrought duplex stainless steels and includes also the first generation of duplex stainless steels as a point of reference.

Table I.1 : Chemical composition in wt. % of wrought Duplex Stainless Steel grades with the corresponding Unified Numbering System and European Norm [IMO 09].

Grade	UNS No.	EN No.	C	Cr	Ni	Mo	N	Mn	Cu	W
Wrought duplex stainless steels										
First-generation duplex grades										
329	S32900	1,4460	0,08	23.0–28.0	2.5–5.0	1.0–2.0	–	1,00	–	–
**	S31500	1,4424	0,03	18.0–19.0	4.3–5.2	2.5–3.0	0.05–0.1		–	–
	S32404		0,04	20.5–22.5	5.5–8.5	2.0–3.0	0,20	2,00	1.0–2.0	–
Second-generation duplex grades										
Lean										
	S32001	1,4482	0,03	19.5–21.5	1.0–3.0	0,6	0.05–0.17	4.0–6.0	1,0	–
	S32101	1,4162	0,04	21.0–22.0	1.35–1.7	0.1–0.8	0.20–0.25	4.0–6.0	0.1–0.8	–
	S32202	1,4062	0,03	21.5–24.0	1.0–2.8	0,45	0.18–0.26	2,00	–	–
	S82011		0,03	20.5–23.5	1.0–2.0	0.1–1.0	0.15–0.27	2.0–3.0	0,5	–
2304	S32304	1,4362	0,03	21.5–24.5	3.0–5.5	0.05–0.6	0.05–0.20	2,50	0.05–0.60	–
		1,4655	0,03	22.0–24.0	3.5–5.5	0.1–0.6	0.05–0.20	2,00	1.0–3.0	–
Standard										
	S32003		0,03	19.5–22.5	3.0–4.0	1.5–2.0	0.14–0.20	2,00	–	–
2205	S31803	1,4462	0,03	21.0–23.0	4.5–6.5	2.5–3.5	0.08–0.20	2,00	–	–
2205	S32205	1,4462	0,03	22.0–23.0	4.5–6.5	3.0–3.5	0.14–0.20	2,00	–	–
25 Cr										
	S31200		0,03	24.0–26.0	5.5–6.5	1.2–2.0	0.14–0.20	2,00	–	–
	S31260		0,03	24.0–26.0	5.5–7.5	2.5–3.5	0.10–0.30	1,00	0.2–0.8	0.1–0.5
	S32506		0,03	24.0–26.0	5.5–7.2	3.0–3.5	0.08–0.20	1,00	–	0.05–0.30
	S32520	1,4507	0,03	24.0–26.0	5.5–8.0	3.0–4.0	0.20–0.35	1,50	0.5–2.0	–
255	S32550	1,4507	0,04	24.0–27.0	4.5–6.5	2.9–3.9	0.10–0.25	1,50	1.5–2.5	–
Super duplex										
2507	S32750	1,4410	0,03	24.0–26.0	6.0–8.0	3.0–5.0	0.24–0.32	1,20	0,5	–
	S32760	1,4501	0,03	24.0–26.0	6.0–8.0	3.0–4.0	0.20–0.30	1,00	0.5–1.0	0.5–1.0
	S32808		0,03	27.0–27.9	7.0–8.2	0.8–1.2	0.30–0.40	1,10	–	2.1–2.5
	S32906		0,03	28.0–30.0	5.8–7.5	1.5–2.6	0.30–0.40	0.80–1.5	0,8	–
	S32950		0,03	26.0–29.0	3.5–5.2	1.0–2.5	0.15–0.35	2,00	–	–
	S39274		0,03	24.0–26.0	6.8–8.0	2.5–3.5	0.24–0.32	1,0	0.2–0.8	1.5–2.5
	S39277		0,025	24.0–26.0	6.5–8.0	3.0–4.0	0.23–0.33	0,80	1.2–2.0	0.8–1.2
		1,4477	0,03	28.0–30.0	5.8–7.5	1.5–2.6	0.30–0.40	0.80–1.50	≤0.8	–
Hyper duplex										
	S32707		0,03	26.0–29.0	5.5–9.5	4.0–5.0	0.30–0.50	1,50	1,0	–
	S33207		0,03	29.0–33.0	6.0–9.0	3.0–5.0	0.40–0.60	1,50	1,0	–

2.3 Mechanical proprieties of DSS

Duplex stainless steels have exceptional mechanical properties. They are listed for the standard duplex grades in Table I.2. Their room temperature yield strength in the solution-

annealed condition is more than double that of standard austenitic stainless steels not alloyed with nitrogen. This may allow the design engineer to decrease the wall thickness in some applications. The typical yield strengths of several duplex stainless steels are compared with that of 316L austenitic stainless steel between room temperature and 300°C (570°F) in Figure I.3.

Because of the danger of 475°C (885°F) embrittlement of the ferritic phase, duplex stainless steels should not be used in service at temperatures above those allowed by the applicable pressure vessel design code for prolonged periods of time (see Table I.4).

Table I.2 : Minimum ASTM and EN mechanical property limits for duplex stainless steel plate [IMO 09].

Grade	UNS No.	ASTM			EN			
		Yield strength 0.2% MPa (ksi)	Tensile strength MPa (ksi)	Elongation in 2" (%)	EN No.	Proof strength $R_{p0.2}$ MPa (ksi)	Tensile strength R_m MPa (ksi)	Elongation A_5 (%)
2304	S32304	400 (58)	600 (87)	25	1,4362	400 (58)	630 (91)	25
2205	S32205	450 (65)	655 (95)	25	1,4462	460 (67)	640 (93)	25
2507	S32750	550 (80)	795 (116)	15	1,4410	530 (77)	730 (106)	20

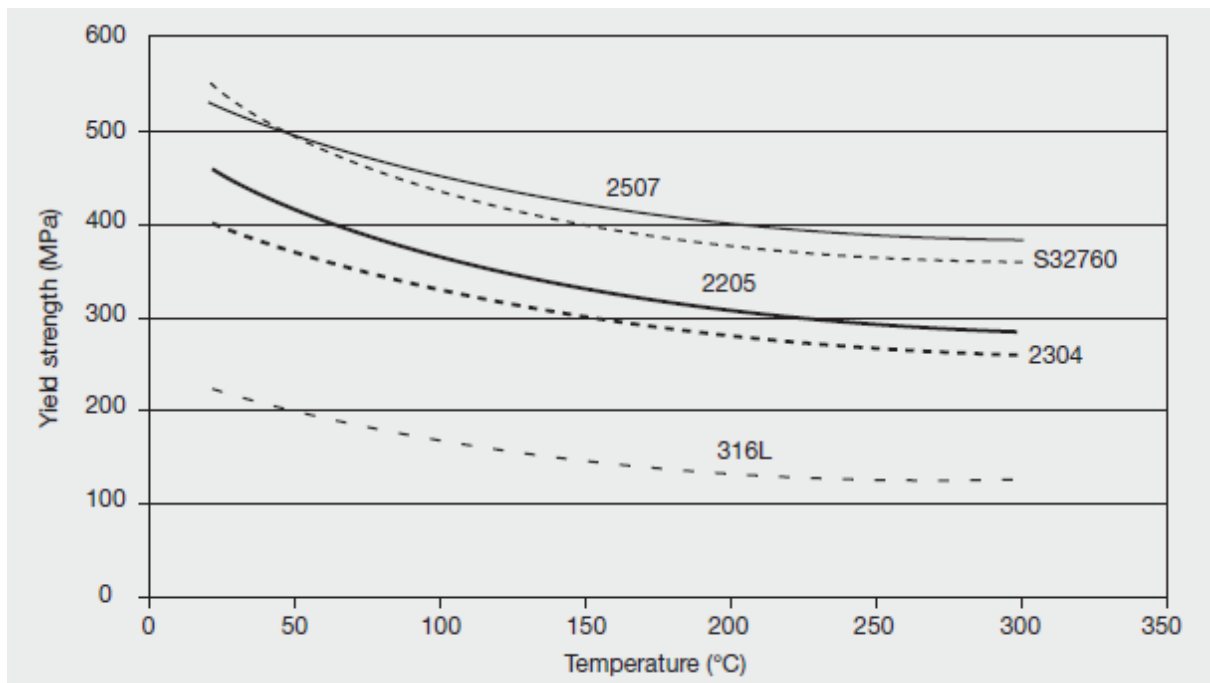


Figure I.3: Comparison of typical yield strength of duplex stainless steels and Type 316L between room temperature and 300°C (572°F) [IMO 09]

2.4 Physical proprieties of DSS

Ambient temperature physical properties for a selection of duplex stainless steels are given in Table I.3. Data are included for carbon steel and austenitic stainless steels for comparison.

In all cases, differences in physical property values among the duplex grades are very slight and probably reflect differences in test procedures. The physical properties of the duplex grades all fall between those of the austenitic stainless steels and carbon steels but tend to be closer to those of the stainless steels.

Table I.3: Ambient temperature physical properties of duplex stainless steels compared with carbon steel and austenitic stainless steels [IMO 09].

Grade	UNS No.	Density		Specific heat		Electrical resistivity		Young's modulus	
		g/cm ³	lb./in ³	J/kg K	Btu/lb./°F	micro Ωm	micro Ω in.	GPa	x10 ⁶ psi
Carbon Steel	G10200	7,64	0,278	447	0,107	0,10	3,9	207	30,0
Type 304	S30400	7,98	0,290	502	0,120	0,73	28,7	193	28,0
Type 316	S31600	7,98	0,290	502	0,120	0,75	29,5	193	28,0
Type 329	S32900	7,70	0,280	460	0,110	0,80	31,5	200	29,0
	S31500	7,75	0,280	482	0,115			200	29,0
	S32101	7,80	0,281	500	0,119	0,80	31,5	200	29,0
2304	S32304	7,75	0,280	482	0,115	0,80	31,5	200	29,0
	S31803	7,80	0,281	500	0,119	0,80	31,5	200	29,0
2205	S32205	7,80	0,281	500	0,119	0,80	31,5	200	29,0
	S31260	7,80	0,281	502	0,120			200	29,0
	S32750	7,85	0,285	480	0,114	0,80	31,5	205	29,7
255	S32550	7,81	0,282	488	0,116	0,84	33,1	210	30,5
	S39274	7,80	0,281	502	0,120			200	29,0
	S32760	7,84	0,281			0,85	33,5	190	27,6
	S32520	7,85	0,280	450	0,108	0,85	33,5	205	29,7
2507	S32750	7,79	0,280	485	0,115	0,80	31,5	200	29,0

2.5 Pitting Resistance Equivalent number PRE_N

It is common to define the corrosion resistance of duplex grades by their pitting resistance equivalence number [CER 10] (PRE_N) as defined by Equation I.1:

$$PRE_N = \%Cr + 3.3\%Mo + 16\%N \quad (I. 1)$$

Some alloys contain an addition of tungsten, which is another element that acts to increase the pitting resistance of stainless steels. For these alloys, the pitting resistance is expressed as PRE_W , according to Equation. I.2 [SAI 07, CER 10]:

$$PRE_W = \%Cr + 3.3\%Mo + 1.65W + 16\%N \quad (I. 2)$$

In fact, the pitting resistance equivalent number (PRE_N) has been introduced by the alloy producers as a tool for comparing stainless steels for their relative resistance to pitting. As the user of stainless steels has only a very limited knowledge of suitability of a specific steels for applications in the plant. It will allow the user to judge and select a material that is suitable for a environment and gives guidance about the alternate materials for various applications [SAI 07].

In general, materials having a pitting resistance number in the low 30's or lower are classified as lean duplex grades, those with PRE 's in the mid 30's such as 2205, are classified as standard duplex, and those with PRE 's of 40 or more are known as super-duplex alloys [CER 10].

2.6 Applications of DSS

As stated above, Duplex stainless steels (DSS) are Fe-Cr-Ni alloys having an approximately volumetric fraction of 50% ferrite and 50% austenite in their microstructures, therefore they combine some characteristics of each of these phases. Their main feature is that they compromise the favorable corrosion resistance of austenitic stainless steels with good mechanical properties [ARI 12]. The superior properties of the duplex stainless steels come primarily from approximately equivalent amounts of austenite (γ) and δ -ferrite [WEN 03].

They have been widely used in various industrial sectors due to their higher strength, better weldability, and higher resistance to stress corrosion and pitting [WEN 03]. Hence they are attractive material for applications where these properties are desired like in off-shore industries, food industries, chemical industries, paper industries [ROL 17, EZU 06], nuclear industries and in structural applications as well [KES 09].

In particular, the UNS S31803 alloy (also known as steel SAF 2205) is the most widely employed duplex stainless steels nowadays [EZU 06, KAI 14]. This material grade found widespread use in oil and gas industry, especially for high chloride containing process fluids like oily produced water and injection process systems.

At the Sixth Conference of Duplex Stainless steels, Charles [CHA 10] provides a paper which outlines the high number of applications where DSS and SDSS were extensively used, in particular [CER 10]:

- Pulp and paper industry (chip preparation and chip presteaming vessels, bleaching pulp storage tank, pulp batch digester- sulfite and sulfate processes, chlorine dioxide bleach water drums);
- Chemical and petrochemical industries (PVC stripper columns and heat exchangers, pressure vessel for organic products, reactors for the alcohol production);
- Hydrometallurgy;
- Chemical fertilizer industry (phosphoric acid production, urea industry);
- Organic and caustic media;
- Pollution control equipments;
- Chemical tankers;
- On/Offshore applications;
- Seawater and chloride containing water (hot water tanks and drums, seawater applications, reverse osmosis desalination, industrial and domestic water storage tanks and pipings);
- Architecture;
- Transports.

2.7 Limit of use of DSS

The use of DSS at high temperature is a typical concern to users of duplex stainless steels owing to their susceptibility to the formation of dangerous intermetallic phases which form after long exposure at high temperature [CAL 13]. The technical aspects related to the intermetallic phases precipitation will be treated in extent on **Section.3**.

Because long-term, elevated temperature exposure can result in loss of ambient temperature toughness, pressure vessel design codes have established upper temperature limits for the maximum allowable design stresses (Table I.4). The German TÜV code distinguishes between welded and unwelded constructions and is more conservative in its upper temperature limits than the ASME Boiler and Pressure Vessel Code. The temperature limits for these pressure vessel design codes for various duplex stainless steels are summarized in Table I.4.

Table I. 4: Upper temperature limits for duplex stainless steel for maximum allowable stress values in pressure vessel design codes [IMO 09].

Grade	Condition	ASME		TüV	
		°C	°F	°C	°F
2304	Unwelded	315	600	300	570
2304	Welded, matching filler	315	600	300	570
2304	Welded with 2205/2209	315	600	250	480
2205	Unwelded	315	600	280	535
2205	Welded	315	600	250	480
2507	Seamless tubes	315	600	250	480
Alloy 255	Welded or unwelded	315	600		

2.8 Chemical composition: effect of main alloying elements

The mechanical properties and corrosion resistance features of stainless steels depend on the chemical composition. Some of the main alloying elements effects are described on the following section:

Chromium:

The main advantage of adding chromium to steel is to improve the localized corrosion resistance, by the formation of a passive chromium-rich oxy-hydroxide film [HAS 79]. Electrochemically this is achieved by extending the passive range (see Figure I.4) and reducing the rate of general corrosion [GUN 03].

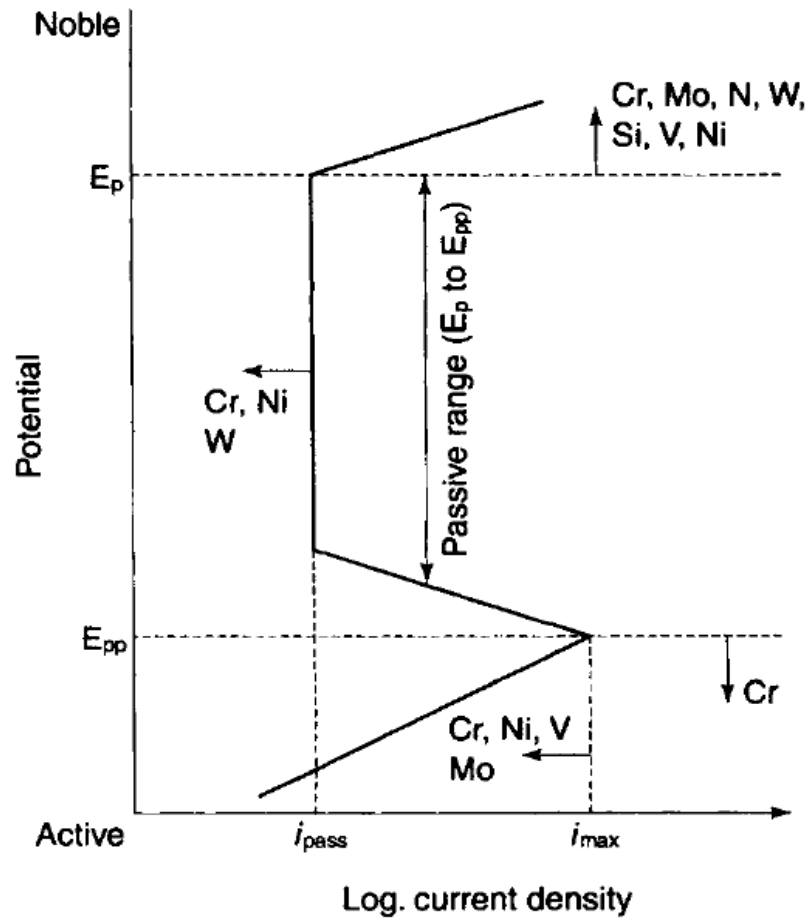


Figure I.4: effect of alloying elements on passive range [SED 85].

Chromium and other elements stabilize ferrite, although the effect of different elements varies. Equations have been derived to quantify elemental effects (the so-called chromium equivalents, Cr_{eq}) of which the most favored is [KOT 92, GUN 03]:

$$Cr_{eq} = \%Cr + \%Mo + 0.7\%Nb \quad (I.3)$$

The "stabilizing effects" of Cr on the ferrite is well illustrated on the binary iron–chromium equilibrium diagram (Figure I.5) which shows that chromium restricts the occurrence of the γ -loop to the extent that above 13wt% Cr the binary alloys are ferrite over the whole temperature range, while there is a narrow ($\alpha + \gamma$) range between 12 and 13wt%Cr. The ferrite is normally referred to as delta ferrite, because in these steels the phase can have a continuous existence from the melting point to room temperature [BHA 06].

However, there is a limit to the level of chromium that can be added to such a steel, as the beneficial effect of ever higher levels is negated by the enhanced precipitation of intermetallic

phases (Figure I.6) such as sigma. These phases often lead to reduction in ductility, toughness and corrosion properties, and are covered later in this chapter.

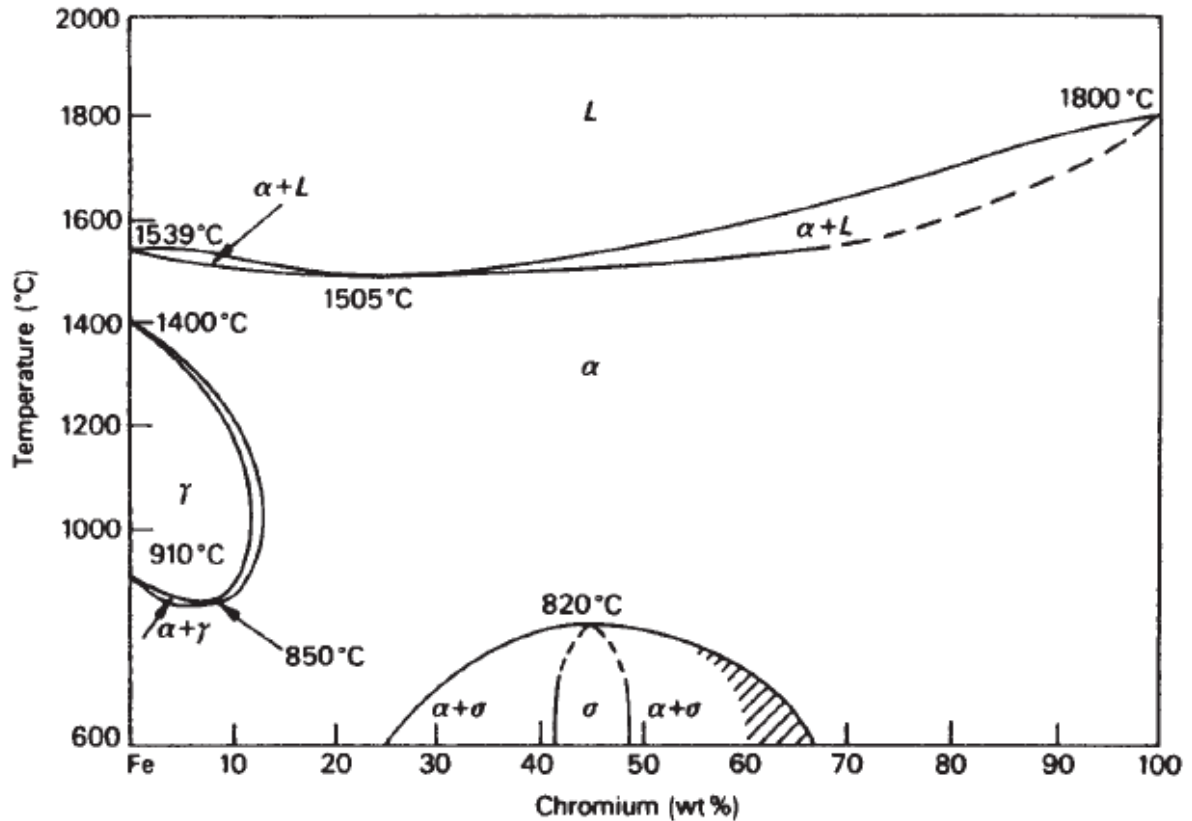


Figure I.5: The Fe–Cr equilibrium diagram [BHA 06].

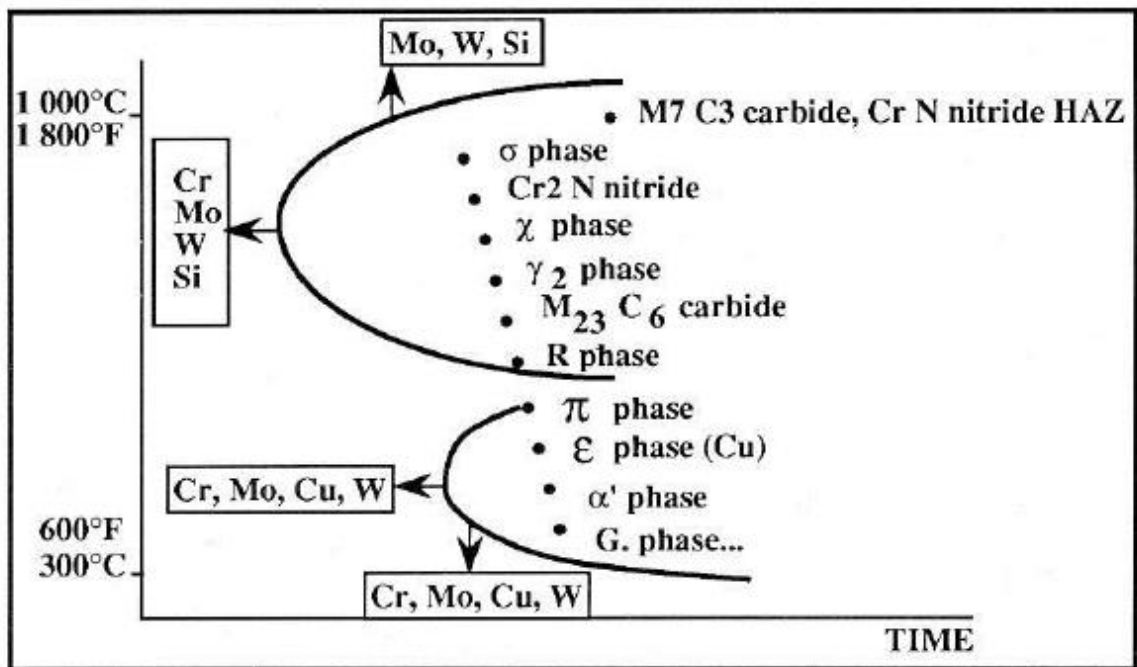


Figure I.6: Schematic TTP, time-to-precipitation, diagram for duplex stainless steels with secondary phases and influence of alloying elements[CHA 91]

Molybdenum

The molybdenum has a beneficial influence on the pitting and crevice corrosion resistance of an alloy in chloride solutions (Figure I.4). As for chromium, molybdenum extends the passive potential range and reduces the corrosion current density (i_{max}) in the active range. Molybdenum is included in both PRE relationships, Equations I.1 and I.2, and is given a coefficient of 3.3 times that of chromium, while it has a similar effect on ferrite stability as chromium, as indicated in Equation I.3 [GUN 03].

Nickel

Counter to the ferrite stabilizing effect of chromium (Mo and Nb), there is another group of elements which stabilize austenite:

$$Ni_{eq} = \%Ni + 35\%C + 20\%N + 0.25\%Cu \quad (I.4)$$

In summary, nickel does have some direct effect on corrosion properties, for instance moving E_p (Pitting potential), in the noble direction and reducing i_{pass} (Figure I.4), and yet it appears that the main role of nickel is to control phase balance and element partitioning [GUN 03].

Nitrogen

Nitrogen has a multiple effect on stainless steels by increasing pitting resistance, austenite content and strength. It has a similar influence on pitting as Cr and Mo, moving E_p , in the noble direction and thus increasing the passive potential range, (Figure I.4). This effect is enhanced in the presence of Mo and it has been suggested by other authors [TRU 77, OGA 82] that Mo and N have a synergistic influence on pitting characteristics. The proposed factor for nitrogen in the PRE_N relationship varies between 13 and 30, but the most widely used value for duplex alloys is 16.

Another important property of nitrogen is its ability to stabilize duplex alloys against the precipitation of intermetallic phases, such as sigma and chi, by reducing Cr-partitioning. It is also reported that increasing the nitrogen level reduces the risk of nitride formation. This may appear contradictory but is due to an increase in austenite content and so a reduction in the distance between austenite islands [GUN 03].

Manganese

Manganese has been quoted as an austenite stabilizer for austenitic steels and yet, for duplex alloys, mixed results have been obtained. Manganese additions to stainless steel increase abrasion and wear resistance and tensile properties without loss of ductility; Further, Mn

increases the solid solubility of nitrogen and thus allows for increased nitrogen contents to be achieved without risk of out-gassing. Nevertheless, the combined addition of Mn and N in modern duplex alloys improves the pitting resistance and counteracts the singular problems associated with Mn [CHA 82, GUN 03].

Carbon

The addition of carbon to the binary alloy extends the γ -loop to higher chromium contents (Figure I.7), and also widens the $(\alpha + \gamma)$ phase field up to 0.3wt%C [BHA 06].

The carbon content of most wrought duplex stainless steels is limited to 0.02% or 0.03%, primarily to suppress the precipitation of Cr-rich carbides which can act as initiation sites for pitting corrosion and intergranular attack [GUN 03].

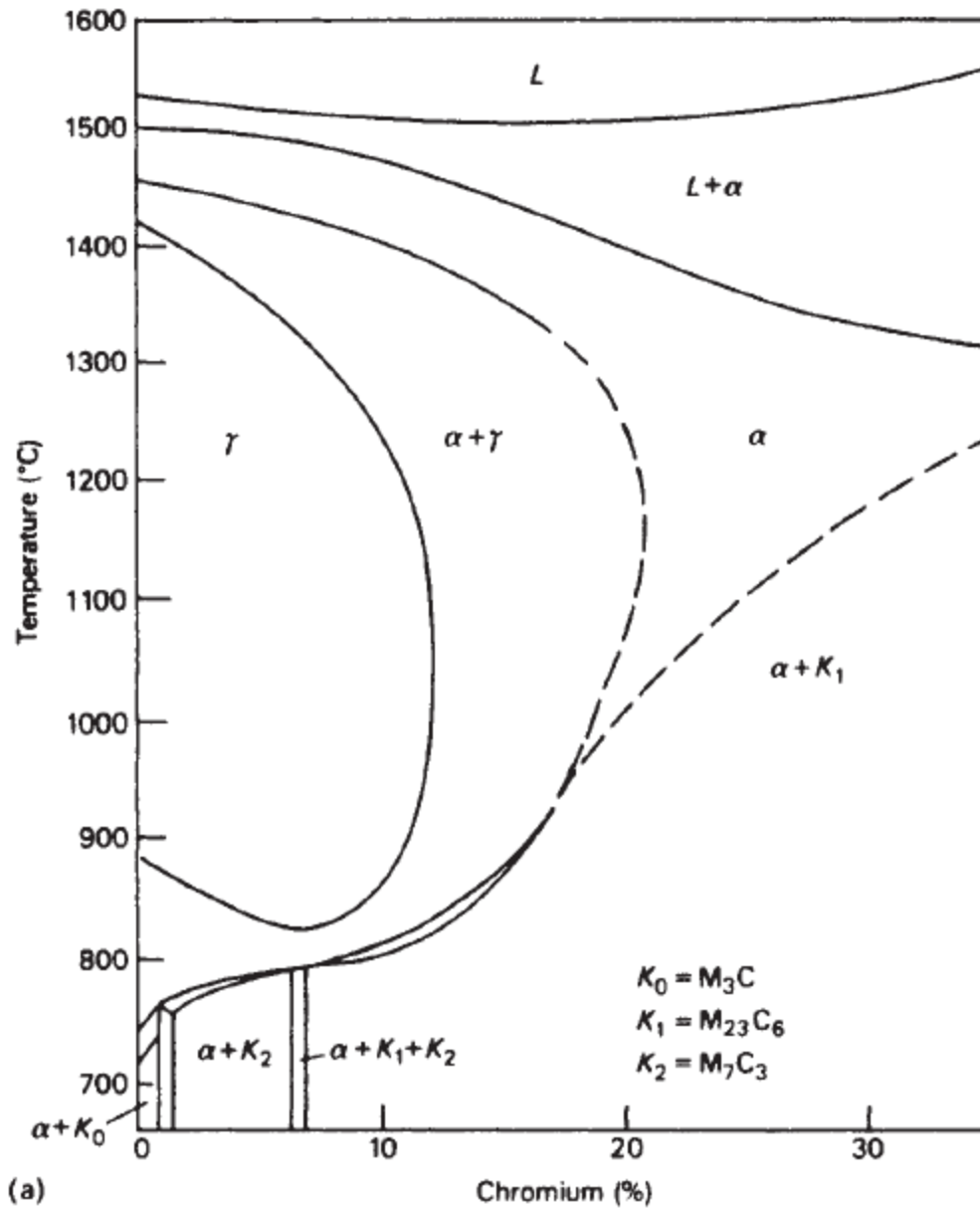


Figure I.7: Effect of carbon on the Fe–Cr diagram: (a) 0.05C wt% [BHA 06].

2.9 Effects of alloying elements on phase balance

An important aspect related to duplex stainless steels is the phase balance control, because it has a direct impact on corrosion and mechanical properties [CER 10]. The optimum phase balance for modern wrought products varies between manufacturers, but overall a range of between 45% and 60% austenite may be expected. The structure is obtained by simultaneous control of the chemical composition and annealing temperature [GUN 03].

Traditionally, the effects of different alloying elements on phase balance have been quantified by using the nickel and chromium equivalent numbers [CER 10]. One of the most convenient

ways of representing the effect of various elements on the basic structure of chromium–nickel stainless steels is the Schaeffler diagram, often used in welding. It plots the compositional limits at room temperature of austenite, ferrite and martensite, in terms of nickel and chromium equivalents (Figure I.8). At its simplest level, the diagram shows the regions of existence of the three phases for iron–chromium–nickel alloys [BHA 06].

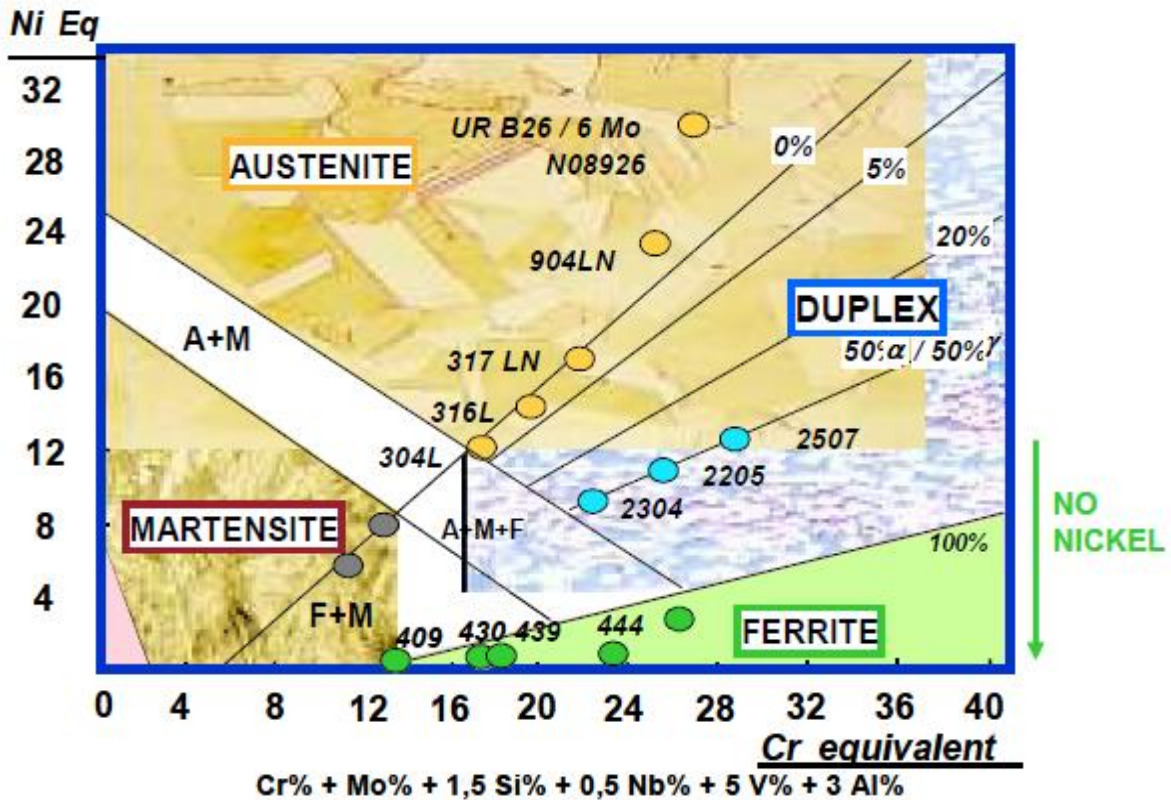


Figure I.8: Schaeffler diagram illustrating the Stainless Steels families positions [CHA 10]

On the other hand, several formulas have been proposed to determine the nickel and chromium equivalent numbers. Equations (I.5) and (I.6) show the formulas reported by Datta et al., as a reference [DAT 01]:

$$Cr_{eq} = \%Cr + 2\%Si + 1.5\%Mo + 5\%V + 5.5\%Al + 1.75\%Nb + 1.5\%Ti + 0.75\%W \quad (I.5)$$

$$Ni_{eq} = \%Ni + \%Co + 0.5\%Mn + 0.3\%Cu + 25\%N + 30\%C \quad (I.6)$$

To be noted that the Schaeffler diagram was originally developed for weld metal, i.e. it describes the structure after melting and rapid cooling, but it has also been found to give a

useful preview of the effect of the alloying elements for wrought and annealed material. However, annealed steels with predicted ferrite contents in the range 0–5 % according to the diagram contain in practice smaller amounts of ferrite [OUT 13].

Other empirical expressions have been proposed, based on the concept of equivalent Cr and Ni. The expression introduced by Leger et al. [LEG 88, ALV 09] states:

$$Cr_{eq} = \%Cr + 1.21\%Mo + 0.48\%Si + 0.14Nb - 4.99 \quad (I. 7)$$

$$Ni_{eq} = \%Ni + 24.5\%C + 0.11\%Mn - 0.0086\%(Mn)^2 + 2.77 \quad (I. 8)$$

$$\delta(\%) = 95.49 \left(\frac{Cr_{eq}}{Ni_{eq}} \right)^3 - 225.96 \left(\frac{Cr_{eq}}{Ni_{eq}} \right)^2 - 191.35 \left(\frac{Cr_{eq}}{Ni_{eq}} \right) - 58.27 \quad (I. 9)$$

where $\delta(\%)$ is the ferrite/austenite ratio.

Bonnet et al. have adjusted an empirical relation using the experimental results obtained on many CF8 and CF8M heats. This relation applies to ferrite content covering the range between 4% and 33% [BON 90, ALV 09]:

$$Cr_{eq} = Cr + Mo + 0.65.Si - 17.6 \quad (I. 10)$$

$$Ni_{eq} = Ni + 20.C + 8.3.N + 0.08.Mn - 5.18 \quad (I. 11)$$

$$\delta(\%) = 21.8. \left(\frac{Cr_{eq}}{Ni_{eq}} \right)^2 - 5.96. \left(\frac{Cr_{eq}}{Ni_{eq}} \right) + 3.39x \left(\frac{400}{1500-T} \right) \quad (I. 12)$$

where T is the annealing temperature in °C.

More recently, using thermodynamical calculations, Longbottom and Hayes [LON 94] have proposed an equation that gives not only the amount of ferrite, but also the mean composition of both phases.

However, the accuracy of those predictions remains limited as other factors, such as the thickness of cast parts, must also be considered [LEG 81, ALV 09].

3. Precipitation of secondary phases

Inevitably, a lot of stainless steel components are used or processed at elevated temperatures. In contrast to austenitic stainless steels, which are often used in high temperatures applications, DSS are not recommended in applications where temperatures exceed 250°C, the reason being the thermal instability of ferrite. In the temperature range 250-500°C spinodal decomposition of ferrite termed “475°C embrittlement” may occur after long term exposure, whereas various types of precipitate may form at temperature in the range 550-1000°C: σ , χ , ϵ , R phases, carbides and nitrides (figure I.9).

Although DSS most commonly used at temperatures below 250°C and, therefore, the effects mentioned above are not expected during service, the producers and manufacturers of these steels have to be aware of these phase transformations because they may occur either during production or during welding when the material is exposed to elevated temperature for shorter or longer times [CER 10].

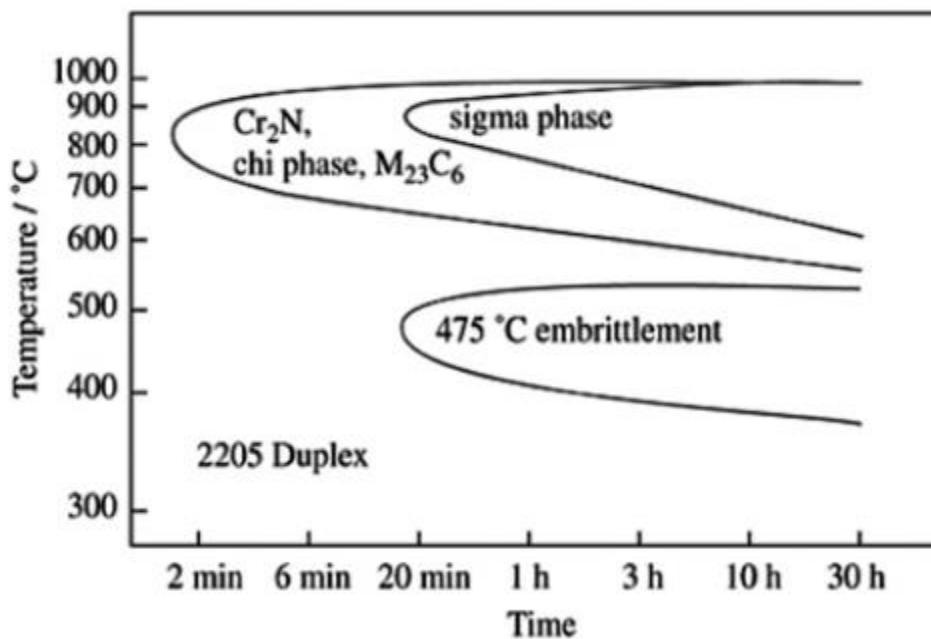


Figure I.9: Intermetallic phase precipitations for UNS S31803 DSS [PRA 15].

The various intermetallic phases that can occur in DSS and SDSS are tabulated in Table 5.

Table I.5: observed intermetallic phases in DSS [ALV 09].

Phase	UNIT CELL	Atoms per cell	Space group	Lattice parameters (nm)	Composition
Main phases					
Austenite (γ)	fcc	4	Fm3m	a = 0.358-0.362	(Fe,Cr,Ni,Mo,N)
Ferrite (δ or α)	bcc	2	Im3m	a = 0.285-0.289	(Fe,Cr,Ni,Mo)
Martensite (α')	bcc	2	Im3m	a = 0.285-0.289	(Fe,Cr,Ni,Mo,N)
Martensite (ϵ)	hcp	2 (6)	P6 ₃ /mmc	a = 0.250-0.255; c = 0.410-0.420	(Fe,Cr,Ni,Mo,N)
Intermetallic phases					
Sigma (σ)	bct	30	P4 ₂ /mnm	a = 0.87-0.92; c = 0.4554-0.48	(Fe,Ni) _x (Cr,Mo) _y
Chi (χ)	bcc	58	I43m	a = 0.881-0.895	Fe ₃₆ Cr ₁₂ Mo ₁₀ ; (Fe,Ni) ₃₆ Cr ₁₈ Mo ₄
Laves (η)	hex.	12	P6 ₃ /mmc	a = 0.473-0.483; c = 0.772-0.786	Fe ₂ Mo; Fe ₂ Nb; Fe ₂ Ta; Fe ₂ Ti; Fe ₂ W
G	fcc	116	Fd3m	a = 1.115-1.120	Ni ₁₆ Nb ₆ Si ₇ ; Ni ₁₆ Ti ₆ Si ₇ ; (Ni,Fe,Cr) ₁₆ (Nb,Ti) ₆ Si ₇
R	hex.	53 (159)	R3	a = 1.08-1.10; c = 1.92-1.94	Fe ₂₂ Mo ₁₈ Cr ₁₃ ; (Fe,Ni) ₁₀ Cr ₅ Mo ₃ Si ₂
Carbides					
M ₂₃ C ₆	fcc	116	Fm3m	a = 1.057-1.068	(Cr, Fe, Mo) ₂₃ C ₆ ; (Cr ₁₆ Fe ₅ Mo ₂)C ₆
MC	ord fcc	8	Fm3m	a = 0.4131- 0.4698	(Ti,Nb,V)C
M ₆ C	fcc	112	Fd3m	a = 1.085-1.128	(Fe, Mo, Nb,Cr) ₆ C
M ₇ C ₃	pseudo hex.	40	Pnma	a = 1.395-1.400; c = 0.452-0.453	(Cr,Fe) ₇ C ₃
Nitrides					
MN	ord fcc	8	Fm3m	a = 0.4097- 0.4577	CrN, ZrN;TiN; NbN; VN
M ₂ N	hexagonal	9	P31m	a = 0.475-0.480; c = 0.443-0.447	(Cr,Fe) ₂ N
Z-phase	tetragonal	6	P4/nmm	a = 0.303-0.306; c = 0.738-0.740	CrNNb

An overview of the various types of precipitates that may form in duplex stainless steels upon thermal ageing is reported briefly in the following sections (3.1 to 3.7). A special care is given for alpha prime (α') and sigma phases in dedicated sections (**Section.4 and Section.5**) as a great part the current work was allocated to these phases.

Precipitates can be categorized into two groups considering the temperature range of thermal aging as follows [CER 10]:

- Low range (250-500°C) where the most important precipitate is alfa prime (α')
- High range (550-1000°C) where the possible precipitates are σ , χ , secondary austenite, ϵ , R phases, carbides and nitrides.

3.1 Secondary austenite (γ_2)

Austenite precipitations in duplex steel created because of reheating to a temperature lower than the solvus line temperature (Figure I.10) after fast cooling are considered as the secondary austenite [CER 10].

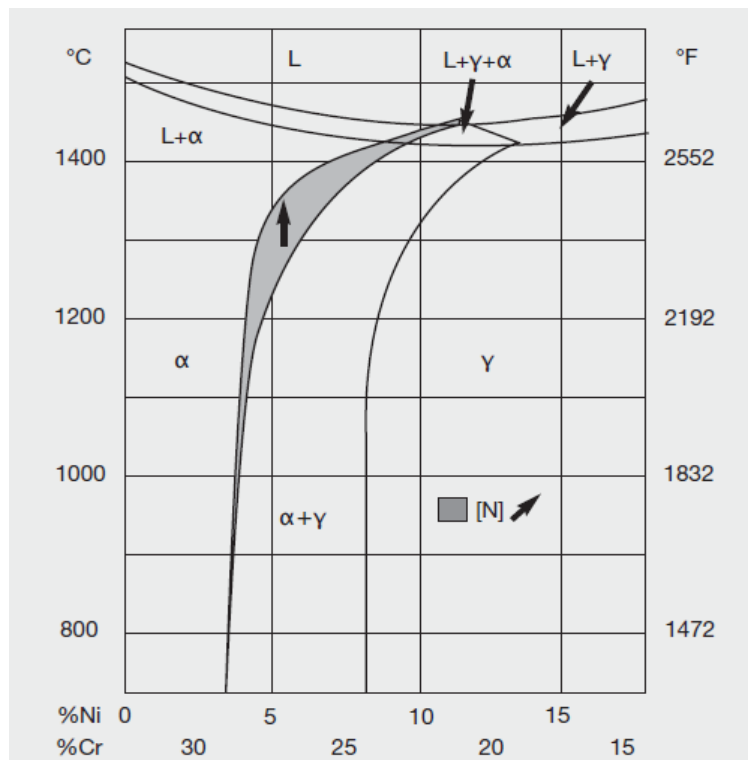


Figure I.10: Section through the Fe-Cr-Ni ternary phase diagram at 68% iron (small changes in the nickel and chromium content have a large influence on the amount of austenite and ferrite in duplex stainless steels [IMO 09]).

There appear to be three mechanisms for secondary austenite formation [CER 10, GUN 03]:

- as a result of the eutectoid reaction $\delta \rightarrow \sigma + \gamma_2$ in the temperature range 700–900°C (at the ferrite/austenite grain boundaries).
- a diffusive transformation at a temperature above 650 °C resulting in a Widmanstätten precipitates (intragranular)
- a non-diffusive isothermal transformation at a temperature lower than 650°C analogous to a martensitic transformation.

It was reported that intragranular secondary austenite has a lower chromium, molybdenum and nitrogen content compared to the primary austenite, therefore it is more susceptible to pitting attack [NIL 95, CER 10].

3.2 Chi (χ) phase

Chi phase formation takes place prior to sigma phase formation between temperatures 750–850°C. This phase is thermodynamically unstable. Chi phase (χ) forms on the ferrite/ferrite interface and grows into the ferrite. The sigma phase formation takes place at the expense of Chi phase as shown in Figure I.11. As Chi-phase is richer in Mo than sigma phase and Mo being a heavy element, it is easy to contrast between sigma and chi phase using Back-Scattered Electron Microscope (BSE) [MIC 06, ESC 09, PRA 15].

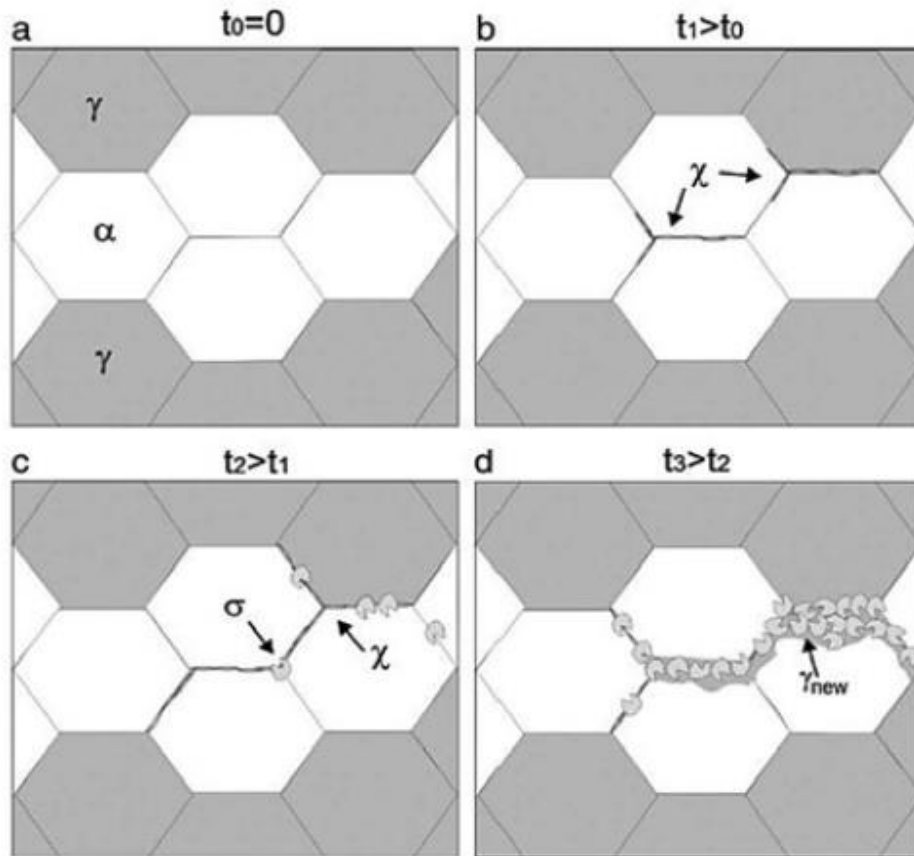


Figure I.11: Chi phase precipitation in DSS [ESC 09].

3.3 Chromium nitrides ($\text{CrN}/\text{Cr}_2\text{N}$)

Chromium nitrides precipitation is commonly found between temperatures 700–900°C, during fast cooling from high annealing temperatures [PAR 15].

Slow cooling rates reduce the amount of Cr_2N due to increasing austenite formation, where nitrogen can dissolve. The precipitation decreases the pitting corrosion resistance due to depletion of chromium and nitrogen. There is also another nitride, CrN , which forms during the welding operations in the Heat affected zone [NIL 92, HOF 94, LIA 01, CER 10].

3.4 R-phase

R-phase precipitates between temperatures 550-650°C in an initial stage of aging and later, disappears with aging time by transformation to Sigma phase. They form at intra and inter granular sites. R-phase is Mo rich compound and their stability increases with increase in Mo content [PRA 15].

3.5 Π -phase

Π -phase formation takes place after isothermal heat treatment at 600°C for long aging time. This phase is often confused with Sigma phase as it is also rich in Cr and Mo [PRA 15].

3.6 τ -phase

τ -phase is a needle like structure which forms at ferrite/ferrite boundaries after heat treatment between 550-650 °C [PRA 15].

3.7 Carbides $M_{23}C_6$ and M_7C_3

M_7C_3 forms between 950°C and 1050°C at the δ/γ grain boundaries. However, as its formation takes 10 minutes, it can be avoided by normal quenching techniques. Further, as modern duplex grades contain less than 0.02 % C, carbides of either form are rarely if ever seen [GUN 03].

4. Sigma phase precipitation:

Sigma phase is a Cr-Mo rich hard precipitate which occurs at temperatures between 600-1000°C. This phase is one of the main reasons for the deterioration of stainless steels properties, for example, mechanical property, corrosion resistance, and weldability [CHI 12].

4.1 Development Progress of the σ Phase:

In the review article published by Chih et al [CHI 12], an overview of the historical development of sigma phase was given:

- (1) In 1907, Treitschke and Tammann found that the σ phase in the Fe-Cr binary system was an intermetallic compound of 30wt.% Cr~50wt.% Cr.
- (2) In 1927, Bain and Griffiths observed the successful σ phase in the Fe-Cr-Ni ternary system. They found that the σ phase was a very hard and brittle compound which impacted the toughness of the steels. At that time, the σ phase was called the “B constituent”.
- (3) In 1936, this Fe-Cr compound was called the “ σ phase” by Jett and Foote, which became its official name.
- (4) In 1951, the crystal structure of the σ phase in the Fe-Cr binary system was examined by Yano and Abiko They pointed out that the σ phase exhibited slower precipitation kinetics in the Fe-Cr alloy system than in the Fe-Cr-Mo and Fe-Cr-Si ternary systems.

- (5) In 1966, the σ phase was observed by Hattersley and Hume-Rothery and Hall and Algie in austenitic stainless steels.
- (6) By 1966, the σ phase had been found in over 50 transition alloys [6], including Cr-Ni, Fe-Cr-Ni, Fe-Cr-Mo, Fe-Cr-Mn, Fe-Cr-Ni-Mo, Fe-Cr-Si, Fe-V, Re-Cr, Mo-Re, Ta-Al, W-Te, Ta-V, Zr-Ir, Nb-Pd, Ti-Mn, and Nb-Fe.

4.2 Precipitation Characteristic of the σ Phase:

The σ phase is a tetragonal crystal structure with 30 atoms per cell, and its precipitation temperature is between 600°C and 1000°C . The crystal information and chemical composition of the σ phase are listed in Table I.6 [CHI 12].

The elements Cr, Mo, Si and Mn have been noted to encourage sigma formation (previous Figure I.6). In addition, nickel has been found also to enhance σ formation, but reduce the equilibrium volume fraction. This occurs as nickel induces γ formation and so concentrates the σ promoting elements in the remaining ferrite [GUN 03].

The “*Sigma Equivalent*” (σ_{eq}) is a parameter proposed by Ramirez et al to measure the tendency of a DSS or SDSS to σ precipitation [CER 10]:

$$\sigma_{eq} = X_{Cr(\delta)} + 4.5.X_{Mo(\delta)} + 1.5.X_{Si(\delta)} \quad (I.13)$$

Where, $X_{Cr(\delta)}$, $X_{Mo(\delta)}$ and $X_{Si(\delta)}$ are the amounts of Cr, Mo and Si in the ferritic matrix.

Therefore, it can be easily noted that super duplex stainless steels with high additions of Cr and Mo are more prone to sigma precipitation.

Gow and Harder pointed out an empirical formula to examine the precipitation tendency of the σ phase, as expressed in equation I.14 [GOW 42, CHI 12]:

$$\text{Ratio factor} = \frac{\%Cr - 16\%C}{\%Ni} \quad (I.14)$$

If ratio factor > 1.7 , the σ phase can precipitate in stainless steels. When the C content is much higher, the ratio factor is much lower, and the precipitation tendency of the σ phase is decreased.

This phase occurs due to Eutectoid reaction where ferrite is converted to Sigma (σ) and secondary austenitic phase (γ_2) [MAR 09, CHI 12].

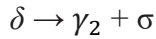


Table I.6: Chemical composition and lattice constant of the σ phase [CHI 12].

Alloy	Lattice parameter (Å)	Composition of phase (wt%)					Formula
		Fe	Cr	Ni	Mo	Si	
Fe-Cr	$a_0 = 8.799, c_0 = 4.544$						Fe-Cr
Fe-Mo	$a_0 = 9.188, c_0 = 4.812$						Fe-Mo
17Cr-11Ni-2Mo-0.4Ti	—		30	4.3	9	0.8	
17Cr-11Ni-0.9Mo-0.5Ti	—		33	4.5	5.4	0.7	
Type 316	$a_0 = 8.28 \sim 8.38, c_0 = 4.597 \sim 4.599$	55	29	5	11	—	$(\text{FeNi})_x(\text{CrMo})_y$
Type 316L	$a_0 = 9.21, c_0 = 4.78$						
20Cr-25-34Ni-6.5-8Mo	$a_0 = 8.87, c_0 = 4.61$	35/37	17/26	15/21	21/28	—	
25Cr-20Ni	—	40	46	9.4	—	3	

At temperature between 850-900°C, sigma phase has fastest precipitation rate.

Sikka pointed out that the σ phase was easy to precipitate at the δ/γ interphase boundaries [SIK 83] because the δ/γ interphase was a high boundary energy place and so a beneficial site for the heterogeneous nucleation of the σ phase. Sato et al. [SAT 99] found that a high lattice coherent degree and low δ/γ boundary energy could suppress the precipitation of the σ phase.

Na et al. [NA 00] found that the σ phase formed in γ -austenite when the aging time was high; they constructed a schematic diagram to explain the precipitation behavior of the σ phase, as shown in Figure I.12. For Case 1, the σ phase was formed in γ -austenite, but needed a higher aging temperature (above 1000 ° C), as shown in Figure I.12(a). For Case 2, the σ phase precipitated at the δ/γ interphase boundary because this boundary was a region of high boundary energy, as displayed in Figure I.12 (b). For Case 3, the σ phase precipitated in δ -ferrite particle and was attributed to the high Cr region of δ -ferrite. This precipitation behavior was the least difficult condition to accomplish, as represented in Figure I.12 (c). Padilha and Rios [PAD 02] pointed out that the σ phase precipitating directly in γ -austenite was very slow (about several thousand hours) [CHI 12].

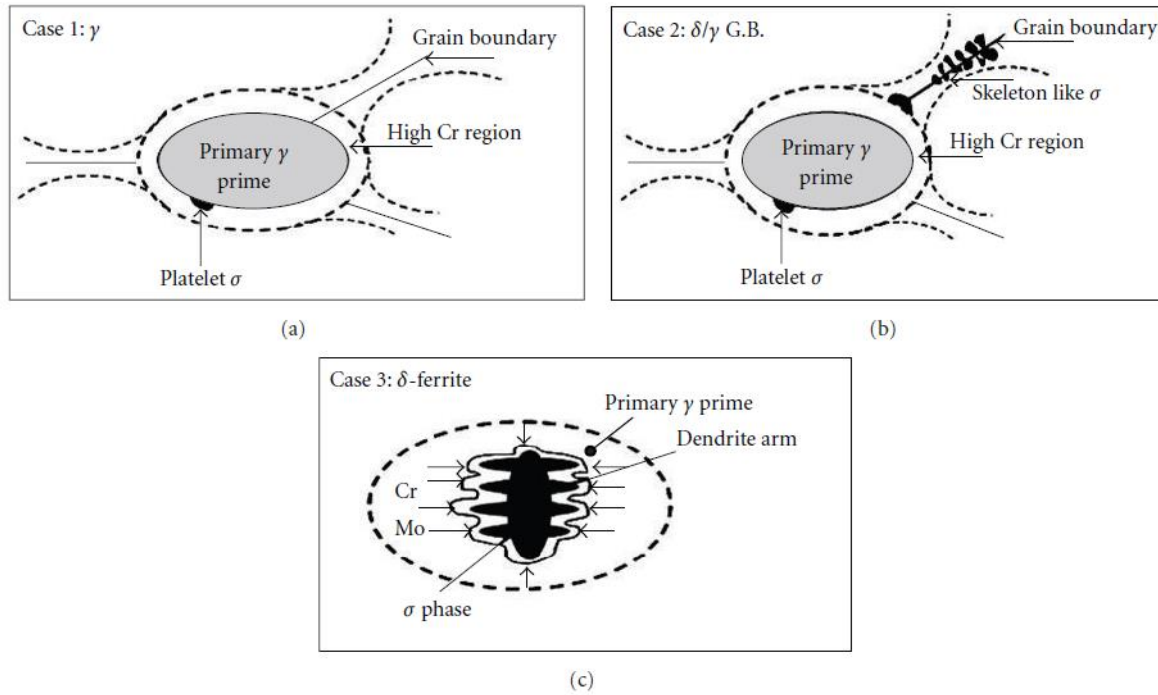


Figure I.12: Schematic diagram of the σ phase precipitation [CHI 12].

However, the schematic diagram shown in figure I.13 has been proposed by Villanueva et al. [VIL 06] to explain the precipitation mechanism of the σ phase in a duplex stainless steel (UNS S31803).

Here are δ and γ phases in UNS S31803 duplex stainless steel without heating (T_0). Some laminar cellular structures ($\sigma + \gamma_{new}$) are formed at the δ/γ interphase boundaries when the aging temperature is T_1 . Furthermore, the laminar cellular structures continue to grow when the aging temperature is increased to T_2 . Finally, the δ -ferrite is occupied completely [CHI 12].

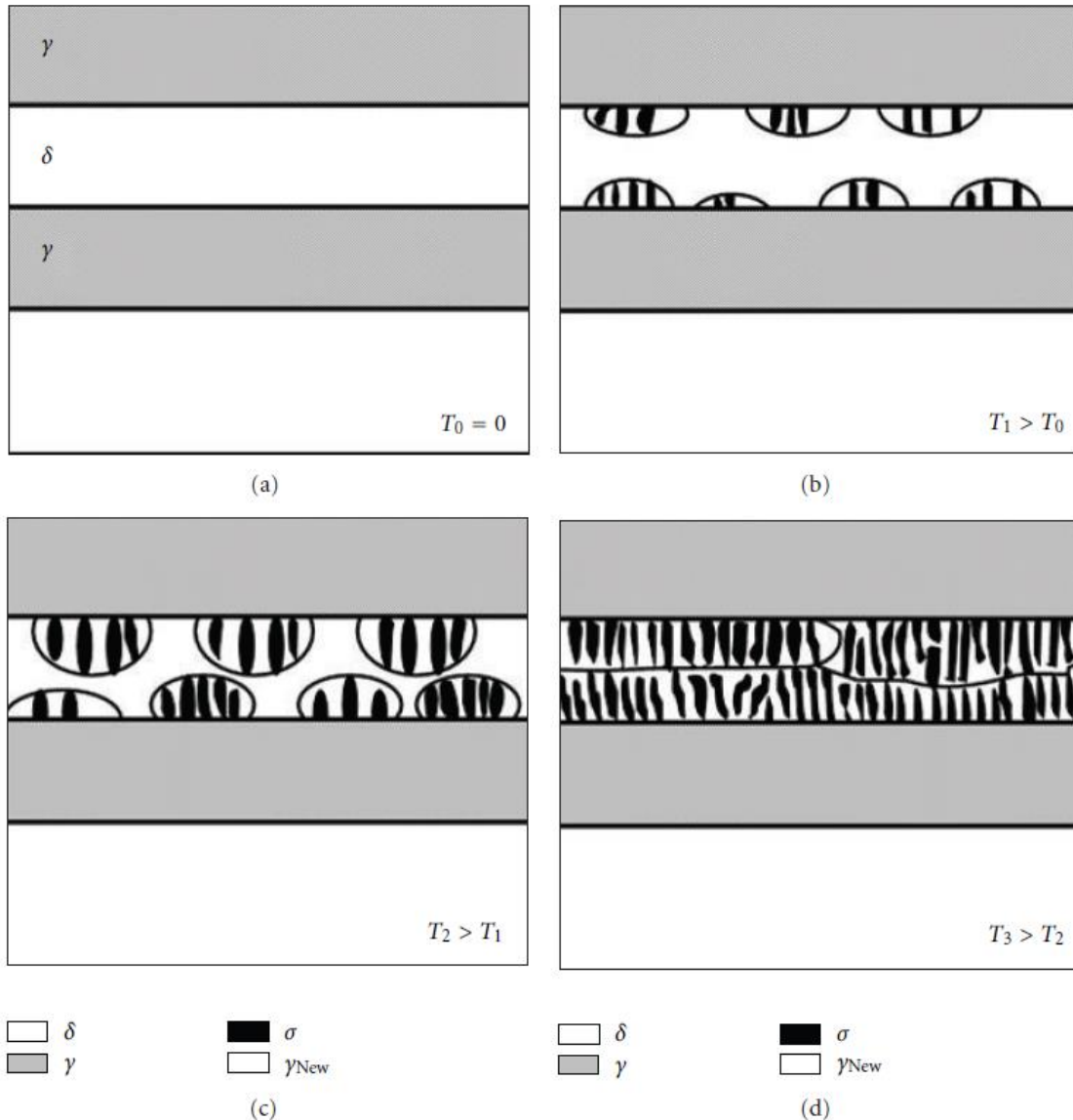


Figure I.13: Precipitation mechanism of the σ phase in UNS S31803 stainless steel [CHI 12].

4.3 Isothermal Kinetics Modeling of Sigma Phase Formation

(a) Classical JMA Model

The fraction of sigma phase can be described by a Johnson-Mehl-Avrami (JMA) type expression, which is formulated in the original paper by Avrami [AVR 39, FER 17] as follows:

$$1 - V = \exp[-Bt^k] \quad (I.15)$$

Where, V is the fraction transformed at time t , B is a function of temperature and k is a constant varying between 1 and 4 and depending upon the nucleation and growth mechanism. Since then, many workers commonly write Equation (I.15) as:

$$y = \frac{V}{V_{eq}} = 1 - \exp[-Kt^n] \quad (I.16)$$

where y is the fraction of sigma phase formed ($0 < y < 1$) after an isothermal treatment at a time period t , V_{eq} is the equilibrium amount of transformed phase at temperature T , K is an overall rate constant related to the activation energy to sigma phase formation and n is the Avrami exponent [MAG 09, FER 17].

The constant K is defined by Equation (I.17), where Q_σ is the activation energy for sigma phase formation and R is the universal gas constant.

$$K = k_0 \cdot \exp\left(-\frac{Q_\sigma}{RT}\right) \quad (I.17)$$

In order to extrapolate the kinetic parameters (n , K) from experimental data, Equation (I.16) is often rearranged as follows:

$$\ln\left[\ln\left(\frac{1}{1-y}\right)\right] = \ln(K) + n \cdot \ln(t) \quad (I.18)$$

The phase transformation kinetics obeys the classical JMA model when the evolution of $\ln\left[\ln\left(\frac{1}{1-y}\right)\right]$ as a function of $\ln(t)$ gives a straight line (Avrami plot).

Although the JMA exponent can't be used to precisely identify the mechanism, it can be used as an indicator of the type of nucleation and growth conditions that are occurring. According to Christian [CHR 75], a JMA exponent above 4, like those observed at low fractions of sigma, would indicate that the transformation is taking place by either a discontinuous precipitation or an interface controlled growth mechanism, with a nucleation rate that increases with increasing [ELM 06].

The kinetic studies of sigma phase formation were explored earlier [ELM 07, MAG 09, SAN 13] and a divergence between proposed kinetic mechanisms was observed. Palmer et al. [ELM 07] suggested that a change in the mechanism of sigma phase formation occurs during aging. The authors mentioned that in the beginning of aging time, n varies between 7 for high and 0.75 for low temperatures and sigma was formed by continuous precipitation controlled by

interface. With increasing aging time, the mechanism changes to a diffusion-controlled growth [SAN 16].

However, Magnabosco et al [MAG 09] pointed that the mechanism of sigma phase formation is diffusion-controlled growth, with n values of approximately 0.9, during aging between 700 °C and 850 °C, and proposed that the activation energy for sigma phase formation may be related to the activation energy for Cr diffusion in ferrite (185 kJ/mol).

(b) Modified JMA model:

When studying intermetallic phase precipitation, different authors have found that a better interpolation of the experimental results is obtained by using a modified JMA model [LEE 90, BAD 14, FER 12, FER 17]:

$$y = 1 - \left[\frac{1}{1+c.(K.t)^n} \right]^{\frac{1}{c}}, \text{ with } c \neq 0 \quad (I. 19)$$

Where c (coefficient) is the impingement exponent used to correct some complex competing effects that may occur during precipitation such as [BAD 08, FER 17]:

- (1) depletion of the solute content in the untransformed matrix due to competitive growth of the fraction products,
- (2) direct collision of two advancing reaction products, or
- (3) exhaustion of nucleation sites.

In addition to the theoretical restrictions of the JMA model, there are also physical phenomena to take into account. Kinetic parameters of intermetallic phase precipitation are influenced by chemical composition [HUA 05], solution heat treatment [KAS 12] (and consequently primary phase proportion, phase and grain size), hot and cold working [CHO 13], as well as aging time and temperature [FER 17].

The above equation can be rearranged as follows [BAD 08, FER 12] :

$$(K.t)^n = \frac{(1-y)^{-c}-1}{c} \quad (I. 20)$$

and then:

$$n. \ln(K) + n. \ln(t) = \ln \left[\frac{(1-y)^{-c}-1}{c} \right] \quad (I. 21)$$

There are now 3 adjusting parameters, n , K and c . When a suitable value of c is adopted, a plot of $\text{Ln} \left[\frac{(1-y)^{-c}-1}{c} \right]$ vs. $\text{Ln}(t)$ can result in a straight line. Then, the value of n and K can be obtained from the slope and the intercept [BAD 08].

During our literature review, we noted that only few studies have investigated the modified JMA model to follow the kinetic process of sigma precipitation in DSS steels. Hence, this aspect will be examined in the current study.

4.1 Effect of the σ Phase on the Properties of Duplex Stainless Steels

It is supposed that among intermetallic precipitates, sigma phase is the most detrimental one, as it causes a considerable drop in toughness as well as corrosion resistance [KES 09]. Without doubt, even small amounts of sigma phase influence the resistance against most corrosion forms such as pitting, sulphide stress corrosion cracking, intergranular corrosion and hydrogen embrittlement. Consequently, the standard criterion is that no sigma phase is allowed in produced duplex materials [MAT 13].

Recently in 2019, C.R. de Farias Azevedo et al [FAR 19] have conducted a literature survey on the main cases of failure analysis of DSS. Most of these failures took place in the welded joints either in the heat-affected zone (HAZ) or in the molten zone. Additionally, almost 50% of these failures involved the precipitation of deleterious phases, usually the sigma phase. The corrosion failures usually started with the action of a localized corrosion mechanism, like pitting corrosion or preferential corrosion. This corrosion mechanism can be promoted by the precipitation of deleterious phases (Cr-rich carbide and sigma phase) and the unbalance between the proportion of ferrite and austenite phases.

In the table I.7, we have reported some failure cases involving sigma phase precipitation.

Table I.7: Some failure cases involving sigma phase precipitation, from [FAR 19].

Class.	Product	Failure and causes
UNS J93370 (CDM4Cu)	Casting valves The valves operated with circulating seawater at 69 bar and working temperature between 40 and 45 °C during 15 years.	Type of failure: Pitting corrosion. Causes: The chemical composition of DSS casting presented higher content of Mo and lower content of Cu than the required. The proportion of ferrite was much higher than the required. The crack propagated along α/γ interfaces due to the precipitation of Cr-carbide and σ phases

Class.	Product	Failure and causes
UNS S32750	Welded vessel (polymer industry) The vessel was manufactured by circumferential and longitudinal welds of wrought DSS plates.	Type of failure: Stress corrosion cracking (SCC) in the HAZ. Causes: Two circumferential joints were made by SMAW (shield metal arc welding)/GMAW (gas metal arc welding) followed by SAW (submerged arc welding), leading to the formation of 2% of σ phase in the HAZ. The service environment was rich in chloride (~ 220 ppm) and worked at 110 °C. The remaining SAW joints did not show SCC. Crevice corrosion of the sigma/austenite interface of the HAZ promoted the stress corrosion cracking (SCC) propagation along the α/γ interfaces and in the austenite phase.
UNS S32900	Forged double disc valve stem (nuclear industry) The DSS stem of a heavy water plant failed after 30 year of use in an environment containing H ₂ S, pH 4, 128 °C and pressure of 19 kg/cm ² . The stem was forged and annealed at 1000 °C.	Type of failure: Sulphide stress cracking. Causes: The annealing heat treatment of the valve stem caused the precipitation of σ phase. The SSC crack preferentially propagated in the ferrite phase and along the α/γ boundary due to the presence of the σ phase.
UNS S31803	Welded duct nozzle (oil industry) The nozzle injected steam (fluid of 99.99% of H ₂ O with a flow rate of 262,000 lbs./h at 105.5 °C and 14.6 psi) into a heavy oil reservoir and failed after four years of operation.	Type of failure: Fatigue crack in the weld region (perpendicular direction to the weld axis). Causes: The fatigue failure was promoted by the vibration of the piping system. The high content of austenite (~ 70%) and the precipitation of deleterious phases (σ phase and a Cr-rich intermetallic) in the weld region facilitated the crack propagation.
UNS S32760	Welded pipe for oil transportation (oil industry) The pipe failed with 1 month of operation with pits on the weld joint region.	Type of failure: Pitting corrosion in the HAZ. Causes: Preferential corrosion of the α/γ interface due to a precipitation of ~ 8% of σ phase during the heating procedure before the repair welding, which is not recommended for SDSS pipes.

5. Alpha Prime (α') phase

The lowest temperature decomposition within a duplex steel is that of alpha prime (α'), which occurs between 300 and 525°C (figure I.14), and is the main cause of hardening and “**475 embrittlement**” in ferritic and Duplex stainless steels [MAE 14]. This embrittlement is caused by decomposition of ferrite phase into α phase (rich in iron) and α' phase (rich in chromium). The presence of miscibility gap in Fe-Cr phase diagram causes this embrittlement. At 475 °C [SAH 09], the rate of embrittlement is highest, hence this occurrence is known as 475 °C embrittlement [PRA 15].

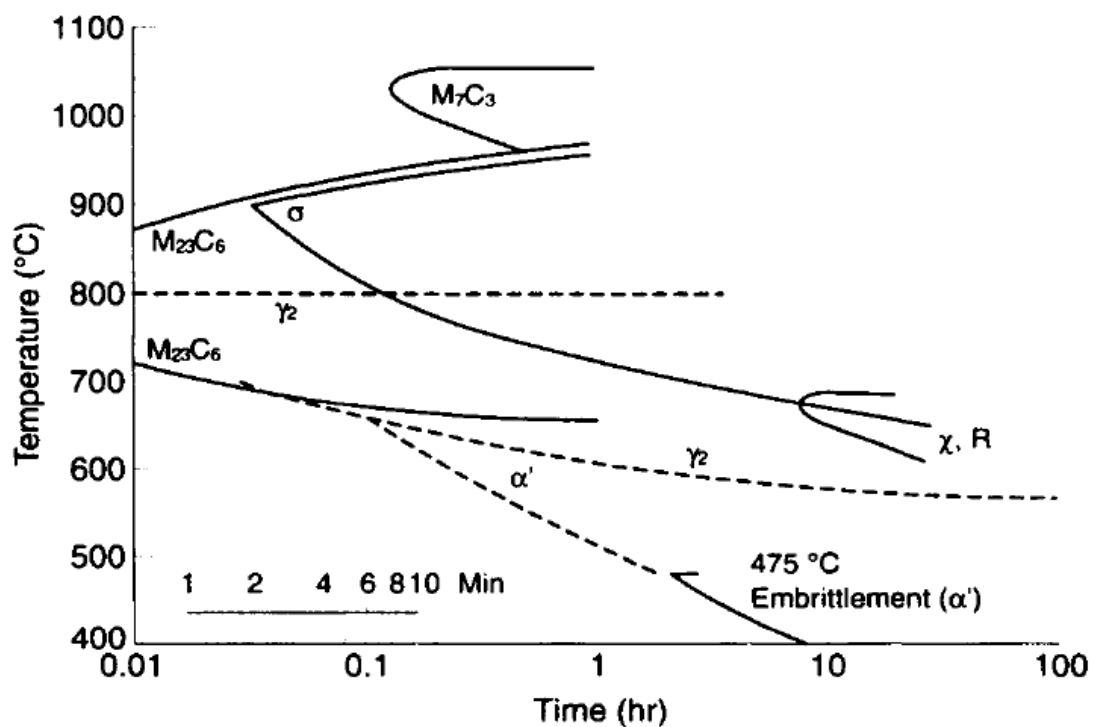


Figure I.14: Time-Temperature Transformation diagram for alloy S32404 [GUN 03].

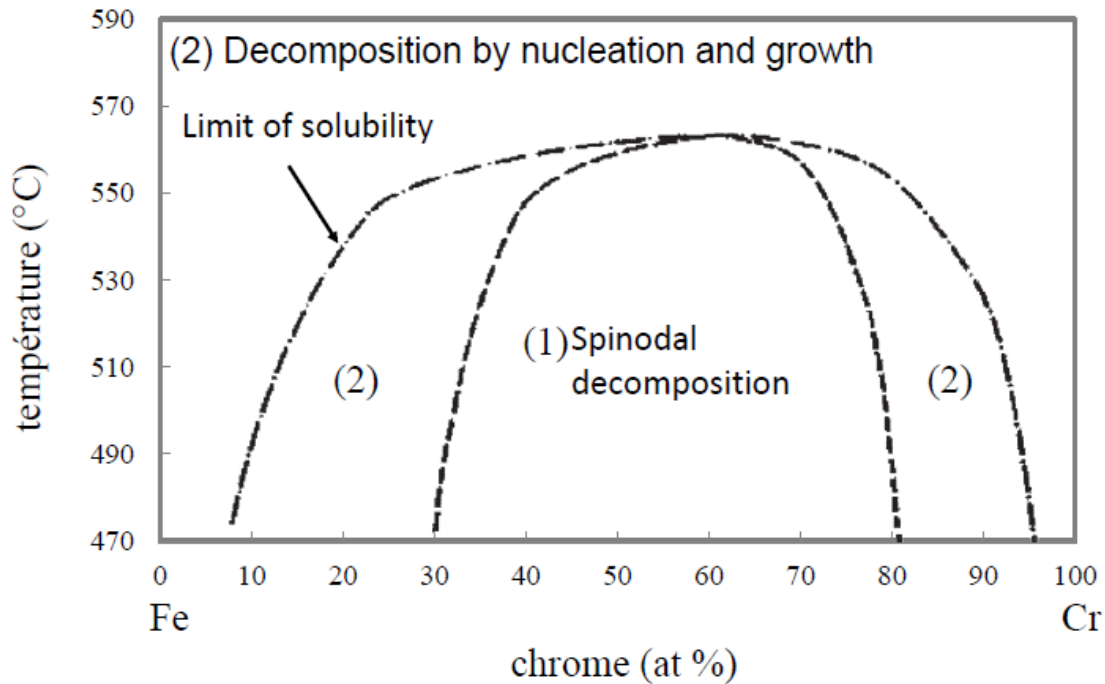


Figure I.15: Fe–Cr binary phase diagram [MAE 14].

Depending on the temperature and the composition of the ferrite, the decomposition can occur according to two mechanisms: either by spinodal decomposition, or by a classical mechanism of nucleation and growth (see figure I.15). These mechanisms are briefly described on the following section.

5.1 Spinodal decomposition and nucleation – growth mechanism

These unmixing mechanisms are illustrated in Figure I.16.

During decomposition by germination and growth, the precipitates of α' dispersed in the matrix α , germinate directly to their equilibrium composition and grow by absorbing the surrounding elements. During spinodal decomposition, composition fluctuations appear, which give rise to a progressive enrichment of α' and α zones, in chromium and iron [MIT 10, POR 92].

However, whatever the mechanism of decomposition of the ferrite, the morphology of α' and α becomes identical when the system tends towards equilibrium, with respectively concentrations equal to the solubility limits of chromium in iron and of iron in chromium, as shown in figure I.16 [MAE 14].

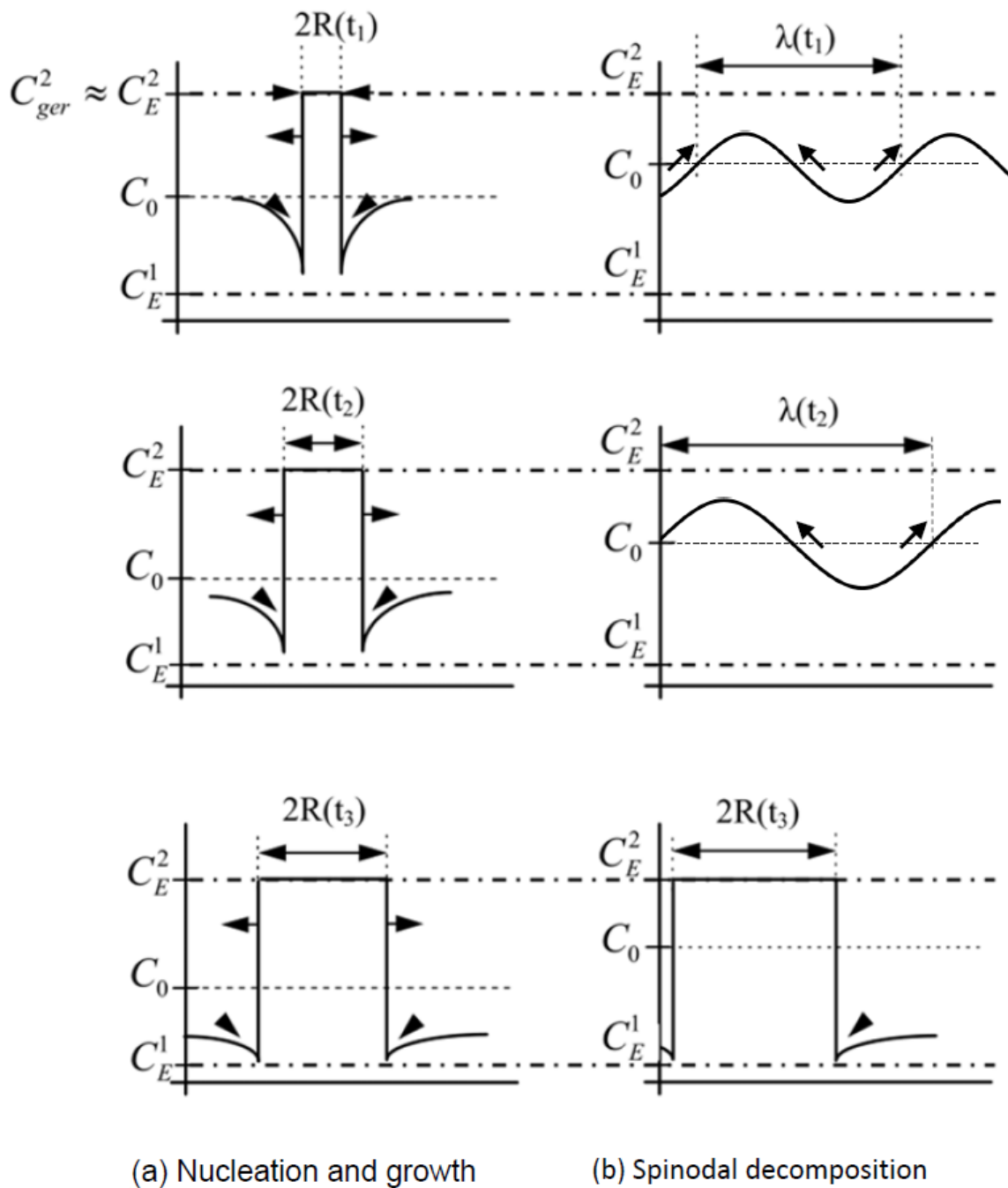


Figure 1.16 : Formation of precipitates by a classical mechanism of nucleation and growth or by spinodal decomposition. C_0 , C_E^1 and C_E^2 are respectively the initial composition of phase 1 and the equilibrium compositions of phase 1 and phase 2. R is the radius of the nuclei then of the precipitates and λ is the wavelength of the fluctuations [MAE 14].

It is well documented in literature that the spinodal decomposition of ferrite into chromium-rich (α') and iron-rich (α) phases at intermediate temperatures is the primary mechanisms of thermal embrittlement of DSS [CHU 90, LEA 92, CHU 92, WEN 04, PAR 15].

5.2 Activation energy of ferrite spinodal decomposition:

The unmixing of ferrite by spinodal decomposition is considered as a thermally activated mechanism that follows the Arrhenius law. The activation energy “ Q ” related to this decomposition process has been extensively studied by many researchers using different methods. A critical review of several methods had been carried out by Chung to explain the complex behavior of activation energy of decomposition process [CHU 92].

The great importance allocated to this parameter is justified by the fact that this activation energy “ Q ” is essential for design life prediction of DSS components operating at high temperature particularly in nuclear and petroleum industries. In fact it is generally accepted that the activation energy measured for the embrittlement process is consistent with that derived from hardening kinetics in ferrite, and in agreement with the development of the spinodal reaction in the ferrite phase [MEY 11].

Information obtained at a number of laboratories shows, however, that the activation energy of aging embrittlement is strongly influenced by nominally small differences in chemical composition and fabrication process, and a consensus among investigators on the understanding of the activation energy of aging has not been reached yet [CHU 92].

The activation energy determined by Pareige et al [PAR 11] for this mechanism is approximately equal to 243 ± 80 kJ/mol, consistent with the activation energy for the diffusion of chromium in iron ($Q = 250.3$ kJ/mol [MEH 90]).

Meyer et al [MEY 11] studied the relationship between the chemical composition of ferrite and embrittlement, through resilience measurements on six different commercial duplex steels, aged between 250 °C and 400° C. The activation energies determined by this research group from these measurements are between 100 kJ/mol, for the low alloyed steels and 300 kJ/mol for the high alloyed steels. They therefore established a correlation between the chemical composition of the ferrite of the various steels and the activation energies associated with embrittlement phenomena, and Q (in kJ/mol) follows an empirical law of type:

$$Q = -64 - 2\%Cr - 49\%Si - 5\%Mo - 11\%Cu + 33\%Ni + 64\%Mn + 4123\%N \quad (I. 22)$$

In the current study, the activation energy has been determined using DSC technique. During our literature survey, we have found only one research work published in 2014 [COU 14], in which DSC technique was used to follow the embrittlement kinetic for a precipitation hardening stainless steel grade (15-5 PH grade).

In our study, a simplified method was used. DSC curves were analyzed through Kissinger equation, modified by Mittemeijer et al. [MIT 88, RIV 18] :

$$\ln\left(\frac{T_p^2}{S}\right) = \frac{Q}{R.T_p} + \ln\left(\frac{Q}{R.k_0}\right) \quad (1.23)$$

where T_p = peak temperature (K); S = heating rate (K/S); Q = effective activation energy for the process associated with the peak (J mol⁻¹); R = gas constant; k_0 = pre-exponential factor in the Arrhenius equation for the rate constant k :

$$K = k_0 \cdot \exp\left[-\frac{Q}{R.T}\right] \quad (1.24)$$

Further details and results are presented with discussions on Chapter 3.

6. Solution annealing heat treatment:

To overcome the problem of intermetallic precipitation, the DSS are often supplied in the solution annealed condition. The aim of the this treatment is to dissolve the secondary phases that can precipitate during hot working or welding.

The figure I.17 provides a typical thermal cycle of Solution annealing heat treatment, the cooling should normally be as fast as possible; air cooling is normally fast enough but water quenching can be necessary for certain grades.

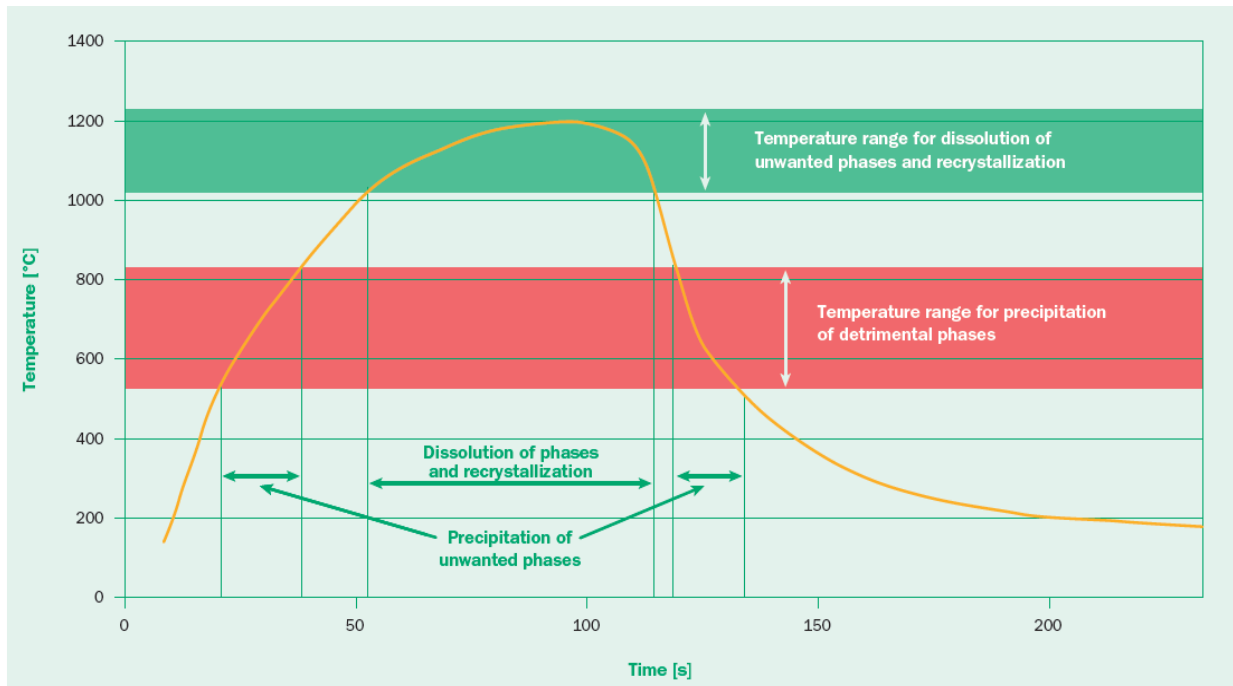


Figure III.17: Example of a solution annealing cycle. The critical temperature ranges are strongly dependent on the steel grade [OUT 13].

7. Pitting corrosion properties

One of the most common types of corrosion phenomenon in stainless steels is pitting corrosion, which is introduced in this section. In the presence of mechanical stresses, this form of damage has been observed to potentially lead to the development of stress corrosion cracks (SCC), thus degrading the structural properties of components [GHA 15].

Furthermore, it has been reported that almost 30% of cases of the corrosion failures in power stations is caused by localized corrosion including pitting and stress corrosion cracking (SCC). Once these damage processes initiate they will allow the material to deteriorate, leading to catastrophic structural failure, resulting in plant shutdown and economic losses [SAI 07].

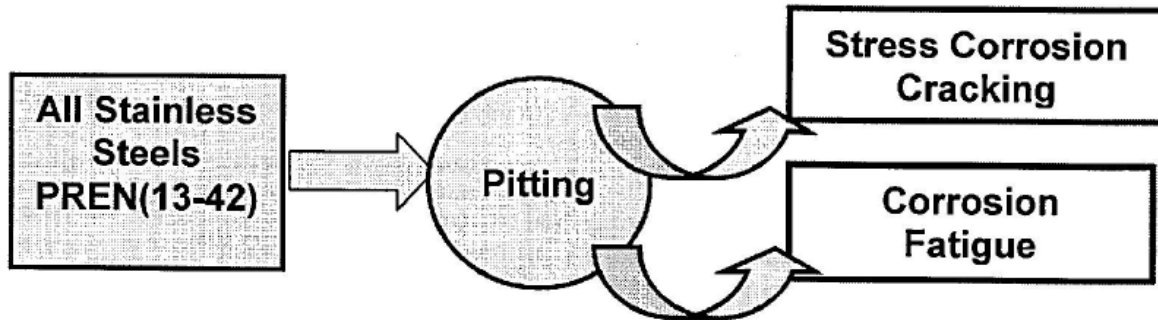


Figure I.18: Schematic diagram of the role of pitting [SAI 07].

The more the stainless steel is resistant to pitting the better it is for long term applications as pitting aggravates both stress corrosion cracking (SCC) and corrosion fatigue (CF) cracking which leads to the failure of engineering equipment.

Therefore, these failures are serious and important.

7.1 Mechanism and Stages of Pitting Corrosion

Stainless steels are protected from corrosion by a naturally formed passive film on the surface. In the presence of chloride ions, however, stainless steels are susceptible to localized corrosion such as pitting corrosion.

The mechanism of pitting corrosion had been widely studied in the literature. Almost all pits initiate at some chemical or physical heterogeneity at the surface such as an inclusion, second phase particles, mechanical damage, solute-segregated grain boundary or dislocation.

As the passive film or any another protective surface layer breaks down locally, pitting corrosion normally takes place. An anode forms where the film has broken, while the unbroken surface film acts as a cathode. In this case the localized attack will be accelerated and pits will develop at the anodic spot. The environment within the pit may become very aggressive which will further accelerate corrosion. A typical schematic for pitting corrosion process is presented by Figure I.19 [SAU 11].

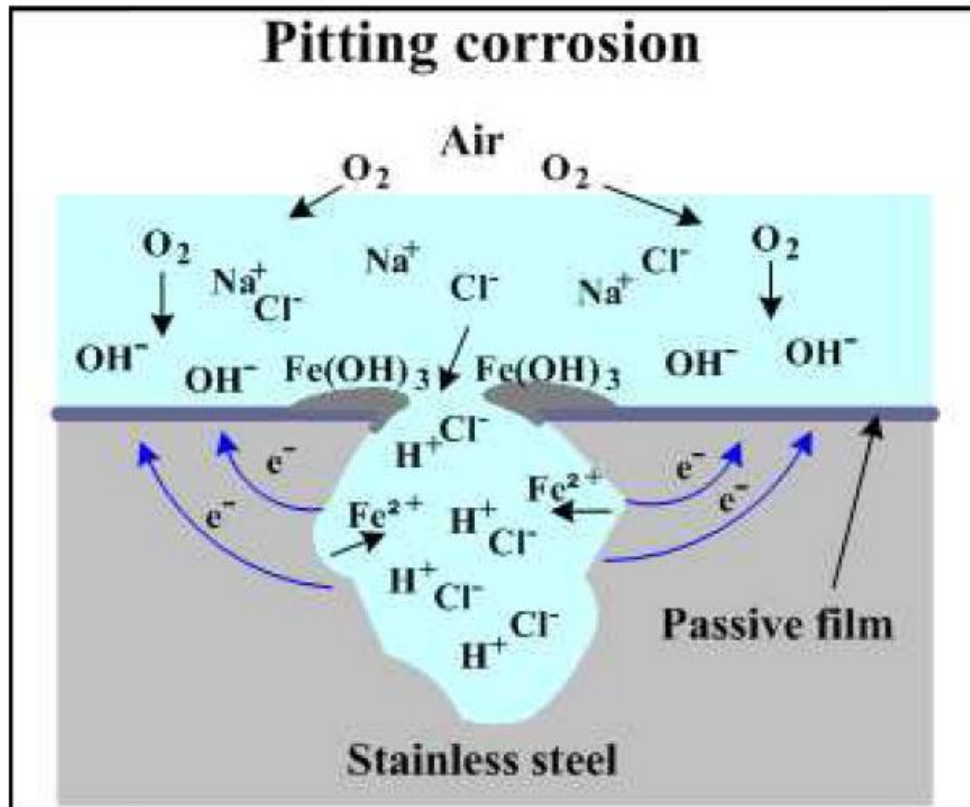


Figure I.19: typical schematic for pitting corrosion process [SAU 11].

The pitting corrosion process can be divided into two main stages :

1. Pit initiation stage (passive film breakdown) and
2. Pit propagation stage.

Some typical morphologies of pitting corrosion of DSS samples are shown in **Annex A**.

7.2 Pitting potential

It is generally accepted that pitting initiates when the pitting potential reaches a critical value (E_p), which depends on the chemical composition of the alloy and on the environment (temperature and chloride concentration). E_p is often measured by potentiodynamic anodic polarization tests. In these measurements the onset of pitting corrosion is observed as an irreversible increase in current density (Figure I.20). The higher the E_p value, the more resistant is the alloy to pitting corrosion in the environment considered [POH 08, CER 10].

This value can be measured in the environment of interest for example in aqueous chloride, bromide, iodide and even in sulphuric acid solution. The values obtained depend on the composition and structure of the metal and the tests environment. Measuring the potentials when the pits tend to cause damage is useful for selecting materials for various applications [SAI 07].

The figure I.20 explains a lot of terms related to the pitting behavior of stainless steels. In the active anodic region, the measured current tends to increase with the applied potential and then starts to decrease at a potential called the primary passivation potential E_{pp} . The occurrence of this is known as the active-passive transition. Above this potential the current usually drops to a low value and becomes nearly stable with increase in applied potential called as passive current, i_{pass} . The potential range over which the current remains at low value is called the passive potential range and it is a range where stainless steels remains passive and the corrosion rate is low.

On increasing the applied potential towards positive direction, there exists a critical potential where the current tends to increase with the applied potential this potential is termed as pitting potential, E_p or breakdown potential, E_b . This particular potential value is defined by the combination of alloy and environment [SAI 07].

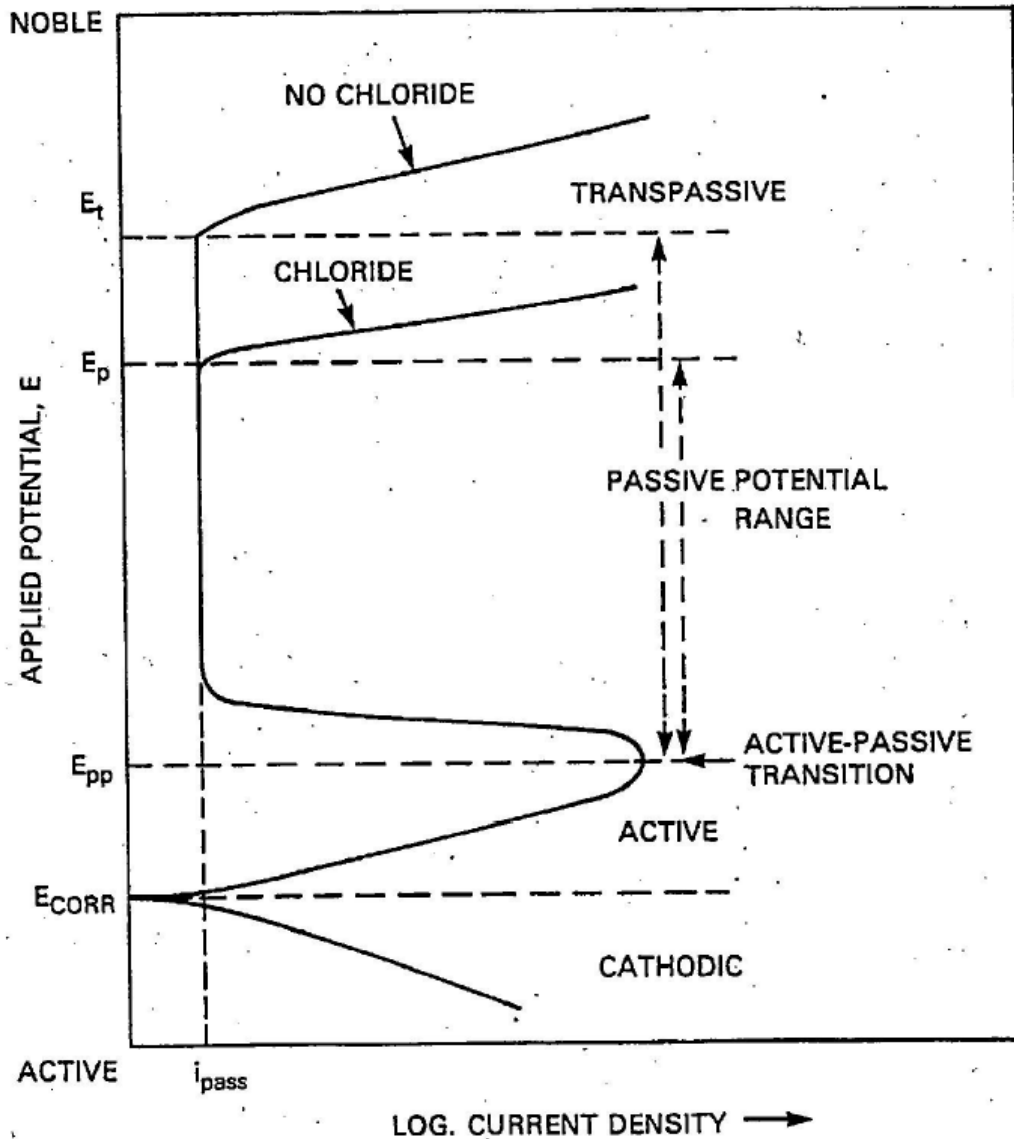


Figure I.20: Schematic polarization curve for a stainless steel in a sulphuric acid solution [SAI 07].

7.3 Relationship between E_p and PRE_N

Although that the PRE_N is not an absolute as we already mentioned, some authors attempted to correlate between the PRE_N and E_p in some specific environments. Some of their findings are presented in this section.

Truman [TRU 87] in his study mentioned the relationship between alloy content and pitting potential is not linear, involving a transition above a certain PRE_N value, which is due to the addition of chromium, molybdenum, and nitrogen individually or in a combination as shown in Figure I.21 [SAI 07].

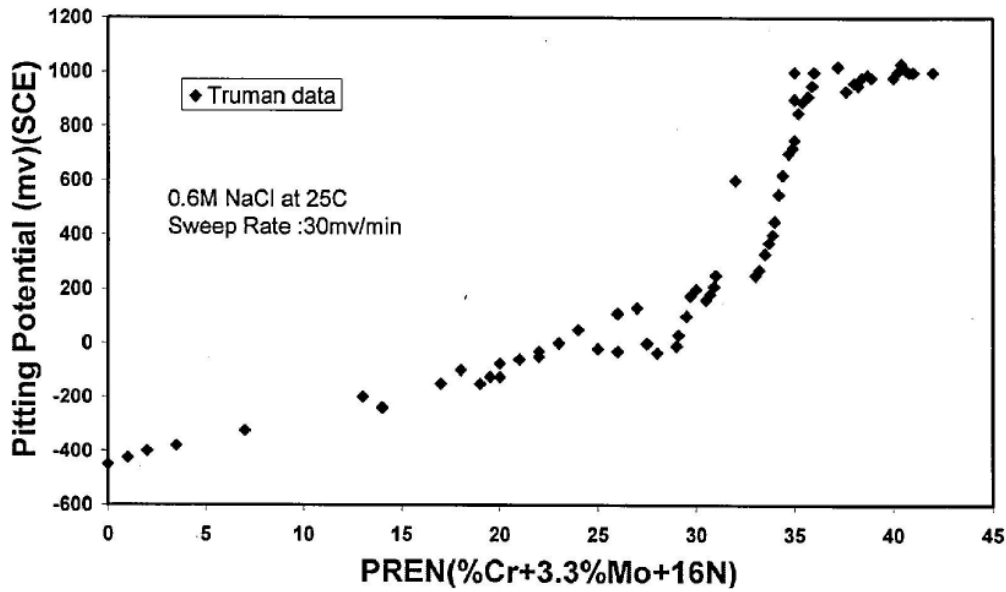


Figure I.21: Relationship between E_p & PRE_N [55].

As shown in this figure the transition occurred around PRE_N value of 32 which suggests that increase in alloying elements does increase the pitting resistance. But the increase in PRE_N is directly related to the increase in cost. So, it was not always a good idea to enhance the composition as it becomes very expensive product. Among the expensive compositional elements nickel tends to be at higher price so the stainless steel makers found an alternative solution by adding nitrogen and molybdenum.

Lorenz and Medawar studied the effect of chromium and molybdenum on several alloys in artificial seawater and proposed a following relationship between pitting potential, and these alloying elements as [SAI 07]:

$$(1200 - E_p)^2 = 2.54 \cdot 10^{-6} - 90 \cdot 10^3 \cdot (\%Cr + \%Mo) \quad (I.25)$$

Merello et al [MER 03], studied some duplex steel samples in NaCl solution at 25°C and found an exponential relationship between the pitting potential and the PRE_N as given below:

$$E_p = 2.94 \cdot \exp[0.14 \cdot PRE_N] \quad (I.26)$$

7.4 Effect of secondary phases on pitting potential

The protectiveness of passive film depends greatly on the Cr, Mo and N contents. In particular, Cr and Mo in the passive film act synergistically in resisting the attack of chloride ions by rehealing damaged film. When secondary phase particles and chromium carbides are formed at the grain boundaries of DSSs, the boundaries adjacent to the precipitates are depleted of Cr and Mo. The Cr/Mo-depleted zone near the grain boundaries is much less corrosion resistant than the surrounding grains. Thus the film locally is less protective and the Cr/Mo depleted zone experiences active dissolution (act as the anode) and corrode upon exposure to corrosive environment, while the surrounding grains remain in the passive state (act as the cathode).

Furthermore, the precipitation of secondary phase particles can cause compositional changes in the α - and γ -phases, resulting in selective pitting corrosion of a weak phase [KAI 14].

Domínguez-Aguilar and Newman studied the deleterious effects of secondary phase formation on the pitting behavior of a 25Cr duplex stainless steel exposed to a halide solutions (NaBr, NaCl) at different temperatures (20–50 °C) [DOM 06]. The steel was aged at 675–825 °C for different periods to induce the formation of χ and σ phases. As mentioned above, Mo promotes the formation of χ - and σ -phases in DSSs in which the χ -phase nucleates in the early stage of aging. In both halide solutions the presence of intermetallics leads to pitting corrosion. The Cr/Mo depleted zones are preferred dissolution sites in halide solutions. The passive films formed on these zones are less protective because they are depleted of Cr and Mo.

Hence, the correlation between pitting potential and σ -phase volume fraction has shown a shift of pitting potential to more active region as the σ -phase content increases [DOM 06, KAI 14].

D.C. Dos Santos et al [SAN 16] investigated the correlation between the pitting potential and sigma phase volume fraction for isothermally aged DSS at 850°C for different aging time. The aged steel was analyzed through cyclic potentiodynamic polarization tests in 0.6 M sodium chloride (NaCl) solution. It was established that Both pitting and repassivation potentials decreased with an increase of sigma volume fraction and this was attributed to the increase of secondary chromium-depleted phases formed in consequence of sigma phase formation.

Other researchers [PAR 15, EBR 12, YOU 11, DEN 09] have correlated the influence of sigma phase on pitting resistance through the Critical Pitting Temperature (CPT). The CPT is the lowest temperature at which stable pit formation is initiated [PRA 15].

For example, Park et al. carried out a study on effect of sigma phase precipitation on DSS in 10% $\text{Fe}_3\text{Cl}\cdot 6\text{H}_2\text{O}$ solution. They allowed sigma phase precipitation by different aging treatments and found that CPT value decreases with increase in σ -phase precipitation [PAR 05, PRA 15].

However, the numerical data relating sigma phase content to the pitting potential are limited. Furthermore, most of the available studies have been conducted using a various electrochemical tests in chloride containing solutions (NaCl, CaCl_2 ,...). Additionally, there is no published studies examining the electrochemical behavior of sigmatized DSS when exposed to oil and gas field environment. There have been only a limited number of studies related to Super Duplex stainless steel (SDSS) materials tested in a simulated oil field environment [SAI 12].

Hence, as part of the current study, the relationship between sigma phase content and pitting potential values have been investigated in Produced water solution. The details of experiment are described in next chapter.

Conclusion

The literature review reported on this chapter served to highlight some of the technical aspects that need to be further investigated due to the limited available information on those topics.

Therefore, among the interesting topics handled under the current research work, the following are listed:

- (1) Study sigma phase precipitation in DSS aged at 850°C and its effects on mechanical proprieties.
- (2) Apply the classical and modified JMA model to follow sigma phase precipitation process.
- (3) Investigate sigma effect on pitting corrosion in a “Real” oil field solution, which is Oily Produced Water solution.
- (4) Apply DSC technique to determine the activation energy “Q” related to the 475°C embrittlement (spinodal decomposition).



EXPERIMENTAL TECHNIQUES

1. Introduction:

In this chapter we will present in a first step the investigated material in the current study, namely its chemical and mechanical characteristics, material shape and delivery conditions. A typical materials selection flow diagram for stainless steels for process piping is presented to give an overview on how oil and gas operators select DSS in petroleum industry.

The other sections of this chapter are dedicated for the presentation of the experimental procedures, applied heat treatment to produce sigma phase, together with the characterization techniques and tests employed to achieve the objectives of this project.

2. Material presentation:

The investigated steel grade in this study is a duplex stainless steel (ASTM 790 UNS 31803) received in the solution treated condition, as a seamless pipe having a 3 inch diameter and 5.5mm thickness. The pipe has been supplied by TUBACEX TUBOS INXIDABLES, S.A. to SONATRACH (Oil and gas Operator) in order to be installed in an oil and gas plant in south of Algeria).

This material grade of this pipe has been selected by the engineering company providing the technical support to SONATRACH in order to be used for various process systems, where the temperature exceeds 60°C in chloride containing environments, like salt crude oil and oily produced water.

The flow diagram used for this material selection is shown in figure II.1.

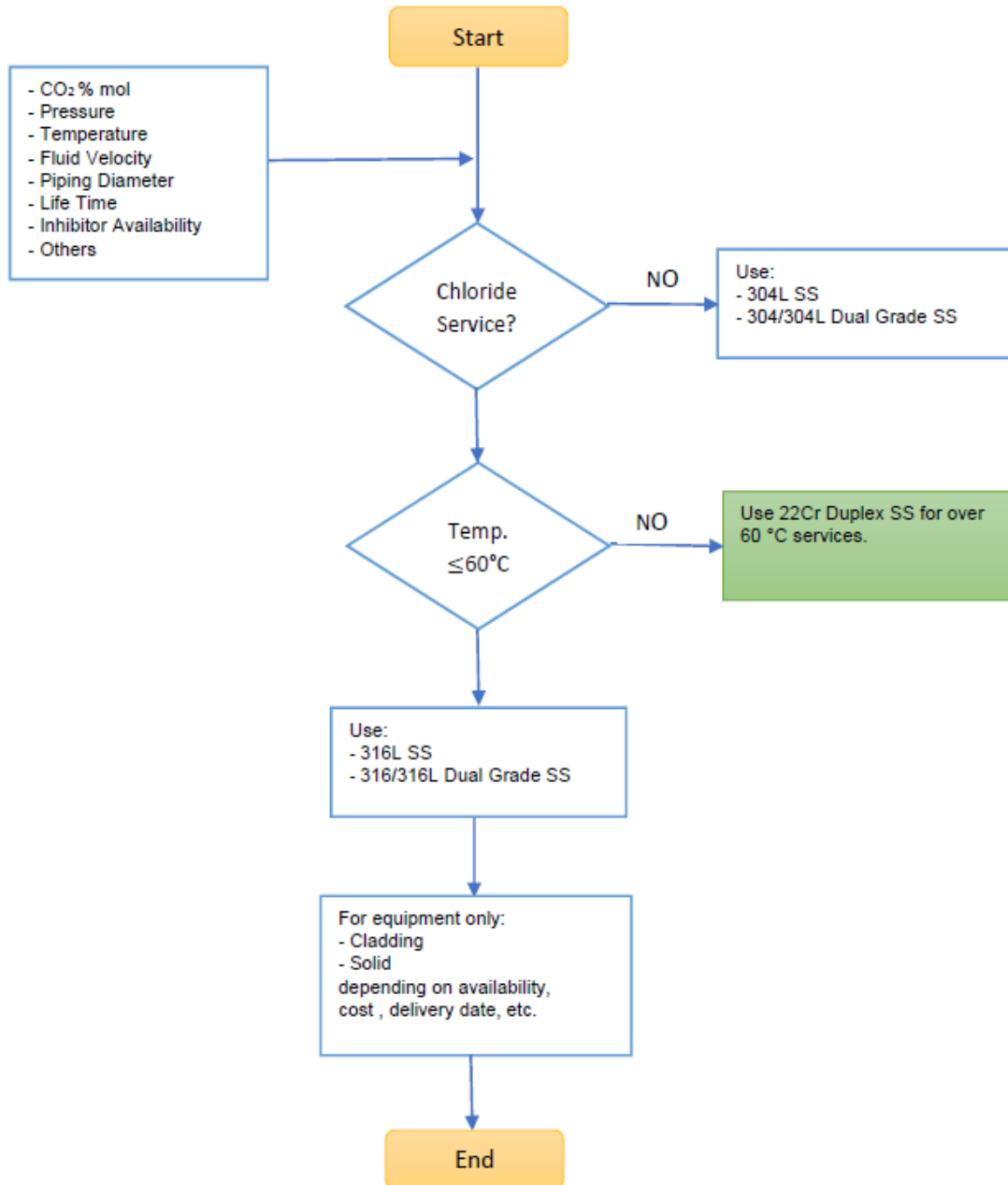


Figure II.1: Flow Diagram for Stainless Steel Materials Selection for Process Piping.

2.1 Chemical composition

The chemical composition of this pipe is given in Table II.1.

Table II.1: Chemical composition of the studied Material.

Elements	C	Si	Mn	P	S	Cr	Mo	Ni	N
wt. (%)	0.013	0.550	1.100	0.0260	0.0006	22.400	3.150	5.450	0.1850

2.2 Mechanical characteristics

The mechanical characteristics are given in table II.2 below, where the parameters $R_{p0.2}$, R_m and A_5 are as defined in the figure II.2.

Table II.2: The mechanical characteristics of the investigated DSS.

Test Temperature	Yield Strength $R_{p0.2}$ (MPa)	Tensile Strength R_m , (MPa)	Elongation, A_5 (%)	Hardness (HRC)
20°C	487	568	44%	16

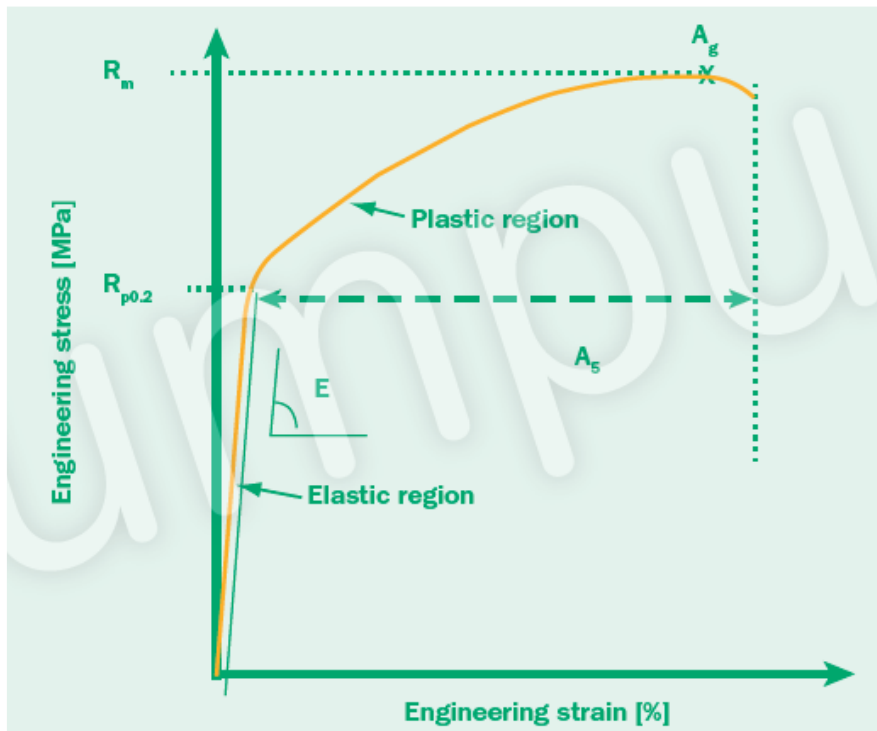


Figure II.2: Some definitions from the stress strain curve [OUT 13].

3. Heat Treatment (Aging) program:

The aim of heat treatment in this study was to study sigma precipitation mechanism and to produce various level of sigma content in the investigated alloy, then study the effect of these various content on the corrosion and mechanical features. Therefore, Specimens of approximately 20 mm length and 10 mm wide were obtained. A number of samples were kept without any treatment as reference, and the rest of specimens were isothermally aged at 850°C for different holding times ranged from 5 minutes to 360 minutes, in a tubular electric furnace equipped with a temperature controller. At the end of each treatment the specimen

was immediately water quenched in order to interrupt the phase transformation process (Figure II.3).

The aging temperature of 850°C was selected in this study as it presents the nose of sigma C curve for the UNS 31803 DSS[MAG 09, CHI 12].

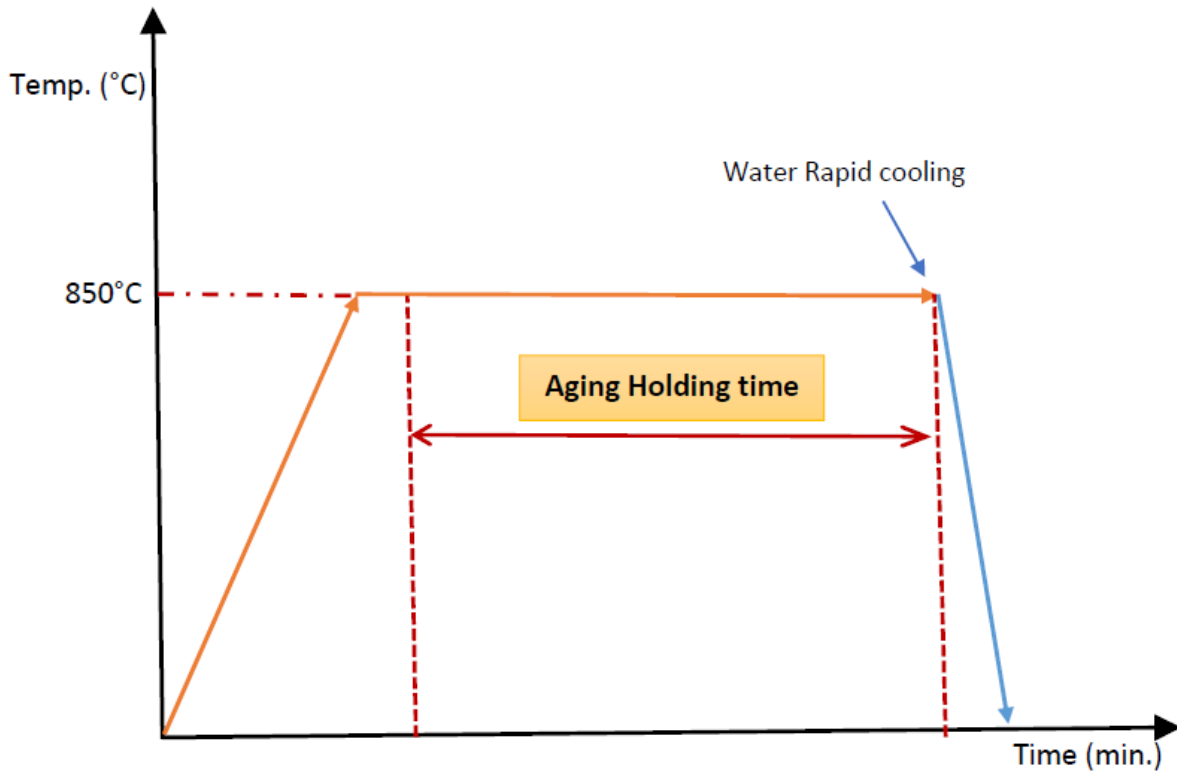


Figure II.3: scheme of applied aging treatment.

4. Metallographic examinations

The specimens for metallography were prepared in the following manner: samples were mounted in acrylic moulding powder. Then all the specimens were ground on silicon carbide paper down to 1200 grit size and then polished with alumina powder. Finally, the specimens were thoroughly cleaned with running cold water and dried.

Metallographic examinations have been carried out using electrolytic etching under the following conditions:

- Solution : oxalic acid aqueux à 10 % (weight),
- Tension : 2 to 2.5 V,
- Electrodes : Duplex SS,
- Etching Period: 10 to 20 seconds [VIL 06].

This procedure has the advantage to allow quantitative metallographic analysis of sigma phase. The electrolytic etching employed colors the phases as follows: ferrite-gray, austenite – white, and sigma phase - dark.

Other alternative etching agents recommended for DSS are provided on **Annex A** for information purpose.

The etching cell is illustrated in figure II.4.

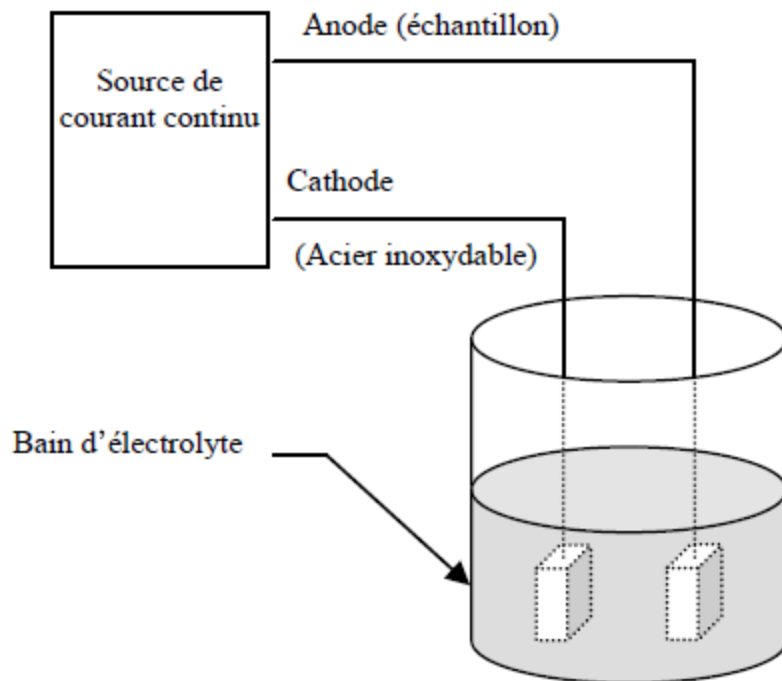


Figure II.4: Schematic for electrolytic etching cell.

5. Microhardness Measurements

The surfaces of the specimens were polished before measuring their hardness.

A Vickers microhardness testing machine with a diamond indenter was used. Vickers microhardness measurements were performed using 0.3 kg load.

At least fifteen readings were recorded for each specimen and an average value calculated.

Figure II.5 shows Vickers microhardness principle, while figure II.6 shows the used apparatus.

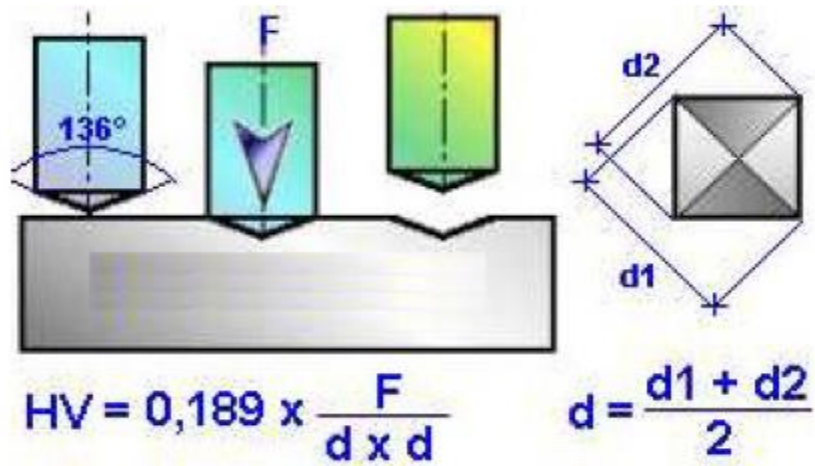


Figure II.5: Vickers Microhardness test principle.



Figure II.6: Microhardness apparatus.

6. X-ray diffraction analysis

The presence of different phases in the specimens was also identified by X-ray diffraction analysis (XRD).

X-ray diffraction is probably the most commonly used analytical technique for phase identification. The working principle is based on diffraction of X-rays (Figure II.7) as described by the Bragg's law :

$$n\lambda = 2 \cdot d \cdot \sin(\theta)$$

Where n is the diffraction order, λ is the wavelength of the X-ray source, d is the diffraction interplanar distance and θ is the diffraction angle [MAI 18].

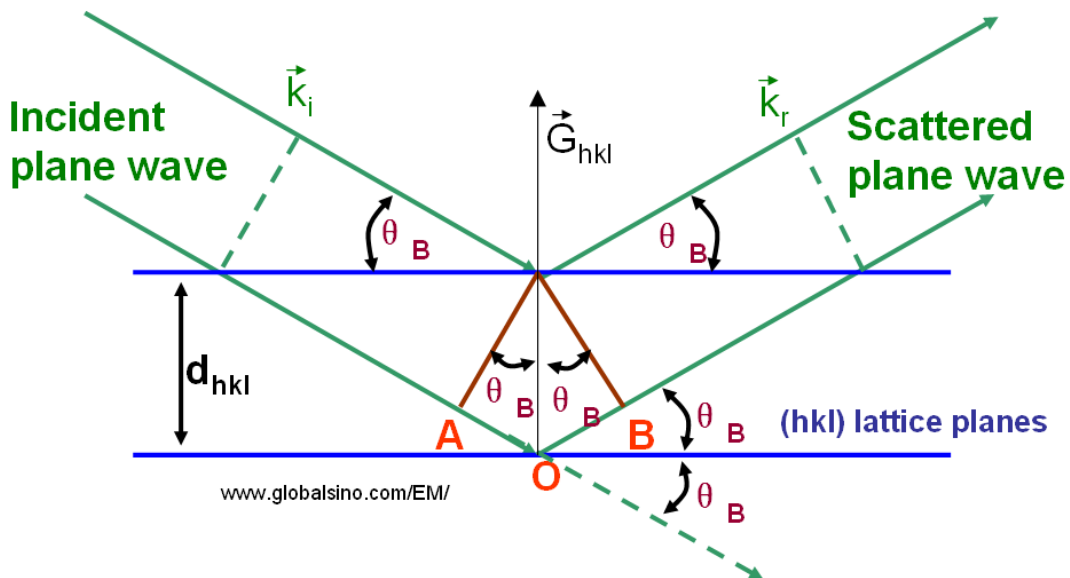


Figure II.7: Schematic illustration of Bragg condition and Bragg's law [GLO 20].

Phase identification is performed by measuring the angles where constructive interference of X-rays is located and then converting into interplanar distance. Sets of diffracting planes are then matched with those from the standard database (Powder Diffraction Files from the International Centre for Diffraction Data).

From sets of interplanar distances it is then possible to calculate the lattice constants, which for cubic systems is :

$$1/d^2 = (h^2 + k^2 + l^2)/a^2$$

Where hkl are the Miller indexes [MAI 18].

X-ray diffraction analysis was carried out on a Bruker D8- Advanced diffractometer (Figure II.8) using monochromatic CuK_{α} radiation ($\lambda = 1.54056 \text{ \AA}$) with an accelerating voltage of 40 kV and current 40 mA, angular range 40° - 70° .



Figure II.8: Bruker D8- Advanced diffractometer.

7. Scanning electron microscopy (SEM)

Complementary microstructural characterizations using scanning electron microscope (SEM) have been used for a number of aged samples for further confirmations purpose.

Scanning electron microscopy (SEM) has been of paramount importance in materials science thanks to the small wavelength of the electron beam, which offers significantly higher spatial resolution compared with Light optical microscopy (LOM). In addition, backscattered electron imaging provides composition contrast on different phases present in the material without etching procedure.

In SEM, electrons are generated by a source (tungsten, LaB_6 or field emission gun) and accelerated through apertures at potential of several keV. The electron beam is then

collimated and focused by means of several electromagnetic lenses and is scanned on the specimen. High vacuum is necessary to increase electron mean free path, allowing high resolution [MAI 18].

The electron beam interacts with matter producing a number of signals that can be detected by different detectors. Secondary electrons are generated by ionization of the atoms composing the material. Having low kinetic energy, they can only escape from the depths in the order of ~ 100 nm (Figure II.9), providing valuable information on the topography. Backscattered electrons, instead, result from the elastic scattering of the primary electron beam, being highly energetic.

The information volume is therefore larger and corresponds to ~ 1 μm . The backscatter yield is dependent on the atomic number of the elements present in the material. Heavy elements backscatter electrons more strongly than light elements, therefore providing composition contrast [MAI 18].

In the current study, imaging was carried out in a JEOL microscope operated from 7.0 to 30kV.

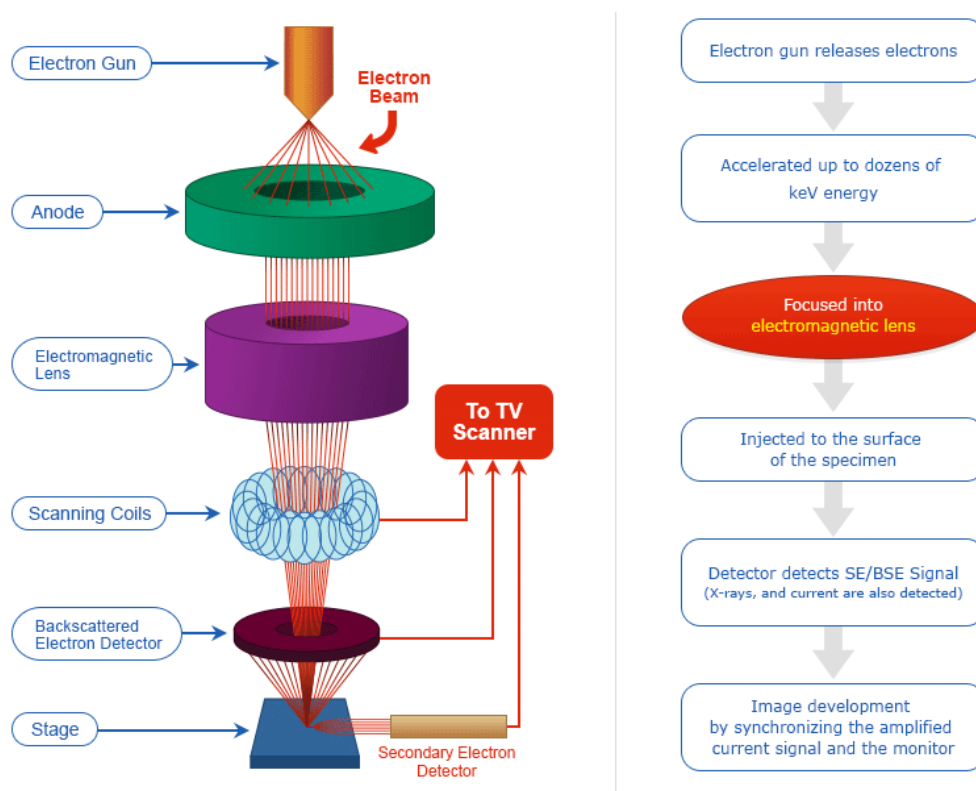


Figure II.9 : Schematic diagram of major components of SEM [NAN 20].

8. Differential Scanning Calorimetry (DSC)

Differential scanning calorimetry (DSC) is a method that is extensively used to measure heat and temperatures of various transitions and has been recognized as a very useful tool for the interpretation of thermal events. It has been widely used to research different phase transformations of steels and alloy materials by several authors [KAS 17, LON 18, REN 11].

A calorimeter measures the heat into or out of a sample. A differential calorimeter measures the heat of sample relative to a reference. A Differential Scanning Calorimeter does all of the above and heats the sample with a linear temperature ramp. DSC is a technique in which the difference in the amount of heat required to increase the temperature of a sample and reference are measured as function of temperature. Both the sample and reference are maintained at nearly the same temperature throughout the experiment. Generally, the temperature program for a DSC analysis is designed such that the sample holder temperature increases linearly as a function of time [KOD 14].

The heat flow signals measured by DSC can provide valuable kinetic information about the phase transformation and the phase precipitation and dissolution in the materials during a specific heating and cooling cycle. Moreover, DSC has two important advantages. First, it is an effective and rapid experimental tool to measure the onset temperature and the finish temperature with high precision during phase transformation in a well-defined small sample. Second, the energy absorbed (endothermic peaks) and energy released (exothermic peaks) during the specific heating and cooling cycle are directly correlated with the phase volume fraction of precipitates and the composition of materials [LON 18].

In practice, the heat is supplied to the sample contained in the pan, and similarly, to the reference in its pan.

Two types of DSC are recognized [HAI 95]:

- 1) **Power-compensated DSC**, where the sample and reference are heated by separate, individual heaters, and the temperature difference is kept close to zero, while the difference in electrical power needed to maintain equal temperatures $\Delta p = d(\Delta Q/dt)$ is measured.

Figure II.10 shows a simplified schematic diagram of the power compensated DSC cell.

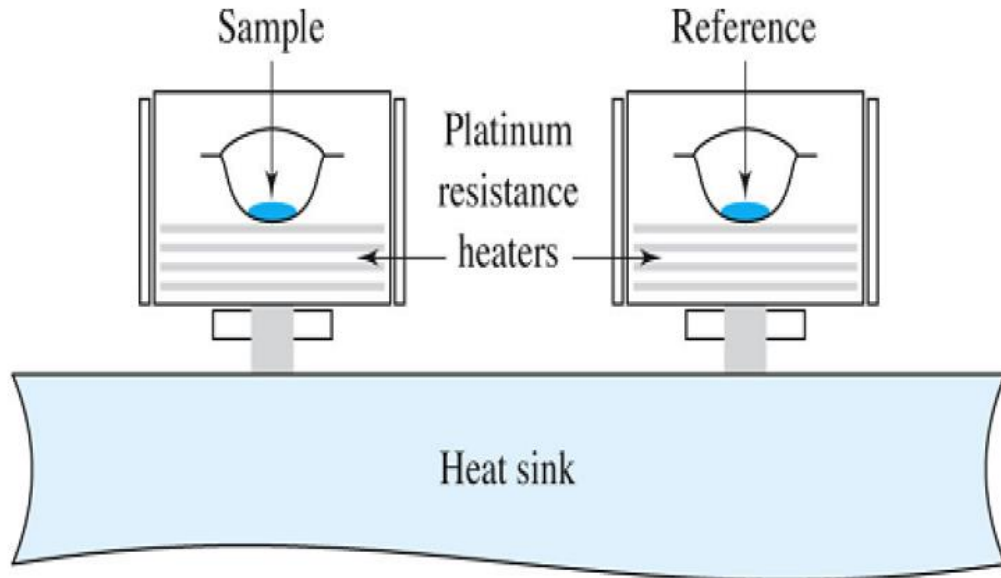


Figure II.10 :Schematic illustration of power compensation DSC [KOD 14].

- 2) *Heat-flux DSC*, where the sample and reference are heated from the same source and the temperature difference a ΔT is measured. This signal is converted to a power difference a ΔP using the calorimetric sensitivity.

Figure II.11 shows a simplified schematic diagram of the heat-flux DSC cell.

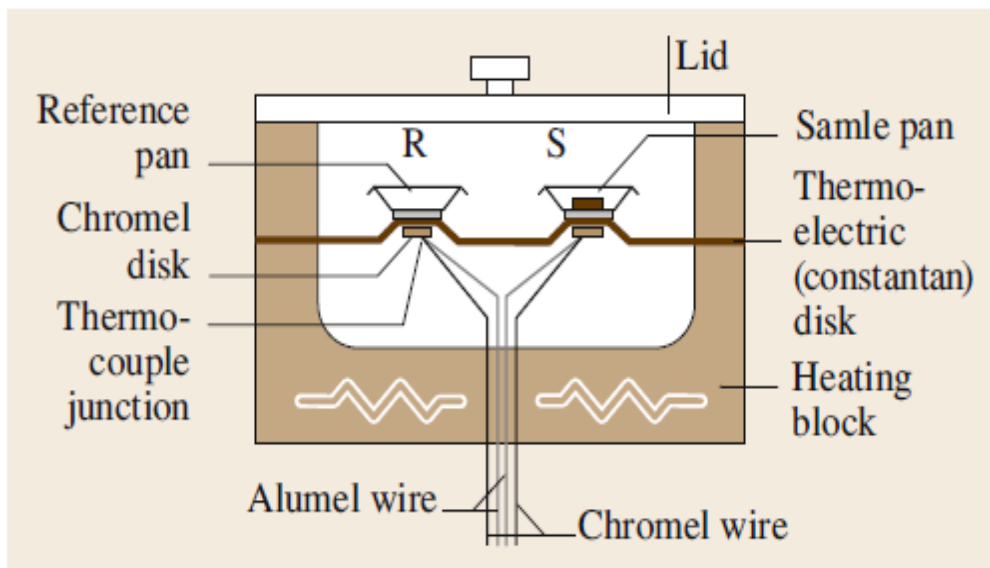


Figure II.11 :Schematic illustration of heat-flux DSC cell. R and S refer to reference and sample pans [KAS 17].

A typical example of a DSC scan performed for a low alloy steel is shown in Figure II.12.

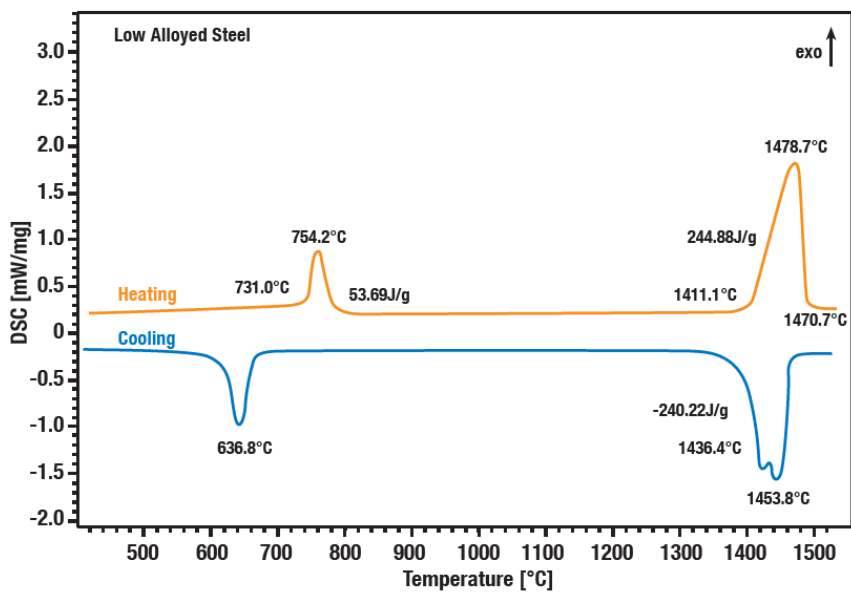


Figure II.12: Typical DSC signal for a Low Alloy Steel [LIN 20].

Figure II.13 shows the photo of the DSC apparatus (Q20) used in this study.



Figure II.13: photograph of the DSC Q20 used in this study.

9. Corrosion Tests and pitting potential measurement:

Localized corrosion (Pitting) tests were carried out to determine the susceptibility of stainless steels to pitting using polarization potentiodynamic technique. The main advantage of with this kind of testing is the opportunity to investigate corrosion phenomenon in the solution of interest. The parameters that was evaluated from these tests is the *Pitting Potential*.

In fact, pitting potential is defined in several ways. In the current study, Pitting Potential (E_p) is defined as the potential corresponding to an abrupt increase of the current above the passive current with increasing potential. This concept of a pitting potential or breakdown potential was proposed by Brenner in 1935 for alloy steels, which characterizes the behavior of passivable metals and alloys in chloride solutions [SAI 07].

Figure II.14 illustrate the method of determination of E_p that we adopted in this work.

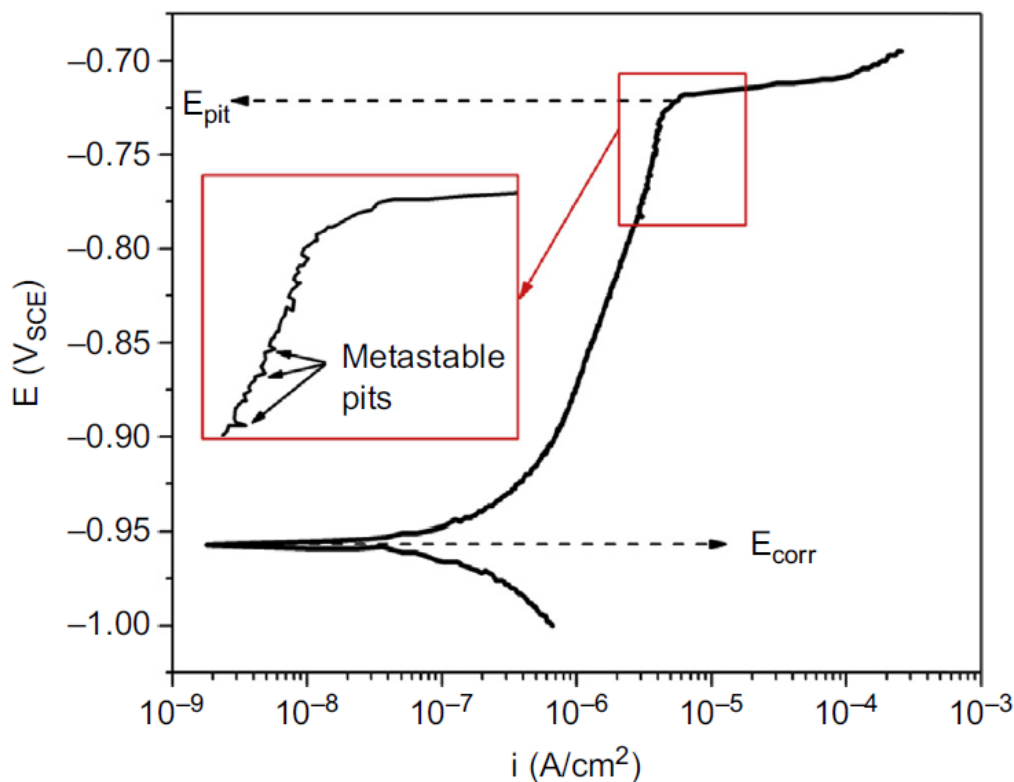


Figure II.14: Principle of determination of pitting Potential (E_p) [OBE 17].

9.1 Potentiodynamic polarization:

Potentiodynamic polarization technique has been in practice for long time and was known to be reliable and most useful approach to make current-potential measurements. This technique

only indicates the relative resistances to pit initiation but has the advantage of giving results in a reasonable time period.

The polarization tests were carried out using a potentiostat *VOLTALAB PGZ-301* consisting of three electrodes. Platinum was used as the counter electrode and saturated calomel electrode (SCE) was employed as the reference electrode. The specimens acting as working electrode were embedded in epoxy resin with an approximate exposure area of 1cm^2 . Before each test, the exposed surfaces of samples were polished up to 4000 grit finish then rinsed with distilled water and dried in air.

Figure II.15 shows a schematic of polarization cell (potentiostat) used for corrosion test.

Figure II.16 shows the polarization cell (*VOLTALAB PGZ-301*) potentiostat used in this study.

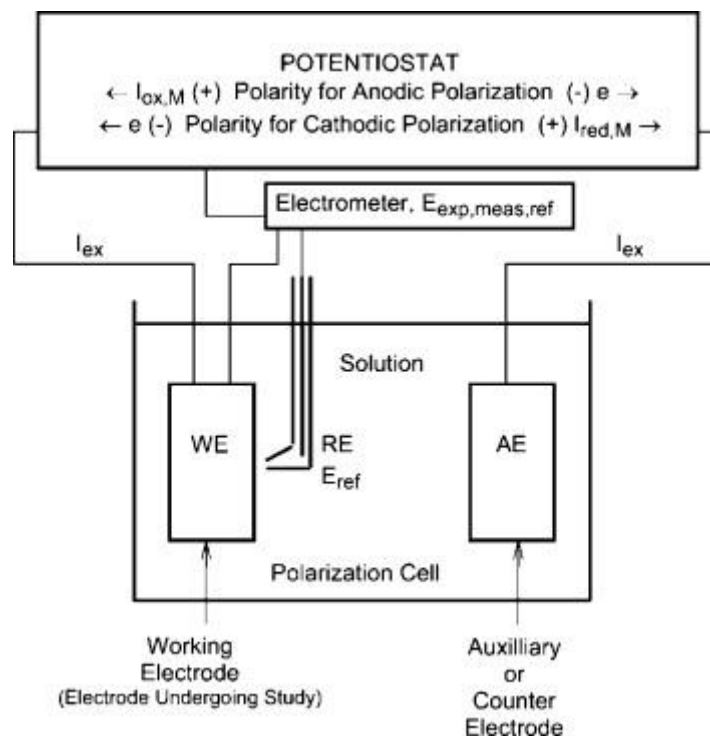


Figure II. 15: Schematic of the electrochemical cell used for corrosion testing [BUC 12].



Figure II. 16: The VOLTALAB PGZ-301 potentiostat.

9.2 Scan rate:

All the potentiodynamic tests can be conducted at different potential scan rates but how far these scan rates influence the pitting initiation is not yet clear [SAI 07].

However, influence of scan rate has been summarized by Smialowska and was reported that scan rate does have influence on the pitting potentials for, high chromium and molybdenum steels, whereas in case of ferritic steels it did not show significant effect [SMI 86, SAI 07].

However, in this study scan rate was based on the most published works in same field of research. The potentiodynamic measurements were performed at a scan rate of 1mV/S until an anodic current of 100 μ A/cm² was exceeded [MOU 08, DON 11, EBR 11, SAN 13].

9.3 Test Solution:

Two test solutions have been used in this study: Produced Water solution and 0.5 M NaCl solution simulating seawater chloride concentration.

Tests solutions were exposed to laboratory air at room temperature (approximately 25 °C).

Produced Water is the recovered water from crude oil production system after separation and filtration. Treated produced water is sent for reinjection into the oil reservoir to increase the oil recovery capacity. The chemical analysis of the produced water used as a test solution for this study is presented in Table II.3.

Table II.3: Chemical Analysis of Produced Water

Elements	Cl ⁻	HCO ₃ ⁻	Na ⁺	Ca ⁺⁺	K ⁺
Concentration (mg/l)	28862	61	30765	97	418

Simulated seawater solution was prepared to achieve a chloride level approaching to the chloride level (salinity) of seawater. The salt was weighed and was calculated to prepare required levels of chloride solution from NaCl, then it was mixed in demonized water.

9.4 Sample identification

Tested samples in simulated seawater were numbered from "0-SW" to "360-SW" whilst the tested samples in produced water were numbered from "0-PW" to "360-PW", where the numeric characters denote the aging time in minutes. Based on that, specimen identification adopted in this work are listed on Table II.4. After the polarization tests, the surface of the pitted samples were cleaned and analyzed using SEM observation to examine pit morphology and preferential location.

Table II.4 Specimens identification

Aging Time (min)	Test solution	Identification
0 (Solution annealed condition)	Simulated Seawater	0-SW
5		5-SW
30		30-SW
60		60-SW
360		360-SW
0 (Solution annealed condition)		Produced Water
5	5-PW	
30	30-PW	
60	60-PW	
360	360-PW	

9.5 Pitting potential determination method

As shown in Figure. II.12, the pitting potential (E_{pit}) or breakdown potentials were measured from the polarization curve to assess the relative performance of the various steels investigated in the present study. The pitting potential was measured when the abrupt increase in the current density was noticed during the polarization scan and was recorded digitally using VOLTALAB software. All the values were recorded against saturated calomel electrode (SCE) unless stated.



RESULTS AND DISCUSSIONS

1. Introduction

Chapter III is devoted to the presentation and the interpretation of the experimental results obtained during the current research work. The presented discussions covers both the scientific and industrial aspects.

The obtained results are examined from a metallurgical and physical point of views in order to ensure a better understanding of the mechanical and corrosion behavior at the microscopic scale. Where possible, our results are compared to the previous works available in the open source literature with a critical review. The observed morphologies of the investigated samples at the different metallurgical conditions have been analyzed and interpreted basing on the best published scientific data presented on **Annex A**.

The resulting conclusions can then be extended and transposed to the scale of the structure and contribute to enhance the current understanding of mechanical and corrosion behavior of DSS in oil and gas filed industry.

2. Characterization of the investigated material at the as received condition

2.1 Metallographic examination

The microstructure of the studied material in the as received condition is shown in Figure III.1. It contains solely austenite and ferrite. The white -etched grains in the micrograph are austenite and the gray etched matrix is ferrite. The average grain sizes are 35 μm and 50 μm for austenite and ferrite, respectively.

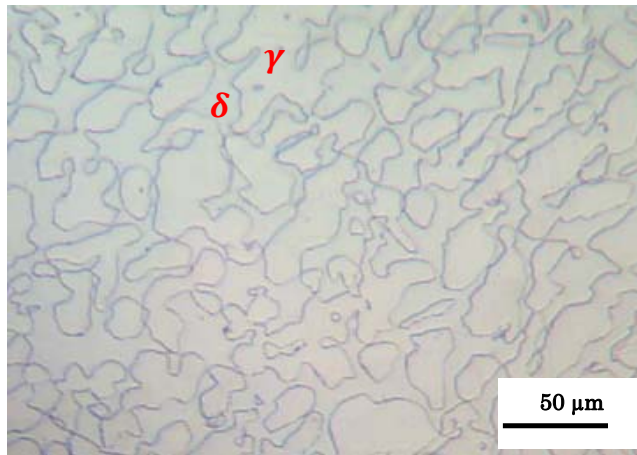


Figure III. 1: Micrograph of the investigated metal at the as received state.

On the other hand, the previous micrograph does not show the presence of any secondary phase or precipitate, this finding has been confirmed by other complementary analysis as presented in next sections.

2.2 Estimation of phase fraction

Phase volume fractions for austenite and ferrite have been determined using image analysis technique. Therefore, austenite content was estimated to be 52% and ferrite content is 48%.

2.3 XRD analysis of solution treated DSS sample

The presence of these phases was confirmed by X-ray diffraction analysis as shown in Figure III.2, no other phases or precipitates have been detected in the investigated DSS at the as received state. Table III.1 shows the summary of detected peaks following XRD analysis.

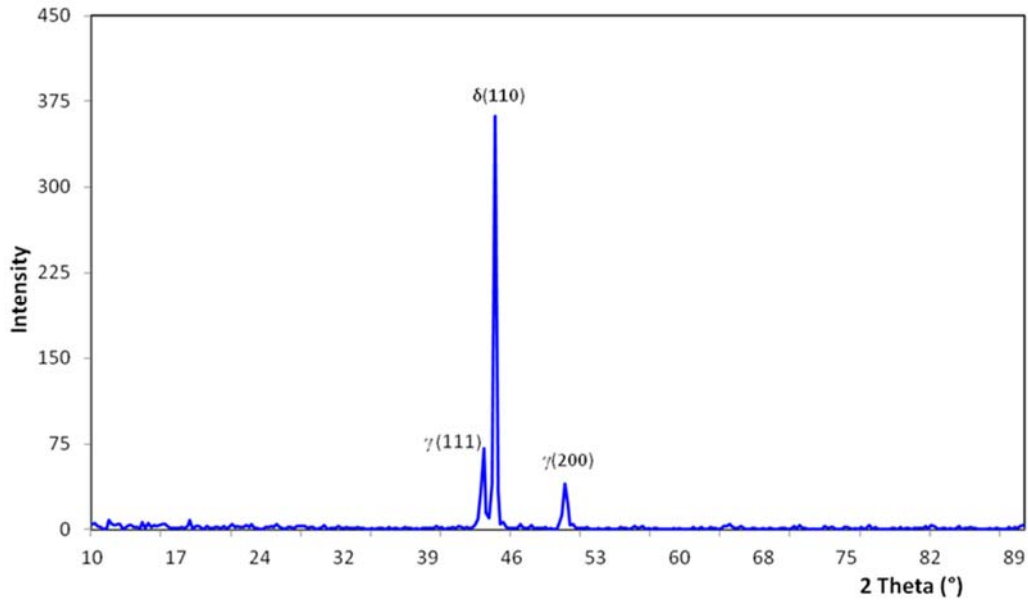


Figure III. 2: X-Ray diffraction pattern of the studied material in the as received condition.

Table III.1 : summary of detected peaks in solution treated DSS sample.

Phase	<i>hkl</i>	2θ (deg.)	<i>d</i> (Å)
Austenite (FCC)	111	11.98	1.980
	200	13.84	1.715
Ferrite (BCC)	110	11.64	2.037

The absence of precipitates in the matrix could be explained by the fact that the investigated material was successfully solution treated as required by the manufacturing standard governing the DSS used in this study (ASTM A789 and API 938-C).

Furthermore, the determined phase fraction falls within the optimum phase balance of modern DSS products which varies between 45% and 60% austenite [GUN 03].

3. Aging treatments at 850°C and Sigma (σ) phase characterization

The primary objective of carrying out aging treatments at 850°C is to produce varied levels of sigma phase in order to study their effects on the mechanical and corrosion proprieties. To

achieve this target, the following investigations handled under this section was introduced for a better understanding of the mechanisms and kinetics of sigma formation process. Obviously, the resulted effects are expected to be strongly influenced by these aspects.

3.1 Sigma phase formation process

Figure III. 3 shows the microstructure of the aged specimen at 850°C for 5 minutes holding time.

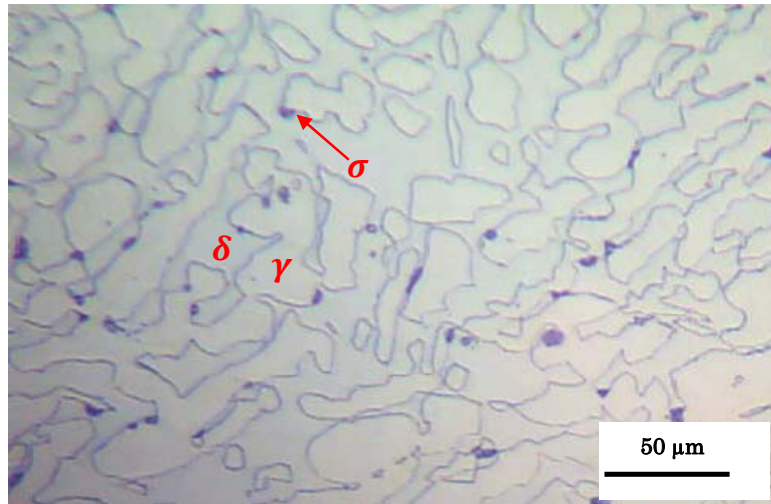


Figure III.3: Optical microstructure corresponding to the aged specimen at 850°C for 5 min.

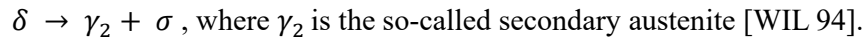
It is well noted that the precipitation of (σ) sigma phase has been taken place in this treated specimen. Sigma (σ) phase appears in dark color at the δ/γ boundaries.

It should be noted that χ phase precipitates are also present in the matrix of this aged specimen. However, the volume fraction of χ was small in comparison with σ phase and it had a far less influence on DSS than σ phase did [DEN 09].

According to Weng et al. [WEN 03], the evidence from transmission electron microscopy also suggests that χ phase is much more unstable than σ phase and would eventually transform to σ phase. These findings and assumptions are also applicable for the other aged specimens in this work; therefore χ phase precipitation was not taken in charge in the present study.

In fact, when the studied duplex stainless steel specimens were exposed to heat treatment at 850°C, the original austenite / ferrite balance was disturbed, causing the material to search for

a more stable thermodynamic state through the precipitation of sigma phase. The precipitation of sigma phase proceeds according to the following eutectoid mechanism:



According to Figure III.3, sigma (σ) phase nucleates preferentially at the δ/γ interfaces and grows through the adjacent ferrite grain; this feature is more visible on the aged specimens for longer periods as presented in next sections, which deals with sigma phase morphology using SEM observations.

This is a typical feature for sigma phase precipitation in DSS, and it is due to the high interface energy of the δ/γ interphase boundary, and as many defects concentrate there, it is a beneficial site for the heterogeneous nucleation of the σ phase [VIL 06, MIC 06, MAG 09]. When the σ phase nucleates at the δ/γ interphase boundary, some defects disappear, which releases the free energy of the materials [CHI 12]. The noticeable fastest and the high susceptibility of sigma precipitation at 850°C in the investigated material reported in this study is in good agreement with previous ones, especially the research work conducted by Palmer et al [PAL 05] using a synchrotron based in situ X-ray diffraction technique. It was pointed out that sigma σ phase was first observed approximately 40 seconds after the start of the aging treatment at 850°C. The high susceptibility of the duplex stainless steels to the sigma phase formation is frequently attributed to the ferrite composition, richer in the sigma forming elements (Cr, Mo and Si) and poorer in the elements that are less soluble in sigma (C, N and Ni) than in austenite [VIL 06].

3.2 SEM observations of Sigma phase

The figures III.4 and III.5 show secondary electron (SE) images of scanning electron micrograph obtained from the specimen aged at 850°C.

Sigma σ phase precipitates is distributed in the original ferrite matrix. The formation of σ phase is intimately associated with the δ/γ interface of duplex structure. The region of δ ferrite with a lower level indicates that the δ ferrite is more sensitive to the electrolytical etching than the γ grain [CHE 01]. Similar morphologies have been observed by other research groups as provided on **Annex A**.

As we know that the differential distribution of the alloying elements in the ferritic and austenitic phase involving a richness of Cr and Mo in ferrite leads to the preferential precipitation of σ -phase from ferrite. Meanwhile, the higher diffusion rate of alloying elements in the ferritic phase, about 100 times faster than in austenite, is also in favor of σ -phase growing into the ferrite. Owing to the depletion in Cr and Mo and enrichment in Ni of the ferrite close to σ -phase region accompanying with σ -phase precipitation, this ferrite becomes unstable and transforms into a new austenite (γ_2) [ZOU 11], which can be clearly observed under SEM (Figures III.4 and III.5).

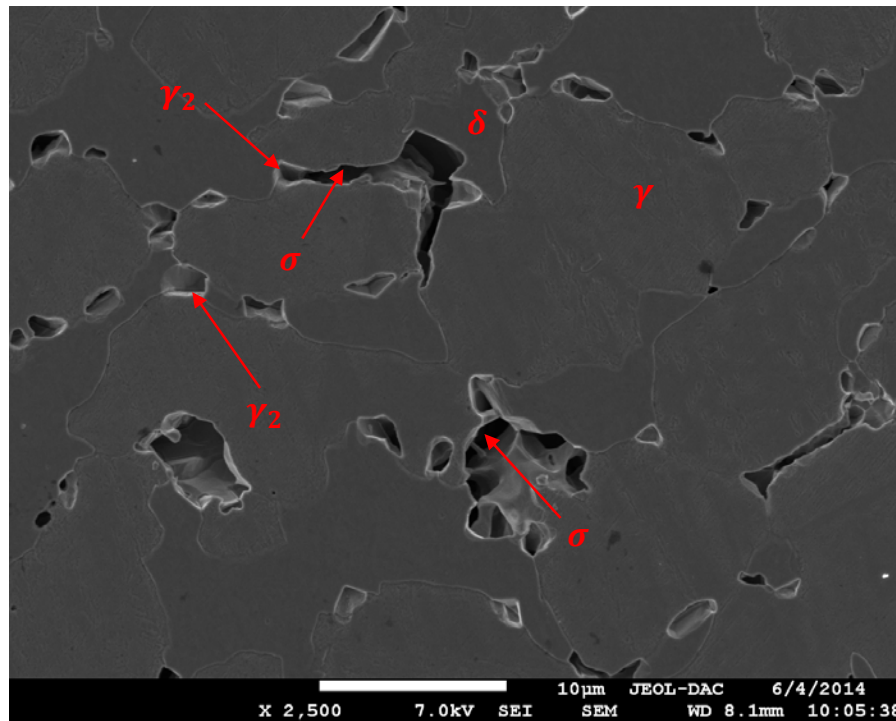


Figure III.4: SEM micrograph corresponding to the aged specimen at 850 °C for 360 min.

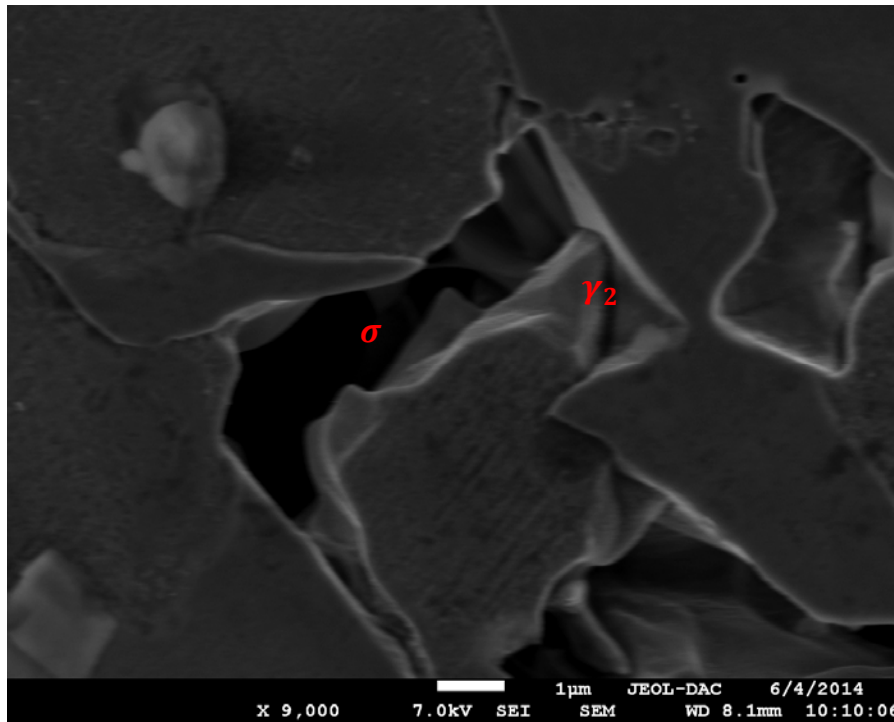


Figure III.5: SEM micrograph corresponding to the aged specimen at 850 °C for 360 min, Morphology of secondary austenite (γ_2) and sigma phase.

3.3 Effect of holding time on sigma (σ) evolution

3.3.1 Metallography of aged samples

Figure III.6 presents the microstructures of the aged specimens at 850°C for different holding periods. Sigma phase appears in dark color. It can be clearly seen that increasing the holding time at 850°C has the effect to increase the amount of σ phase. It leads also to the coarsening increase of the σ phase in an irregular shape.

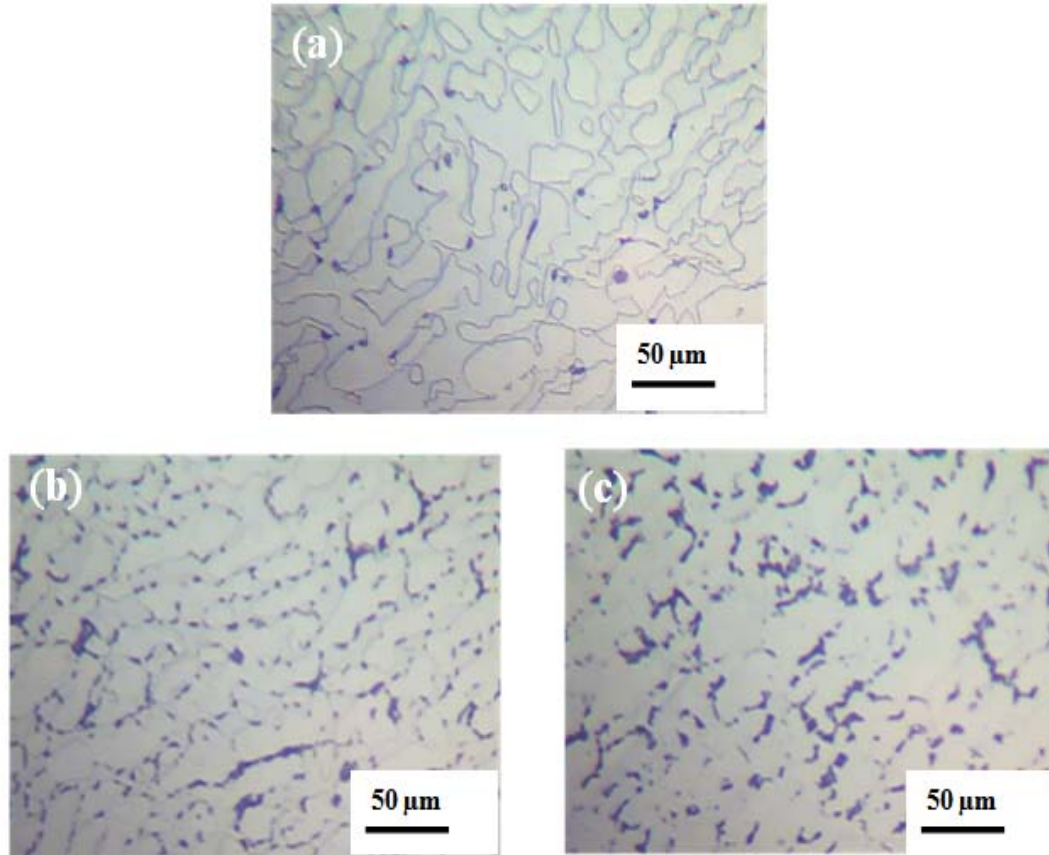


Figure III. 6: Optical micrographs showing the aged specimens at 850°C for (a) 5 min, (b) 60min and (c) 360min.

3.3.2 Quantitative analysis of sigma phase

The estimated volume fraction of sigma phase by image analysis techniques in function of holding time was plotted in Figure III.7.

As it can be seen from Figure III.7, the volume fraction of sigma phase start from ~1% for a holding time of 5 min to reach ~11% after 360 min holding time.

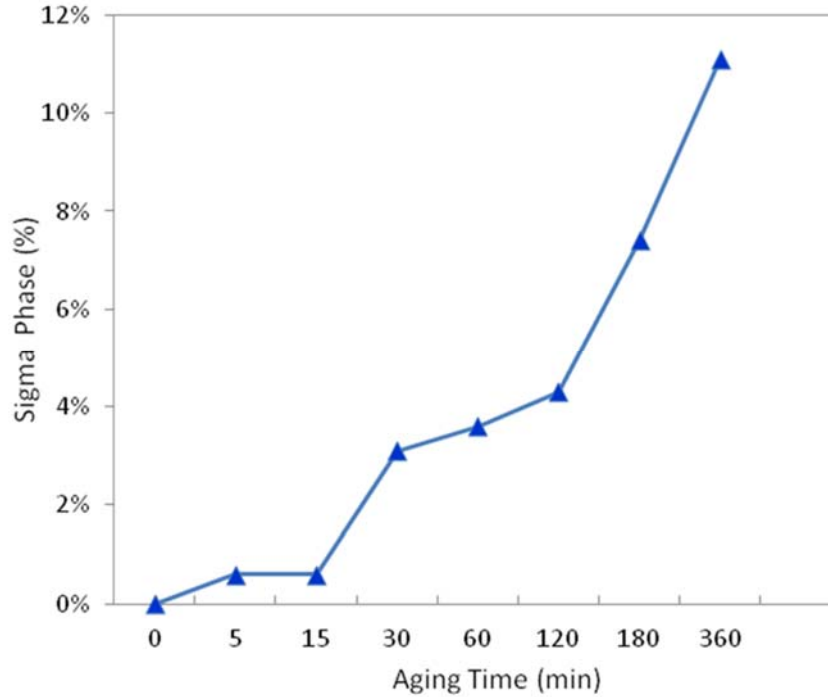


Figure III. 7: Variation of the volume fraction of sigma phase in UNS S31803 as a function of aging time at 850 °C.

3.3.3 Application of the classical Johnson-Mehl-Avrami (JMA) Analysis for sigma phase

Theoretical analysis of sigma phase formation was carried out employing the classical form of Johnson-Mehl-Avrami (JMA) equation. For this analysis the results obtained from optical microscopy (OM) were used.

As already outlined, the kinetics of sigma phase formation can be described by the following equations:

$$y = \frac{V}{V_{eq}} = 1 - \exp[-kt^n] \quad (III. 1)$$

Where, V is the fraction transformed at time t , y is the fraction of sigma phase formed ($0 < y < 1$), V_{eq} is the equilibrium amount of transformed phase at temperature T , k is an overall rate constant related to the activation energy to sigma phase formation and n is the Avrami exponent [MAG 09, FER 17].

The Equation (III.1) was re-arranged, leading to Equation (III.2) :

$$\ln \left[\ln \left(\frac{1}{1-y} \right) \right] = \ln(K) + n \cdot \ln(t) \quad (III. 2)$$

The plot of $\ln \left[\ln \left(\frac{1}{1-y} \right) \right]$ as a function of $\ln(t)$ gives a straight line (Avrami plot) shown on Figure III.8; so the n exponent and k factor of JMA equation y can be determined.

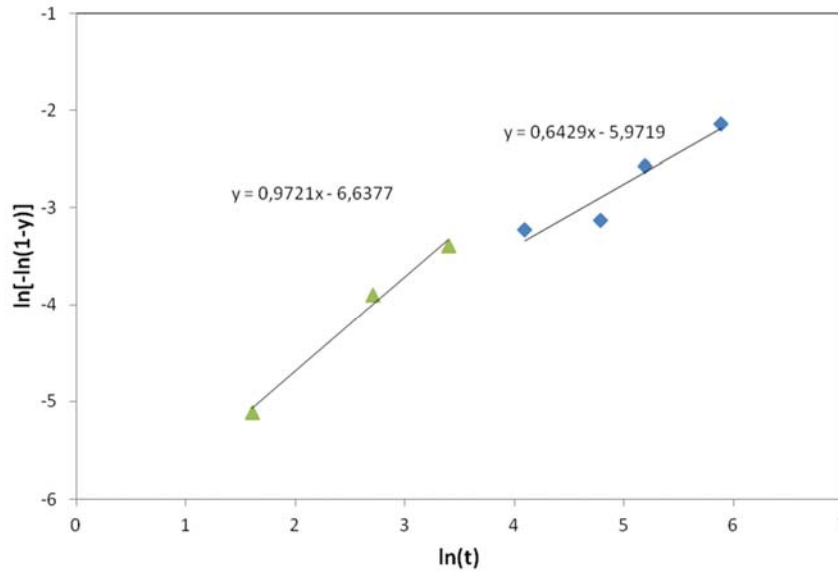


Figure III. 8: Application of the classical JMA model for sigma phase formation mechanism in at 850 °C.

From the plot presented in Figure III.8 it can be observed that the experimental data leads to two different slopes. This trend suggests that there is a change on the main mechanism of sigma phase formation with increasing of aging time, and, consequently, with the increase of sigma volume fraction, as previously mentioned by other authors [ELM 07, MAG 09, SAN 13].

The parameters k and n obtained from JMA plots are presented in Table III.2. Even though the determination of JMA parameters cannot specify precisely the mechanisms of sigma formation, it can indicate what kind of nucleation or growth conditions are occurring.

Table III.2: Values of n and k Parameter from J-M-A Calculations.

Parameter	First Slope	Second Slope
n	0.97	0.643
k	0.0013	0.0025

According to Christian [CHR 75], the n exponent of JMA equation may be related to the nucleation on grain boundaries (1.0), or nucleation in triple points (2.0) if the process is related to discontinuous precipitation; and the growth from small dimensions with decreasing nucleation rate (1.5 to 2.5), if the process is controlled by diffusion [SAN 13].

For the current study, the first slope was close to 1.0 (0.97) which indicates that the sigma phase formation mechanism may be associated to discontinuous precipitation, considering grain boundary nucleation after saturation.

Furthermore, as indicated in this section by microstructural analysis, the sigma phase formation preferably occurs on ferrite/austenite interfaces; therefore, it seems valid to consider the occurrence of nucleation and growth after saturation. Nevertheless, the possibility of the beginning of sigma growth in the first section of aging cannot be ruled out [MAG 09].

In the second slope of the plot presented in Figure III.8, the JMA exponent value of ~ 0.65 was determined.

Considering this value close to 0.5, and according to Christian [CHR 75], this slope can be related to sigma growth by plates thickening, which is confirmed by sigma coarsening as observed in previous figures (SEM micrographs).

The stage governed by nucleation of sigma, characteristic of the first slope, is replaced by the diffusion-controlled growth-coarsening governed stage, characterized by the second slope. It can be then stated that there is a transition of the kinetic mechanism of sigma formation [SAN 16].

Table III.3 shows some of the previous works investigating the Avrami exponent (n) and its correlation with the precipitation mechanism of sigma phase in aged DSS.

Table III.3: value of Avrami exponent (n) obtained in previous works.

Steel Grade	First slope	Second slop	Reference
DSS 2205	1.57	0.67	SANTOS et al., [SAN 13]
DSS 2205	0.915 ± 0.144	-	MAGNABOSCO et al., [MAG 09]
DSS 2205	$0.9449 \sim 3.9329$	$0.2236 \sim 0.4599$	SANTOS et al., [SAN 16]
DSS 2205	7	0.75	ELMER et al., [ELM 06]

As it can be noticed from this table, the value of n obtained in this work is not consistent with some previous works. Notably, Elmer et al.[ELM 06] have found $n = 7$ for the first stages of sigma formation and $n = 0.75$ for the final stages. In addition, Magnabosco [MAG 09] in a previous work found a different kinetic behavior showing just one slope in JMA plots ($n = 0.915 \pm 0.144$). The differences found may be related to the solution-treatment conditions used in each work: a treatment of 2.5 hours at 1065°C was applied in the work of Elmer et al.[ELM 06] while a treatment of 30 minutes at 1120 °C was applied in the work of Magnabosco [MAG 09]. This assumption can be also supported by the study of Badji and his coworkers, who have indicated various kinetic slopes depending on the solution-treatment conditions [BAD 08].

In fact, different solution treatment conditions leads to different ferrite and austenite fractions and chemical compositions, and different grain sizes, generating different conditions for heterogeneous nucleation and growth of the intermetallic phases [SAN 16].

3.3.4 Comparison of experimental data and the classical JMA analysis for sigma volume fraction

The maximum value for the transformed sigma volume fraction ($y = 1$) is established in the aging time (t) correspondent to the absence of ferrite, because from this time, sigma volume fraction tends to stabilization [SAN 13]. The investigated steel in this study contains 48% of ferrite as already stated.

Therefore, to compare between the experimental data and the predicted data through the classical JMA analysis, the following equation has been adopted :

$$\%V_{\sigma} = \%V_{\sigma}^{eq} \cdot [1 - \exp(-kt^n)] \quad (III. 3)$$

In this equation, the sigma equilibrium volume fraction ($\%V_{\sigma}^{eq}$) is considered equal to 48% (initial value of ferrite content).

The comparison between the classical JMA estimated sigma content and experimental results is presented in Figure III.9. In this figure, the calculated data through JMA analysis have been established considering only the first slope. Therefore it shows a good agreement between experimental values and calculated ones for the first period of aging.

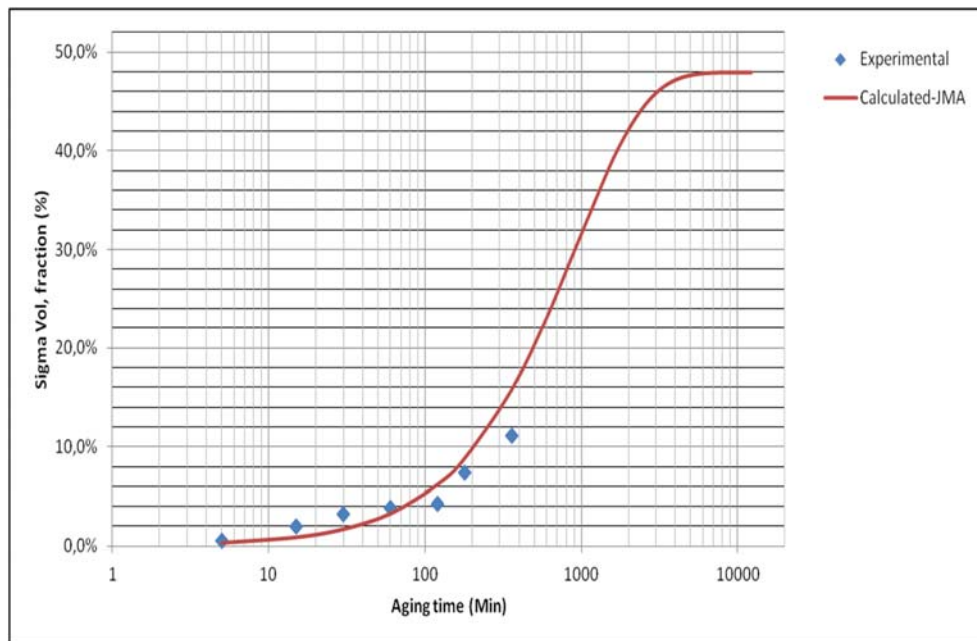


Figure III. 9: Comparison between experimental data and the classical JMA analysis of sigma volume fraction during aging at 850°C.

3.3.5 Application of the modified JMA analysis model

As pointed before in Chapter I, some authors have found a better interpolation of the experimental results is obtained by using a modified JMA model. This Model was introduced in order to take into account the complex competing effects which may occur during precipitation of σ phase [BAD 08, FER 17]. These effects are incorporated in the modified JMA model through an impingement exponent.

According to Lee et al [LEE 90], the transformation rate of a solid state transformation obeying the modified JMA type kinetic function is written in the form:

$$\frac{dy}{dt} = k(T). f(y) = k_0. \exp\left(-\frac{Q}{RT}\right). f(y) \quad (III. 4)$$

Then the Equation (III.4) can be rearranged as follows:

$$\frac{dy}{dt} = nK^n. t^{n-1}. (1 - y)^{1+c} \quad (III. 5)$$

Where:

- $y = \frac{V}{V_{max}}$ is the fraction of initial phase transformed at time t normalized by the maximum amount of phase formed at the end of transformation (V_{max}),
- c is the so-called impingement exponent.

Integration of this equation gives:

$$y = 1 - \left[\frac{1}{1+c.(K.t)^n} \right]^{\frac{1}{c}}, \text{ with } c \neq 0 \quad (III. 6)$$

The above equation can be rearranged as follows [BAD 08, FER 12] :

$$(K.t)^n = \frac{(1-y)^{-c}-1}{c}$$

and then:

$$n. \ln(K) + n. \ln(t) = \ln \left[\frac{(1-y)^{-c}-1}{c} \right] \quad (III. 7)$$

There are now 3 fitting parameters, n , K and c . When a suitable value of c is adopted, a plot of $\ln \left[\frac{(1-y)^{-c}-1}{c} \right]$ vs. $\ln(t)$ can result in a straight line. Then, the value of n and K can be obtained from the slope and the intercept [BAD 08].

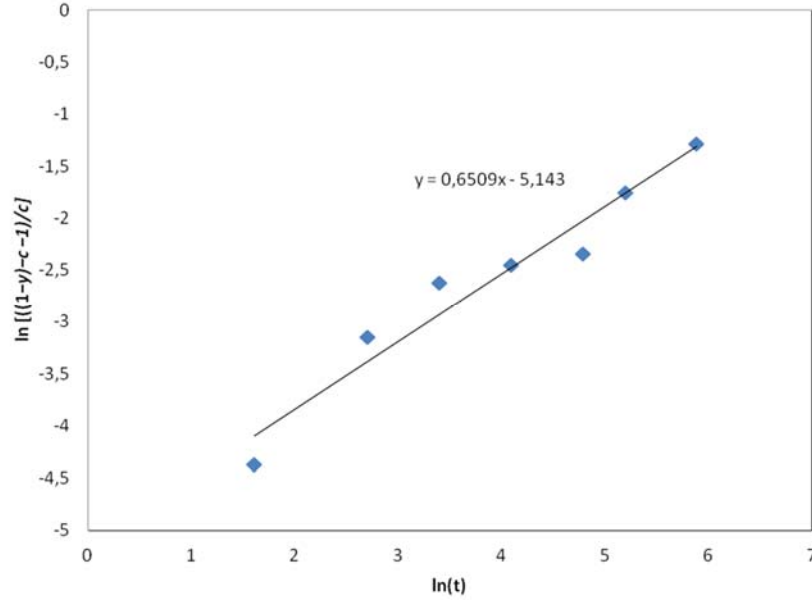


Figure III. 10: Application of the modified JMA model to the sigma phase precipitation during aging at 850 °C.

The figure III.10, shows the plot of $\text{Ln} \left[\frac{(1-y)^{-c}-1}{c} \right]$ vs. $\text{Ln}(t)$. Accordingly, the fittings parameters of the modified JMA model have been determined and reported on Table III.4.

Table III.4 : Kinetic parameters of the modified JMA model.

Parameter	n	k	c
Value	0.6509	0.00037	0.4

The best correlation between the experimental and calculated sigma-phase evolution is obtained for an impingement factor $c = 0.4$.

The comparison between the experimental results and the estimated sigma content (%) via the modified JMA model is presented in Figure III.11. It can be noticed that this model shows a good agreement between experimental values and calculated ones, with only one kinetic slope ($n = 0.6509$), indicating that this model is probably more advantageous for sigma phase kinetic prediction in aged DSS grades, because it incorporates more free fitting parameters.

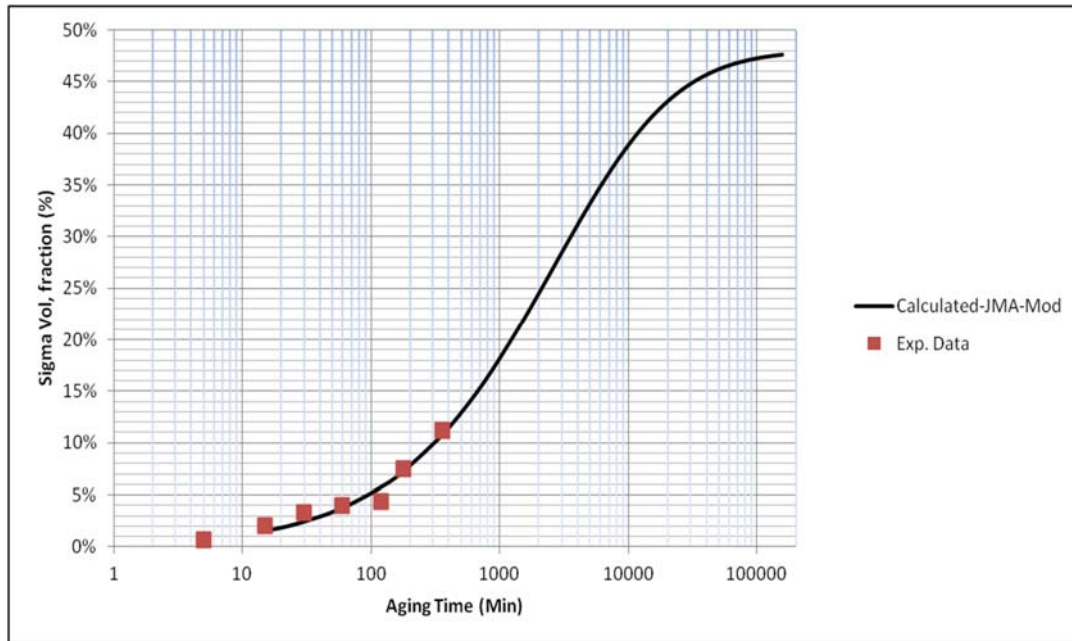


Figure III. 11: Comparison between experimental data and the modified JMA analysis of sigma volume fraction during aging at 850°C.

Up to date, the published works studying the kinetic of sigma phase through the modified JMA model involving the impingement factor (fitting parameter c) are still limited (Table III.5).

Therefore the amount of available information do not allow to provide a satisfactory explanation or to make a firm conclusion on that parameter. Hence more scientific efforts are needed for a better understanding of the physical mechanisms behind this impingement factor and its typical values.

Table III.5: Previous works using the modified JMA model for sigma precipitation kinetic.

Investigated steel grade	Impingement Factor (c)	Reference
DSS 2205	0.4	BADJI et al. [BAD 08]
Super DSS UNS S32760	1.9	FERRO et al. [FER 12]

3.3.6 XRD analysis of aged samples

X-Ray diffraction patterns of aged samples is shown in figure III.12.

The observed peaks have been analyzed and indexed as summarized in the table III.6.

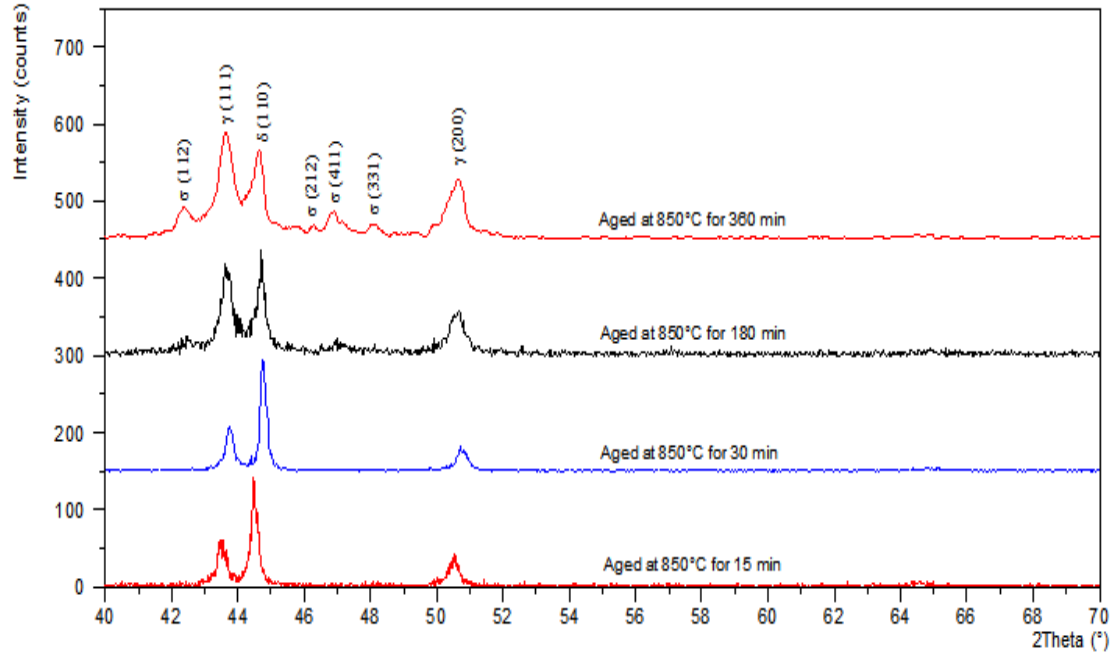


Figure III. 12: X-Ray diffraction patterns of samples aged at 850°C.

Table III.6: Summary of calculated diffraction peaks.

Phase	<i>hkl</i>	2θ (deg.)	<i>d</i> (Å)
Austenite (FCC)	111	11.98	1.980
	200	13.84	1.715
Ferrite (BCC)	110	11.64	2.037
Sigma (tetragonal)	212	11.91	1.992
	411	12.16	1.952
	331	12.45	1.906

X-Ray Diffraction analysis has also confirmed the effect of holding time on the volume fraction of precipitated sigma phase.

As previously stated, the X-ray diffraction pattern of the solution treated specimen shows ferrite and austenite phase peaks only and does not show any peak corresponding to other phases, however small peaks corresponding to sigma phase have been observed on the aged specimens at 850°C, these peaks are more detectable in the aged sample for 360 min holding time as reported in Figure III.12.

With increasing holding time, the intensity of sigma peaks increases and the peak intensity of the ferrite phase compared to the austenite phase decreases, this is directly linked with the decomposition process of ferrite into sigma phase and secondary austenite.

Furthermore, the XRD pattern did not show the σ phase signals in the specimens aged for 30 and 15 min, although there was evidence of its occurrence. This could be explained by the low fraction of the σ phase [DEN 09]. Consequently, it can be concluded that all the obtained diffraction peaks are in good agreement with the changes in σ phase ratio during the isothermal treatments.

4. DSC analysis Results

4.1 Study of "475 °C Embrittlement" by DSC analysis

The apparatus used for DSC analysis is limited to 600°C; therefore we were only able to detect the occurrence of the precipitate that take place below this temperature.

The DSC analysis have carried out on the solution heat treated samples.

Figure III. 13 shows the Differential Scanning Calorimetry (DSC) curve obtained following a heating measurement from 50 to 600 °C with 30°C/ min heating rate. The measured DSC heating curve goes very well with the reported measurements performed on previous works for a similar duplex stainless steel grade [LIP 16, STE12].

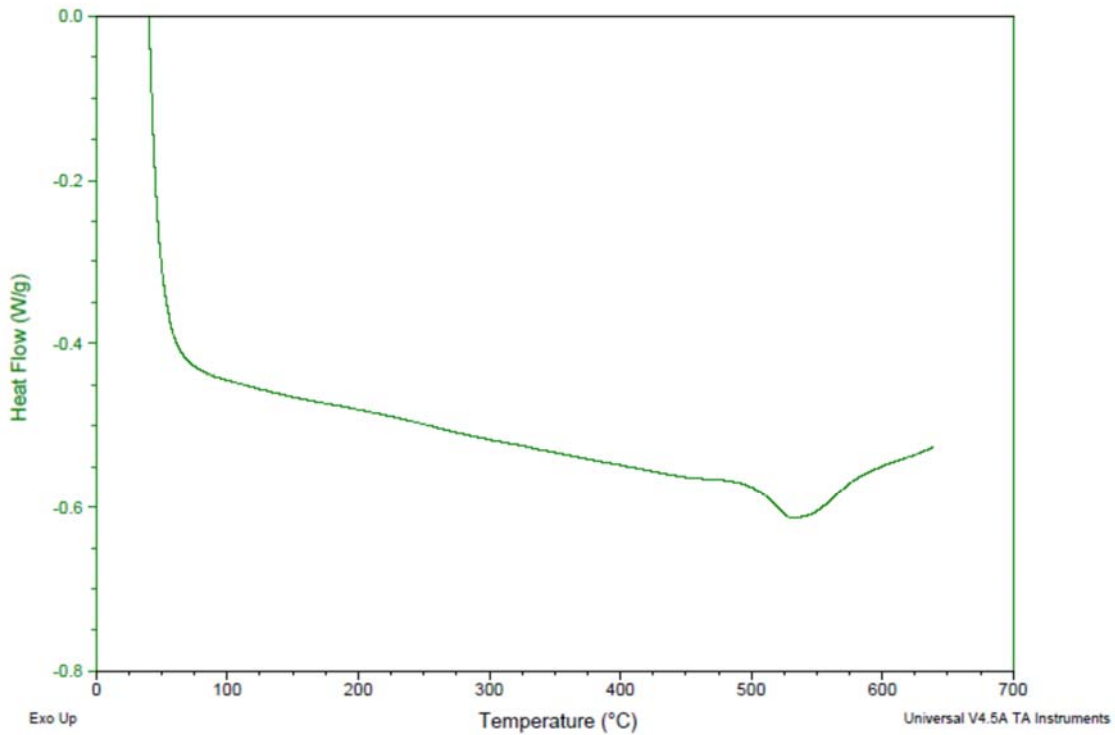


Figure III.13: DSC curve of heating measurement duplex stainless steel. Heating rate 30°C/min.

The curve is characterized by the presence of a negative (endothermic) peak in the temperature range 465°C and 560°C. According to technical literature, this endothermic peak involving a T_{onset} at about 465°C, T_{end} at about 560°C and T_{peak} about 525°C represents the dissolving of α' -chromium-rich phase.

In fact, according to Chung [CHU 92] and Hery [HER 06] the only transformation that occurs during heating from 200°C to 550°C is the redissolution of the iron and chromium atoms. During a temperature rise ramp, the target temperature is higher than the solvus of the miscibility gap (Figure III.14), the chromium and iron atoms are redissolved to reform a homogeneous matrix.

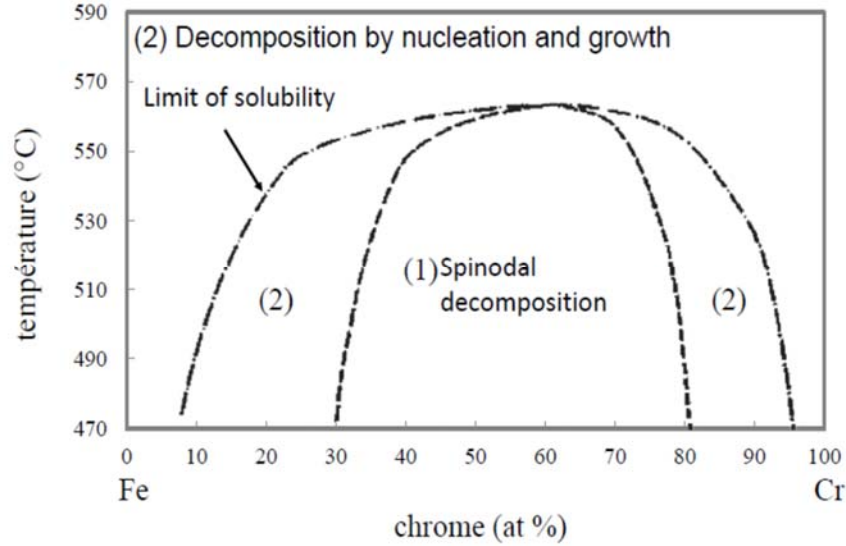


Figure III.14: Fe–Cr binary phase diagram [MAE 14].

According to Courtier [COU 14], the DSC technique provides an "Indirect" measurement of the unmixing process. The integral of the heat flow peak associated with this reaction is a thermodynamic characteristic that informs about the "stability" of the composition fluctuations. It is therefore rather close to the amplitude corresponding to the spinodal decomposition. Based on this argument, Courtier [COU 14] established an empirical law which correlates the evolution of the redissolution Enthalpy with the aging time at a given aging temperature:

$$H(t, T) = H_0 + \left(k_{H0} \cdot \exp\left(-\frac{Q_H}{R.T}\right) \cdot t \right)^{a_H} \quad (III. 8)$$

Where, Q_H is the activation energy of the embrittlement process.

Following the same reasoning, the apparent activation energy related to the redissolution process has been determined in Section 4.2, and has been assumed to be as same as the activation energy corresponding to the spinodal decomposition of ferrite phase.

4.2 Activation Energy calculation

Figure III. 15 shows Differential scanning calorimetry curves of heating measurement from 50 to 600 °C obtained with different heating rate 30, 40 and 60°C/ min.

The shape of the obtained curves is in good agreement with theory. In fact, faster scan rates result in increased values of heat flow giving increased accuracy of measurement, and this also minimizes the time of the run and potential drift of the analyzer. It has been reported that fast scan rates used by fast scan DSC can give extremely accurate data. This feature is well indicated on the following fundamental equation of DSC [GAB 07]:

$$DSC\ signal(W/g) = Heat\ capacity\ (J/kg) \cdot scanning\ rate(^{\circ}K/s) \quad (III. 9)$$

As known in literature [SMI 98, RIV 18], the Kissinger method can be used for deriving activation energies from temperature scanned experiments. It is based on the fact that the observed temperature of a peak (T_p) depends on the scan rate ($S = dT/dt$) of the experiments. The method has been generalized and justified for solid-state reactions by Mittemeijer et al.

The Kissinger expression, as modified by Mittemeijer et al., relates T_p to S as follows [MIT 88, RIV 18]:

$$\ln\left(\frac{T_p^2}{S}\right) = \frac{Q}{R \cdot T_p} + \ln\left(\frac{Q}{R \cdot k_0}\right) \quad (III.10)$$

where T_p = peak temperature (°K); S = heating rate (°K/s); Q = effective activation energy for the process associated with the peak (J/mol); R = gas constant (8.314 J/mol/ K); k_0 = pre-exponential factor in the Arrhenius equation for the rate constant k :

$$K = k_0 \cdot \exp\left[-\frac{Q}{R \cdot T}\right] \quad (III. 11)$$

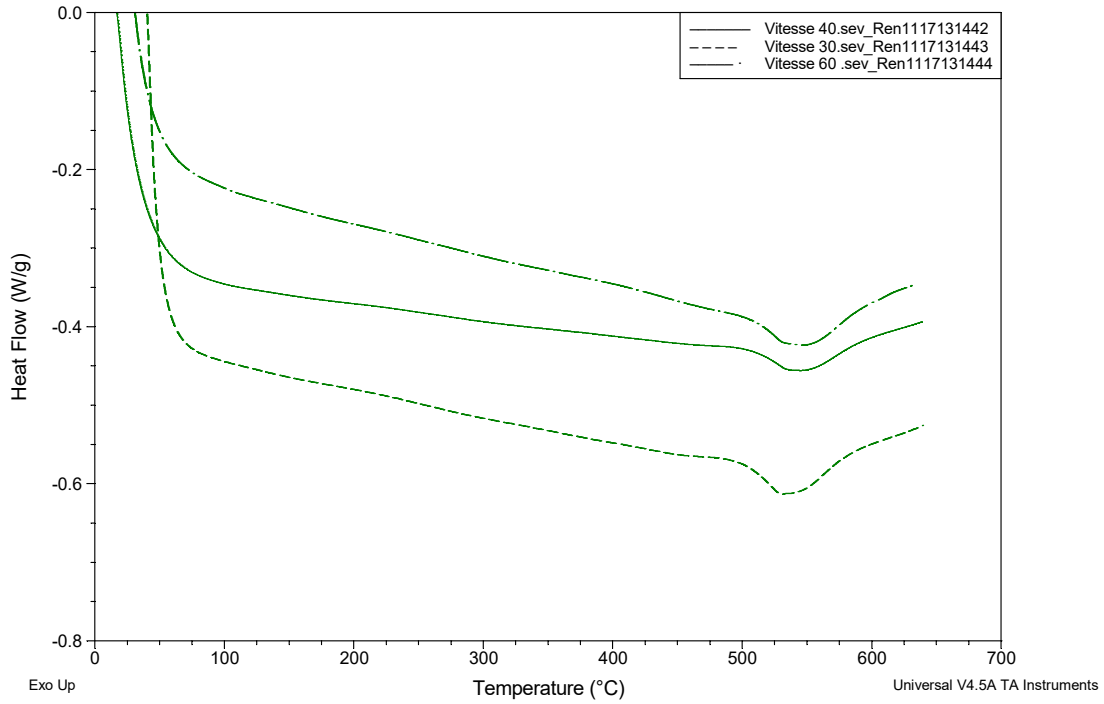


Figure III.15: DSC curves of heating measurement duplex stainless steel. Heating rate 30, 40 and 60°C/min.

The activation energy governing the transformation can be determined from the slope of the straight line obtained by plotting $\ln(T_p^2/S)$ vs. $1/T_p$, as shown in figure III.16.

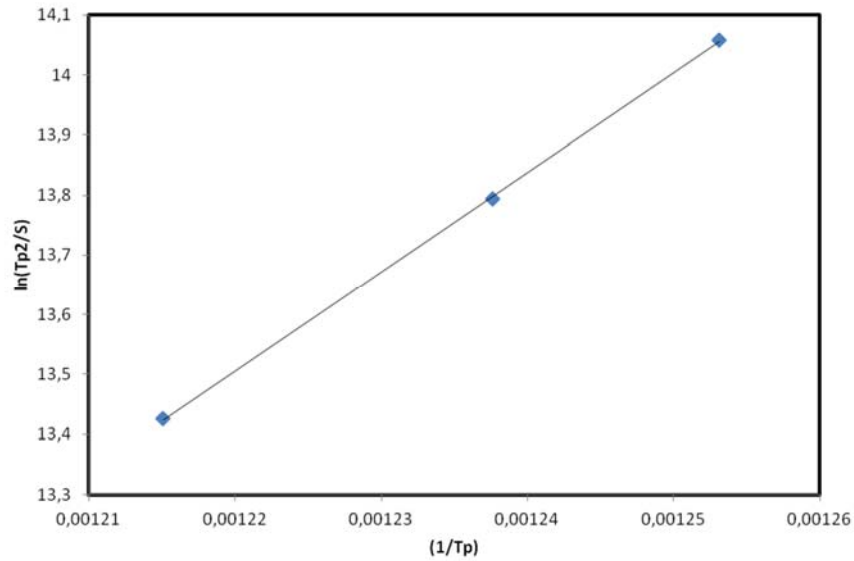


Figure III.16: Plot of $\ln(T_p^2/S)$ as function of $1/T_p$.

Following Kissinger method, the rate constant (k_0) has been also determined. the obtained results are summarized in table III.7 below:

Table III.7 : Activation energies and k_0 values characterizing the phase transformation processes of the DSS grade in the temperature range 300 and 525°C.

Peak Tempertaure	T_p (°C)	525	535	550
	T_p (K)	798	808	823
Heating rate	S (°C/min)	30	40	60
	S (°C/S)	0,5	0,67	1
Activation Energy	Q(kJ /mol)	138		
Rate constant	k₀	13,60 x10 ⁶		

It should be noted that the determined activation energy in the current investigation is not close to the typical value of 250kJ/mole corresponding to the activation energy of chromium diffusion in α -iron ($\sim 230\text{kJ/mole}$), as indicated by Brown et al. [BRO 91] and Leax et al. [LEA 92].

However, the value of $Q = 138\text{ kJ/mole}$ we obtained is in a good agreement with other previous works that we summarized in Table III.8. In particular, a value of $Q = 147\text{ kJ/mole}$ was indicated by Trucker et al. for an aged DSS grade very similar to the one investigated in

this work, through a series of isothermal aging between 260°C and 538°C for times ranged from 1 and 10,000 hour. It is also very close to the activation energy found by Couturier using DSC measurements in a precipitation hardenable stainless steel grade (15-5PH SS) [COU 14].

Table III.8 : Activation Energy of separation process as measured during previous works.

Studied alloy	Investigated parameters	Activation Energy	Reference
Fe-26%Cr-X%Ni	Vickers Hardness	225-304kJ/mol	(BROWN <i>et al.</i> , 1991), [BRO 91]
Ferrite of DSS	Amplitude	260kJ/mol	(LEAX <i>et al.</i> , 1992), [LEA 92]
PH 13-8 Mo SS	Rockwell Hardness	139 kJ/mole	(ROBINO <i>et al.</i> , 1994), [ROB 94]
2205 DSS	Vickers Hardness	147 kJ/mole	(TUCKER <i>et al.</i> , 2015), [TUC 15]
15-5PH SS	Redissolution Enthalpy- by DSC	155 kJ/mole	(COUTURIER, 2014), [COU 14]
15-5PH SS	Vickers Hardness	106kJ/mole	(COUTURIER, 2014), [COU 14]

The fact that the determined activation energy is well below the expected typical value ($\sim 250\text{kJ/mole}$), implies that embrittlement process is not only governed by the diffusion of chromium, but also the driving force of the unmixing process. Meyer *et al* [MEY 11] showed that the activation energy is influenced by chemical composition of the aged steel as per the following empirical law:

$$Q = -64 - 2\%Cr - 49\%Si - 5\%Mo - 11\%Cu + 33\%Ni + 64\%Mn + 4123\%N$$

Chung pointed out that the activation energy of aging embrittlement is also strongly influenced by the fabrication process and thermomechanical history [CHU 90].

According to our literature survey, it appears that there is no consensus among investigators on the understanding of the activation energy of aging. While there remains some uncertainty regarding the correct value, it is important to use a conservative estimate of the activation energy when determining an accelerated aging treatment to simulate end of life conditions [PUM 90].

As already outlined in the literature review chapter, the activation energy is characteristic of the embrittlement process. It is an important parameter to assess and predict the thermal

stability of DSS when subjected to thermal aging at intermediate temperatures, as we will demonstrate on Section.4.3.

4.3 Kinetic of embrittlement and End of life prediction

The main objective of studying the kinetic of embrittlement of DSS is to predict the end of life of DSS components when operated at high temperature, particularly for some critical engineering components in nuclear power plants and hydrocarbon units. It aims to follow and anticipate the evolution of mechanical properties of DSS components and to correlate these properties to the decomposition of the ferrite.

In practice, realistic aging of the components for end of life or life extension conditions at the actual service temperature (280-330°C) cannot be produced, therefore it is usual to simulate the metallurgical structure by accelerated aging at higher temperature (~400°C) [CHU 90].

One of the major issues in studying the embrittlement mechanisms is attributed to the difficulty of characterizing the microstructural evolution of the aged materials in which several different phases appear to precipitate simultaneously on a very fine scale (nanometric scale). Earlier investigations using transmission electron microscopy (TEM) failed to identify the α' precipitation at the lower aging temperature [CHU 90]. According to many sources it is reported that the field ion atom probe technique (FIAP) appears to be the best suitable technique for microstructural characterization of spinodal decomposition [MIL 95, DAN 00, SAH 09, MEY 11, COU 14].

However, several authors succeed to follow the embrittlement kinetics through indirect observations such as changes in certain mechanical properties like hardness [MIL 96], impact energy [SAH 09] or saturation of certain microscopic features [WEN 04]. Additional information on the previous works has been reported on Table III.5.

Knowing that the change in microhardness is correlated to the embrittlement of the alloy due to α - α' phase separation, several authors have used KJMA model to predict the embrittlement of aged DSS.

This model describes the microhardness as a function of isothermal aging time and temperature, allowing for long time extrapolations at temperature to simulate component lifetimes.

The KJMA expression is used to describe a variety of phase transformations and related phenomena, and has the following general form:

$$S(t, T) = 1 - \exp(-(K(T)t)^n) \quad (III. 12)$$

where $S(t, T)$ is a progress variable in terms of aging time t and temperature T , which varies continuously from 0 to 1 as the transformation proceeds from start to completion [TUC 15].

The time exponent n is known as the Avrami exponent, and typically relates to the nucleation and growth mechanism and the geometry of the newly growing phase. This parameter often assumes an integer value, though this is not always the case [SUN 95]. The term $k(T)$ is a kinetic coefficient, which is typically described by an Arrhenius form:

$$k(T) = k_0 \exp(-Q/RT) \quad (III. 13)$$

In the above equation k_0 is the pre-exponential factor, Q is the effective activation energy for the phase transformation, and R is the universal gas constant (8.314 J/mol/K).

The KJMA model is scaled by the maximum change in microhardness in order to relate the measured value to the phase transformation. This model assumes that the change in hardness is linearly related to the phase fraction transformed. The microhardness at any time and temperature can be described by the following Equation:

$$Hv(t, T) = Hv_{Max} - (Hv_{Max} - Hv_0) \cdot \exp(-(k(T)t)^n) \quad (III. 14)$$

The model described by the above equation contains four fitting parameters, namely the initial microhardness prior to isothermal exposure (Hv_0), the final saturation microhardness that would be obtained after infinite exposure (Hv_{max}), the power describing the time dependence of hardening (n), and the activation energy.

Also, it can be seen from this equation that at time, $t = 0$, $Hv(t, T) = Hv_0$, and in the limit as t approaches $+\infty$, $Hv(t, T)$ approaches Hv_{max} .

The Equation (III.14) can be rearranged as follows:

$$Hv(t, T) = Hv_{Max} - (Hv_{Max} - Hv_0) \cdot \exp\left(-\exp\left[n \cdot \left(\ln(k_0) - \frac{Q}{RT} + \ln(t)\right)\right]\right) \quad (III. 15)$$

Note that, in the above Equation, the activation energy (Q) is in units of J/mol , time t is in hours, and temperature T is in kelvin.

The saturation microhardness of ferrite phase (Hv_{max}) was investigated by other research groups following a series of thermal aging between $260^{\circ}C$ and $538^{\circ}C$ up to 10 000 hours and it was found equal to 477 ± 15 HV [GUO 16, TUC 15, TUC 11].

Knowing that the initial microhardness (Hv_0) of ferrite phase of our steel grade is 246 HV, and assuming that $n \approx 2/3$ according to Robino et al [ROB 94], then all the parameters of Equation (III.15) are identified, as summarized in the Table III. 9.

Table III.9: KJMA parameters for hardness prediction during embrittlement.

Parameter	Value	Notes
Hv_0 (HV)	246	-
Hv_{max} (HV)	477 ± 15	-
Q (kJ/mol)	138	<i>From DSC analysis</i>
k_0	$13,60 \times 10^6$	<i>From DSC analysis</i>
n	$\approx 2/3$	<i>ROBINO et al.</i>

The plot of $Hv(t, T)$ in function of time and temperature is given in Figure III.17.

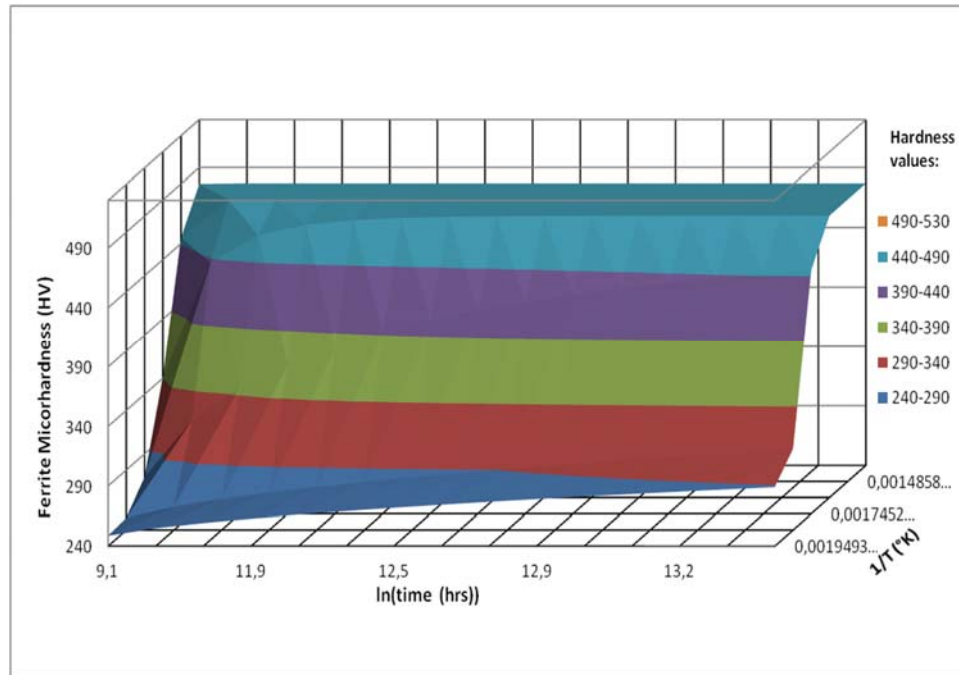


Figure III.17: Predicted Microhardness surface for aged 2205 DSS grade.

In practice, this plot can be used to make end-of-life hardness predictions for DSS components when operated at a specific aging temperature.

We have previously presented in Chapter 1 the maximum allowable service temperature specified by some industrial codes and standards for duplex stainless steels. The ASME Boiler and Pressure Vessel Code currently places an upper temperature limit of 315 °C for the use of DSS 2205 grade, while the TÜV German code considers 280°C as an upper limit of use. They do not mention the maximum service lifetime.

The Table III.10 shows the predicted hardness at 280°C and 315°C, for a periods of times ranging from 5 to 25 years. A period of 25 years is usually considered as a design life in the engineering of hydrocarbon units.

Table III.10: Hardness prediction at 280°C and 315°C during service life.

Hardness prediction (HV)		
Time (Years)	280°C	315°C
5	281	343
10	299	380
15	313	403
20	325	419
25	335	430

At 280°C for 25 years this analysis predicts that DSS 2205 would have a change in microhardness of approximately 89 HV, whereas at 315°C the DSS 2205 would have a change of approximately 184 HV indicating a significant embrittlement of the alloy via α - α' phase separation. This finding indicates that the upper operating limit fixed by the ASME Boiler and Pressure Vessel Code (315°C) may not be appropriate for components that would operate at this temperature for extended times.

In this context, Tucker and his coworkers have performed a similar analysis on the alloy 2205, and they have concluded that this alloy may be viable for use up to 230 °C in nuclear power applications for 80-year service lifetimes based on a microhardness criteria corresponding to 300HV [TUC 15].

As noted previously a higher hardness is a sign of material embrittlement leading to material failure when combined with other operating favorable factors. For that reason, it is usually to limit the hardness of DSS components to a reasonable threshold. To give an example, the API 938C (Technical Report for the Use of Duplex Stainless Steels in the Oil Refining Industry) requires that the hardness shall not be above 320 HV for weld procedure qualification to avoid premature DSS failure by the mechanism of SCC (Stress Corrosion Cracking) [API 15].

5. Corrosion Tests

This part of work is aimed to cover the resistance of aged (sigmatized) samples to pitting corrosion. As we demonstrated in Chapter I, several important field failures have been caused by this form of attack.

To achieve this objective, the pitting potential values of the investigated samples have been determined in the simulated sea water and the oily produced water solutions. In fact, there have been only a limited number of studies examining the behavior of sigma phase in DSS materials tested in a simulated oil field environment [SAI 12], indicating that there is a need to carry out further research works with oil field solutions.

Additionally, knowing that most of Oil and gas companies base their materials selection on field experience data coupled with laboratory tests, therefore the use of the oily produced water as a test solution in this study is meant to contribute to enhance the understanding of sigmatized DSS corrosion behavior in oil field environments.

5.1 Potentiodynamic polarization results of solution treated sample (in the as received condition)

5.1.1 Simulated seawater solution

Potentiodynamic polarization tests were conducted to evaluate the pitting susceptibility of DSS samples at the as received condition (solution treated). Figure III.18 presents the polarization curve conducted in 0.5 M NaCl solution.

Basing on the definition of pitting potential provided previously in chapter I, the pitting potential of the investigated sample has been determined. Therefore $E_p = 1120mV/SCE$.

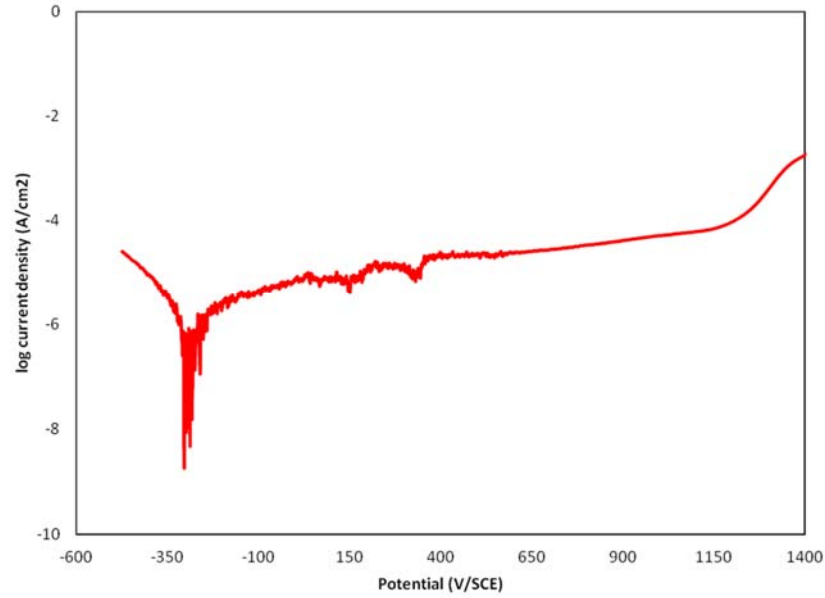


Figure III. 18: Potentiodynamic polarization curves for the solution treated sample in simulated seawater solution.

5.1.2 Produced water solution

Figure III.19 shows Potentiodynamic polarization curve for solution treated sample tested in produced water.

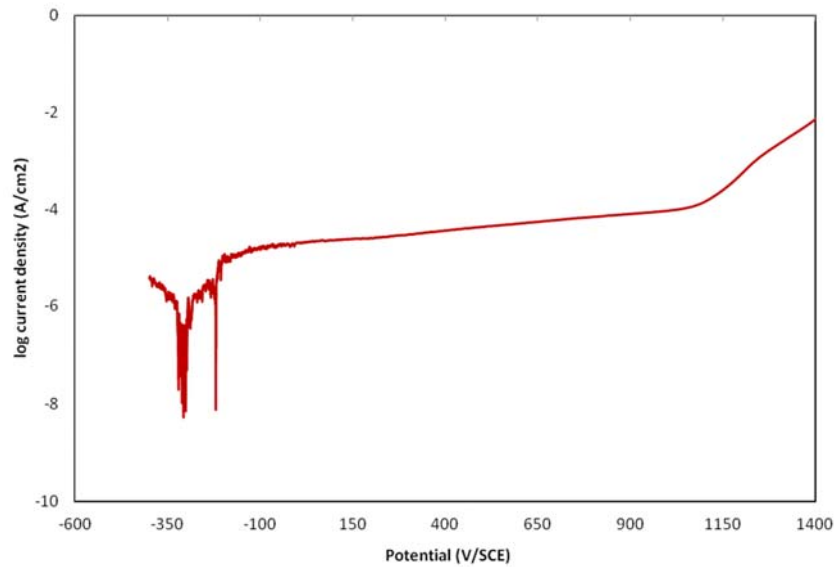


Figure III. 19: Potentiodynamic polarization curves for the solution treated sample in Produced water solution.

The pitting potential of the sample has been determined in produced water solution. Therefore $E_p=1024$ mV/SCE.

5.2 Potentiodynamic polarization results of aged sample

To investigate the effect of sigma phase on pitting potential of aged samples, the Potentiodynamic polarization curves have been established in both test solutions as presented hereafter.

5.2.1 Simulated seawater solution:

Figure III.20 presents typical polarization curves conducted in 0.5 M NaCl solution.

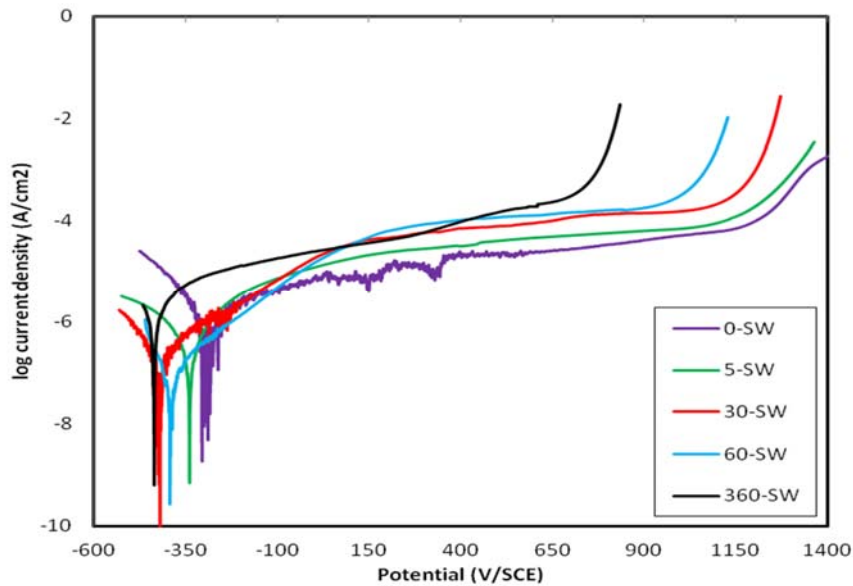


Figure III.20: Potentiodynamic polarization curves for the aged samples at 850°C in for different times in simulated seawater solution.

Basing on the analysis of the polarization curves the pitting potential E_p values of the different tested samples were determined. The obtained values are shown in the Table III.11.

Table III.11: Pitting potentials for the tested samples in Simulated seawater.

Sample identification	0-SW	5-SW	30-SW	60-SW	360-SW
Aging time (min)	0	5	30	60	360
E_p (mV/SCE)	1120	980	910	790	560

It can be seen from Table III.11 that the pitting potentials of tested samples decrease markedly with increasing of aging time from 1120 mV (SCE) of the solution treated sample to 560mV (SCE) of the aged for 360 min. It was previously established in this research work that the increase of the aging time has the effect to increase the sigma phase ratio. So it's clear that the decrease of pitting corrosion resistance in the aged DSS samples is directly attributed to the formation of sigma phase and its volume fraction. Even about 3.3 % of sigma phase corresponding to the aged sample for 30 min can affect dramatically the pitting resistance of the alloy. On the other hand, the un-aged sample show the highest pitting potential value, supporting the standard recommendation of using DSS in the solution treated condition with no sigma phase content [JOH 13].

This restriction implies a careful control of the whole manufacturing process, since a reliable and relatively cheap metallographic procedure is not simple to achieve, especially for the quantitative determination of very small (1-2%) dangerous phase contents[CAL 13].

Actually, it is well documented in the literature that the resistance of this material to localized corrosion is mainly due to the higher content of chromium and molybdenum which protect the DSS by forming and stabilizing the passive film. The decrease in pitting potential as a result of sigma phase formation has been explained by many authors, and it was related to chromium and molybdenum depletion in the zones surrounding sigma phase [EZU 06, DEN 09, MAG 05, SAN 13]. During the formation of sigma phase, Cr and Mo diffused from the ferrite phase to the growing sigma phase, thus causing localized depletion areas in Cr and Mo around the sigma phase. These areas containing lower concentration of Cr and Mo and higher amount of Ni became unstable and transformed into secondary austenite [DEN 09]. These Cr- and Mo-depleted areas surrounding sigma phase become susceptible to pitting attack and thus a reduction on pitting potential is registered.

The lower molybdenum and chromium content is not the only factor for being prone to corrosion. The neighborhood of the more noble phases will enhance the anodic dissolution of the new formed secondary austenite [POH 07].

This behavior of decrease in corrosion resistance due to the increase in aging time was also established in the tested samples in Produced Water as outlined hereafter.

5.2.2 Produced water solution

The polarization curves for the tested specimens in produced water solution are presented in Figure III.21.

Following the same methodology adopted previously for the tested specimens in simulated seawater solution, the pitting potential values have been determined and listed in the Table III.12. The presented data suggest that the pitting potential of the various tested samples show a clear dependence on the aging time. As expected, for high aging time, and consequently high sigma volume fraction, low pitting potential is registered. However, it is well noted that for same aging time a lower pitting potential is found for tested sample in produced water solution.

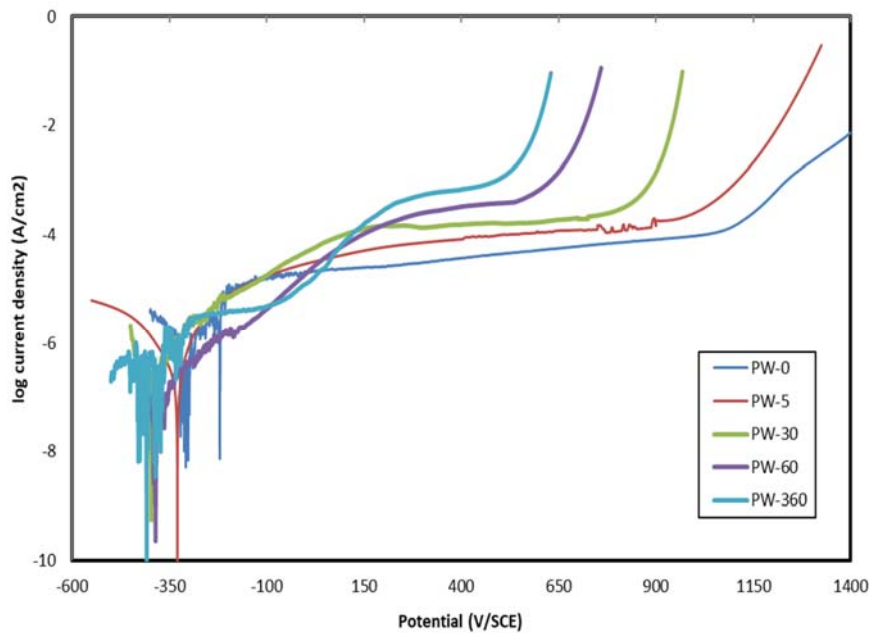


Figure III.21: Potentiodynamic polarization curves for the aged samples at 850°C in for different times in Produced Water solution.

The lower corrosion resistance of aged DSS in produced water solution can be explained by the higher chloride content in this solution.

The other chemical species of the produced water solution shown in Table II.3 do not appear to have a significant impact on the pitting corrosion behavior. In fact the chloride concentration in the simulated seawater solution (0.5M NaCl solution) is about 17725 ppm while in the produced water solution is about 28862 ppm. This confirms that the pitting potential depends on both sigma phase content and the chloride concentration. For chloride, three different models are frequently quoted to explain its effects on pitting: adsorption

leading to local film dissolution, penetration of anions in the film leading to weakening of the oxide bonds, and rupture of film at defects, such as cracks and dislocations [DON 11].

Table III.12: Pitting potentials for the tested samples in Produced Water.

Sample identification	0-PW	5-PW	30-PW	60-PW	360-PW
Aging time (min)	0	5	30	60	360
E_p (mV/SCE)	1024	950	720	570	450

On the other hand the obtained results suggest that the un-aged sample demonstrate an acceptable pitting resistance when exposed to produced water test solution, confirming the indication that this material grade when successfully heat treated is highly suitable for use for produced water process fluids, even at a high level of chloride concentration. Therefore, caution is needed by DSS manufacturers and users to ensure a high quality of DSS products during processing, machining, heat treatments and welding to avoid sigma phase formation.

To summarize the effect of sigma phase on the corrosion resistance of aged DSS, the pitting potential values obtained in both test solutions have been plotted as function of sigma content as provided in figure III.22.

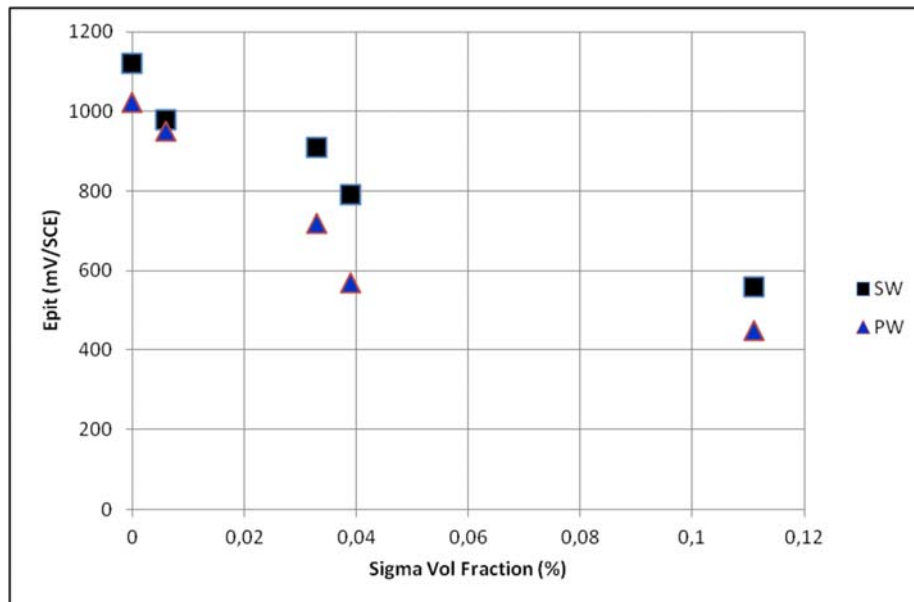


Figure III.22 : E_p as a function of sigma volume fraction (%).

5.3 Engineering significance of pitting potentials in the aged samples

In this section we will discuss the pitting potential values on the light of the concept of pitting engineering diagrams. The idea of Engineering diagrams based on pitting potential (E_p) measurements was introduced by Fielder and Johns in 1989 [FIE 89, MAM 19] and it is used to define limiting conditions for pitting corrosion. When used in combination with knowledge of the corrosion potential in a system containing various oxidizing species such diagrams can be used to assess the corrosion risk [MAM 19].

These diagrams are obtained by mapping the regions in which pitting occurs at different given critical potentials, usually ranging from 300 to 700 mV vs SCE. The critical potential used for defining the boundary is equal to the maximum corrosion potential corresponding to the maximum open circuit potential (E_{OCPmax}) in the test solution. The E_{OCPmax} is defined as the highest corrosion potential in a system containing various oxidizing species such as chlorine [RUI 89, VEN 89, BAR 93, MAM 19]. To give some examples, the E_{OCPmax} was reported to be typically in the range 190-220 mV vs SCE for a drinking water system and about 300 mV vs SCE for a water heater system [FIE 89, MIK 09]. BARDAL et al [BAR 93] indicated that, the maximum potential measured on passive stainless steel in natural seawater after long term exposure at temperature below 30-40°C is about 400 mV(SCE) and in chlorinated seawater about 500-700mV(SCE) depending on the chlorination level. Therefore, a potential of 700 mV(SCE) has been found suitable for most stainless steels for the determination of CPT (Critical Pitting Temperature) as per ASTM G150 standard testing method [AST 18].

On the other hand, it was reported that pitting is unlikely to occur if the maximum corrosion potential of the environment is lower than the pitting potential [GOO 87, RUI 89, VEN 89, LU 91, MAM 19].

Based on the above facts, the engineering pitting diagrams are used to predict the risk for pitting in a given system by comparing with the corrosion potential (E_{OCPmax}), as discussed in other works [FIE 89, CAR 94, JOH 14]. A typical engineering diagrams for a lean Duplex SS grade (LX 2101) is shown on figure III.23. These diagrams show the risk areas for pitting in terms of chloride concentration and temperature. The solid points indicated that E_p is lower than the selected potential and open points indicate that it is higher or equal.

If the E_{OCPmax} is lower than the E_p , pitting is not expected, whereas pitting corrosion will take place when E_{OCPmax} higher than E_{pit} . If E_{OCPmax} is close to E_p pitting corrosion may occur, since even slight changes in the oxidizing concentration may raise the E_{OCPmax} to

E_p . The difference between the E_p and E_{OCPmax} , can be considered as a margin of safety and used as an indicator of the susceptibility to pitting corrosion [MAM 19].

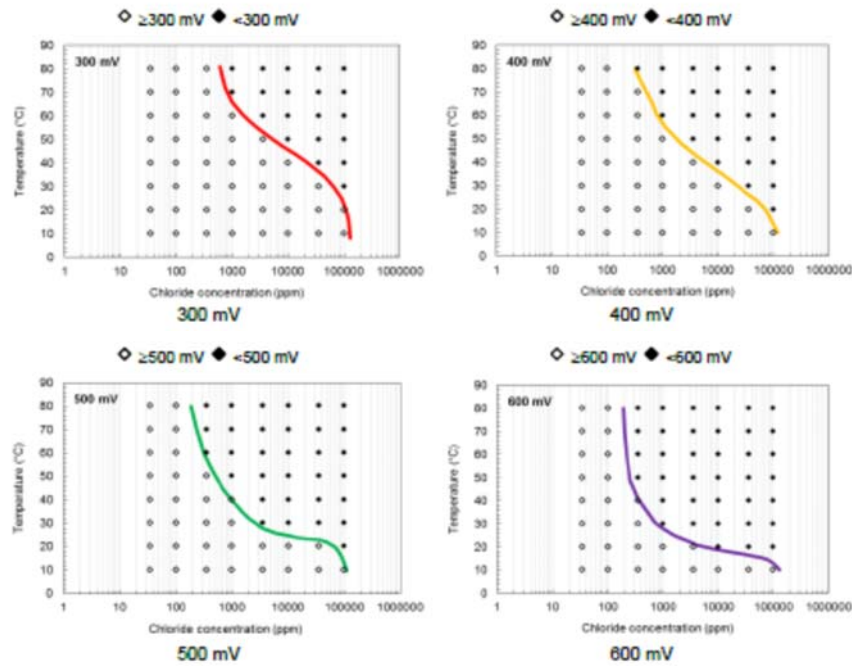


Figure III.23: Potential diagram for Lean Duplex SS (LDX 2101) at the different selected potentials [MAM 14].

As it can be noticed, the construction of such potential diagrams requires the determination of pitting potential at different temperatures.

However, in the current study the pitting potential measurements were performed at a fixed temperature ($\sim 25^\circ\text{C}$). Therefore an alternative approach based on the concept of engineering potential diagram has been adopted to analyze the obtained results.

The alternative approach consist to present the pitting potential values of the different aged samples tested in both testing solutions. A critical potential of 700 mV(SCE) was defined as a boundary limit.

Similarly to the engineering diagrams, the obtained pitting potentials are mapped on the matrix provided on table III.13. The green cells indicate that E_p is lower than the selected potential and red cells indicate that it is higher or equal.

Table III.13: Matrix of acceptable and unacceptable pitting potentials at 25°C based on the concept of Engineering diagrams.

Aging time (min)	0	5	30	60	360
Sigma (%)	0	0,6%	3,3%	3,9%	11,1%
Seawater Solution					
Produced Water					

As it can be seen from this matrix, a sigma content of ~3% will not be acceptable for produced water system operating at 25°C, basing on the previous criterion.

Also, it is important to highlight that this matrix is only valid for systems operating at a service temperature lower than 25°C , as a decrease in the pitting potential is expected to be found at higher temperatures as confirmed by many research works [SED 86, WAN 88, QVA 89, FIE 89, MAM 19].

5.4 Pitting morphology and its relation to sigma phase

To understand the effect of aging on pits morphologies and the relation between sigma phase and pitting nucleation sites, the pitted samples have been analyzed using SEM observations with secondary electron image (SEI) and backscattered electron image (BEI). Figure III.24 displays the typical SEM images of pitted samples after polarization tests in simulated seawater solution.

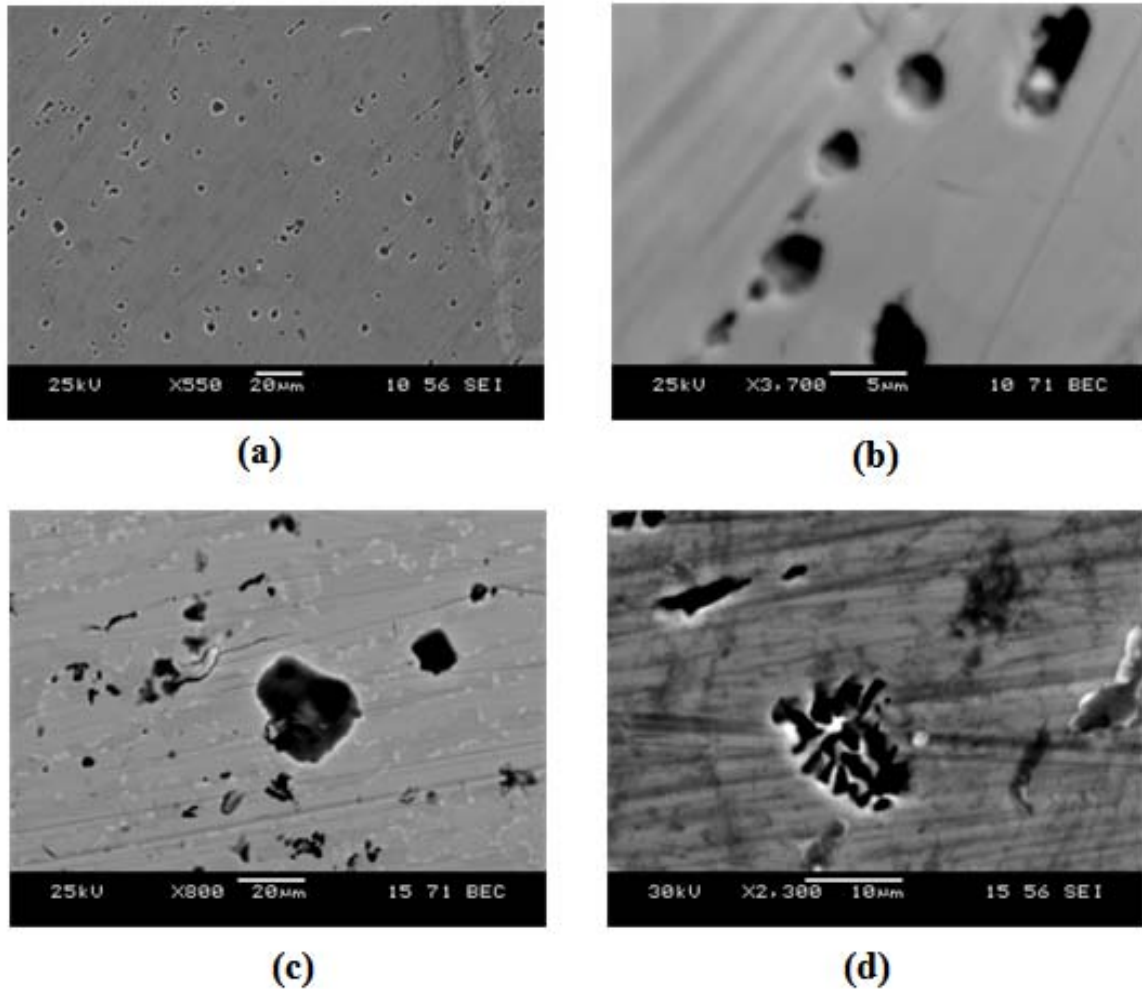


Figure III.24: SEM images of pitted samples (a) and (b) solution treated sample, (c) and (d) aged samples for 60 min at 850°C.

Small size isolated pits are observed in the solution treated sample while severe pitting corrosion is registered in the aged sample for 60 min with a larger size pits compared to the solution treated sample. In particular Figure III.24(d) presents a “lacy pattern pit morphology”, similar to the observations made by other research groups [MAG 05, SAN 13, SAN 14] (see **Annex A**). It is well observed also that pits initiated close to sigma phase regions which is an indication that pits nucleate preferentially at sigma phase interfaces. This finding can be explained by the fact that sigma phase precipitation could lead to the development of Cr- and Mo-depleted zones around the sigma phase, formed by secondary ferrite and by secondary austenite. Thus pit growth occurs as selective corrosion of the metallic matrix surrounding the sigma phase, which is explained by the presence of Cr- and Mo-depleted ferrite or

austenite phases surrounding the sigma, as a consequence of the lower corrosion resistance of those secondary phases [MAG 05].

6. Impact of sigma phase on hardness

The results of the hardness measurement of the treated samples are plotted on Figure III.25. The general trend observed in this figure stipulates that when the holding time is increased the hardness is increased consequently; this is due to sigma phase volume ratio present in the matrix of the aged samples. The higher sigma phase amount, the higher hardness value. In fact, the hardness of the σ phase is significantly greater than that for the χ phase; ferrite or austenite [AKI 12], therefore the increase in the hardness is attributed to the increasing in concentration of the σ phase.

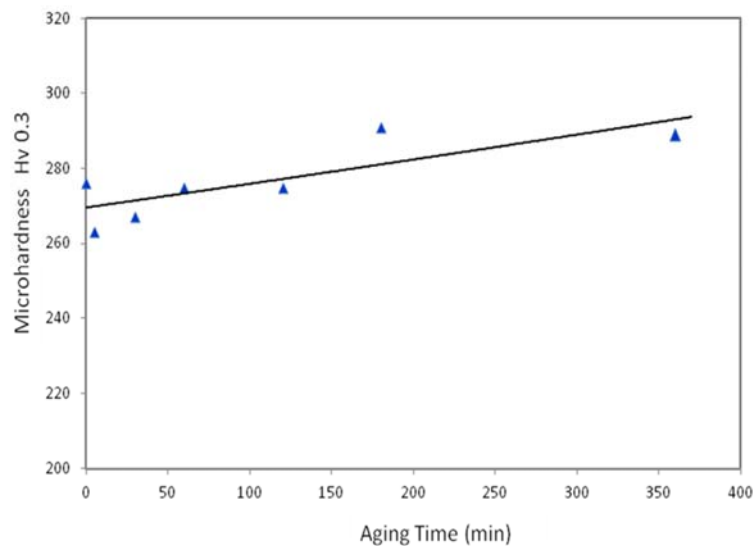


Figure III. 25: Microhardness evolution as a function of aging time at 850°C for the studied DSS (UNS S31803).

However, it was noted that short-term aging at 850°C results in little decrease in hardness, compared to the hardness of the base material (276 Hv). This slight reduction in hardness for short-term aged samples is probably associated to reduction in solute content of ferrite to nucleate sigma phase, particularly reduction in chromium and molybdenum content [MAG 03]. But generally speaking it is well established that the hardness is not a sensitive measure for low sigma content as indicated by Nilsson et al [NIL 00].

General Conclusions and Future Works

In this work the sigma phase precipitation in UNS 31803 DSS during isothermal aging at 850°C has been investigated. The effect of sigma phase on pitting corrosion resistance and hardness behavior was also studied. It constitutes a good background for understanding the quantitative correlation between sigma phase amount and corrosion resistance. The kinetic of embrittlement process associated with α - α' phase separation was also investigated in the current study using DSC technique coupled with Kissinger analysis

The principal conclusions that can be drawn from this work are the followings:

- The microstructure evolution of the aged material has been interpreted in terms of (σ) sigma phase precipitation on the basis of image analysis and XRD. The obtained diffraction peaks are in good agreement with the analysis of metallographic images of aged DSS samples. The results show that the duplex stainless steel UNS31803 is very sensitive to the formation of sigma phase at 850°C.
- The evidence shows that short-term aging at 850°C of UNS S31803 DSS leads to sigma phase precipitation following a preferential nucleation at ferrite / austenite interfaces.
- Increasing the holding time at 850°C has the effect to increase the volume fraction and particle size of (σ) sigma phase. The higher holding time, the higher amount of (σ) sigma phase.
- The kinetics of sigma phase formation study by the JMA model confirmed the change on the mechanism of sigma phase formation from nucleation and growth from ferrite to a diffusion-controlled growth-coarsening stage as observed in the optical and SEM micrographs.
- The application of the modified JMA model shows a good agreement between the experimental values and calculated ones, with only one kinetic slope and an impingement factor ($c = 0.4$), indicating that this model is probably more advantageous for sigma phase kinetic prediction in aged DSS grades, because it incorporates more free fitting parameters. However, more scientific efforts are needed

for a better understanding of the physical mechanisms behind the impingement factor and its typical values.

- The peaks associated with the redissolution of α' -chromium-rich phase in the investigated DSS has been successfully detected by Differential Scanning Calorimetry (DSC) technique.
- The DSC technique has allowed the determination of activation Energy related to DSS embrittlement at 475°C. The determined activation energy (138 kJ/mol) was close the value found by other research groups.
- Solution treated DSS samples show a high pitting corrosion resistance in both test solutions, simulated sea water and produced water, making this material grade highly suitable for use in chloride containing environments. However, serious deterioration of corrosion properties occurs in presence of sigma phase which may be introduced into the DSS microstructure in most cases as a result of inappropriate heat treatment. The results show that even about 3.3 % of sigma volume fraction is sufficient to cause a significant reduction on the pitting corrosion resistance of the UNS 31803 DSS.
- It was concluded that both sigma phase amount and chloride concentration worsen the pitting potential. The higher sigma content, the lower pitting potential and the higher chloride concentration, the lower pitting potential.
- Pitting nucleates preferentially at sigma phase interfaces for the aged specimens due to the development of Cr- and Mo-depleted zones around the sigma phase, formed by secondary ferrite and by secondary austenite.
- Hardness is not a sensitive parameter for low amounts of sigma phase. Hardness is significantly affected by higher sigma phase content.

Future work

Further experiments can be carried out to provide better understanding of the corrosion performance of the aged DSS in other oil and gas solutions.

Also below are some proposed future works:

- Perform more studies on the kinetic of sigma phase using the modified JMA model on various DSS grades to understand the physical mechanisms behind the impingement factor and to establish its typical values.
- Using differential Scanning Calomerty technique (DSC) to follow the kinetic of sigma phase precipitation at 850°C.
- Establish empirical formulation between the sigma phase volume fraction and the pitting potential in deferent test solutions.
- The present work can be extended to investigate other Duplex stainless steel grades, namely the lean duplex grade which are less prone to sigma precipitation in similar environments of this study.
- Investigate the repassivation potential of aged DSS in similar environments of this study.
- The present work can be extended to study other forms of corrosion in oil and gas environment namely the corrosion stress cracking (CSC) phenomena.

REFERENCES

- [AKI 12] A.R. Akisanya et al., Effect of ageing on phase evolution and mechanical properties of a high tungsten super-duplex stainless steel, *Materials Science and Engineering A* 535, 281– 289, 2012.
- [ALV 09] I. Alvarez-Armas, S. D. Moreuil, *Duplex Stainless Steels*, ISTE Ltd and John Wiley & Sons, Inc, 2009.
- [API 15] API 938 C, Use of Duplex Stainless Steels in the Oil Refining Industry, API TECHNICAL REPORT 938-C THIRD EDITION, FEBRUARY 2015.
- [ARI 12] M. E. Arikan, R. Arikan, M. Doruk, Determination of Susceptibility to Intergranular Corrosion of UNS 31803 Type Duplex Stainless Steel by Electrochemical Reactivation Method, *International Journal of Corrosion*, Vol. 2012, 2012.
- [ARO 10] B. Aronsson, On the origins and early growth of stainless steel: A survey with emphasis on the development in Sweden, *Outokumpu Stainless research foundation*, 2010.
- [ASM 00] *Introduction to Stainless Steels*, 2000 ASM International, www.asminternational.org.
- [ASM 05] *ASM Handbook, Volume 1, Properties and Selection: Irons, Steels, and High Performance Alloys, Section: Specialty Steels and Heat-Resistant Alloys*, Revised by A.M. Bayer, T. Vasco, and L.R. Walton, *Latrobe Steel Company*, 2005.
- [AST 18] ASTM G150-18 (2018), Standard Test Method for Electrochemical Critical Pitting Temperature Testing of Stainless Steels and Related Alloys, *ASTM International*, West Conshohocken, PA, 2018.
- [AVR 39] M.J. Avrami, Kinetics of phase change. A general theory. *Chem Phys* 7: 1103, 1939.
- [BAD 08] R. Badji, M. Bouabdallah, B. Bacroix, C. Kahloun, K. Bettahar, Effect of solution treatment temperature on the precipitation kinetic of σ -phase in 2205 duplex stainless steel welds. *Materials Science and Engineering* 496: 447-454, 2008.
- [BAD 14] R. Badji, N. Kherrouba, B. Mehdi, B. Cheniti, M. Bouabdallah, Precipitation kinetics and mechanical behavior in a solution treated and aged dual phase stainless steel. *Materials Chemistry and Physics* 148: 664-672, 2014.
- [BAI 27] E.C. Bain, W.E. Griffiths, *Introduction to the Iron-Chromium-Nickel Alloys*,

- Trans. AIME, vol. 75, 166–211, 1927.
- [BAR 93] E. Bardal, et al., The Behavior Of Corrosion-Resistant Steels In Seawater: A Review, Corrosion Science, Vol. 35, Nos 1-4, pp. 257-267. 1993.
- [BHA 06] H. K. D. H. Bhadeshia, Steels, Microstructure and Properties, Third edition, Published by Elsevier Ltd, 2006.
- [BON 90] S. Bonnet, J. Bourgoïn, J. Champredonde, D. Guttman and M. Guttman, Relationship between evolution of mechanical properties of various cast duplex stainless steels and metallurgical and aging parameters: outline of current EDF programs Mater. Sci. Technol., vol. 6, n. 3, 221–229, 1990.
- [BRO 91] J.E. Brown, G.D.W. Smith, Atom probe studies of spinodal processes in duplex stainless steels and single- and dual-phase Fe-Cr-Ni alloys, Surface Science 246, 285-291, 1991.
- [BUC 12] R.A. Buchanan and E.E. Stansbury, Electrochemical Corrosion, Handbook of Environmental Degradation of Materials, Elsevier Inc, 2012.
- [CAL 13] I. Calliari, M. Breda, E. Ramous, M. Magrini, G. Straffelini: Effect of isothermal heat treatments on Duplex Stainless Steels impact toughness, In: Convegno Nazionale IGF XXII, 1-3 Luglio, Roma, Italia, p. 56-65, 2013.
- [CAR 94] J.A. Carew, M. Abdel-Jawad, A. Julka, British Corrosion Journal, 29, 275–279, 1994.
- [CER 10] R. Cervo, Experimental and Numerical Analysis Of Welding And Heat Treatment Of Duplex Stainless Steels, PhD thesis, University of Padua, 2010.
- [CHA 10] J. Charles and P. Chemelle, The history of duplex developments, nowadays DSS properties and duplex market future trends, 8th Duplex Stainless Steels conference, 13-15 October 2010, Beaune, France.
- [CHA 82] J. Chance, W. Coop, K.J. Gradwell, C.V. Roscoe: Conf proc Duplex Stainless Steels '82, St Louis, ASM, 371-398, 1982.
- [CHA 91] J. Charles, Proc. Duplex Stainless Steels 91, Beaune, France, 1, 3-48, 1991.
- [CHE 01] H.T. Chen, J.R. Yang, Effects of Solution Treatment and Continuous Cooling on σ Phase Precipitation in a 2205 Duplex Stainless Steel. Mater. Sci. Eng. A, 311: 28-41, 2001.
- [CHI 12] H. Chih-Chun, W. Weite, Overview of Intermetallic Sigma (σ) Phase Precipitation in Stainless Steels, International Scholarly Research Network ISRN Metallurgy Volume 2012, Article ID 732471, 2012.

- [CHO 13] H.S. Cho, K. Lee, Effect of cold working and isothermal aging on the precipitation of sigma phase in 2205 duplex stainless steel. *Materials Characterization* 75: 29-34, 2013.
- [CHR 75] J. W. Christian: *The Theory of Transformations in Metals and Alloys*, 2nd Edition, Part I, Oxford: Pergamon, 1975.
- [CHU 90] H. M. Chung, T. R. Leax, Embrittlement of laboratory and reactor aged duplex steels, *Materials Science and Technology* March 1990 Vol. 6, 1990.
- [CHU 92] H. M. Chung, Aging and Life Prediction of Cast Duplex Stainless Steel Components, *Int. J. Pres. Ves. & Piping* 50 ,179-213, 1992.
- [COU 14] L. Couturier, Caractérisation des évolutions microstructurales de l'acier inoxydable martensitique à durcissement structural 15-5PH au cours du vieillissement thermique, Thèse Doctorat, Université de Grenoble, 2014.
- [DAN 00] F. Danoix, P. Auger, Atom Probe Studies of the Fe–Cr System and Stainless Steels Aged at Intermediate Temperature : A Review, *Materials Characterization*, vol. 44, p. 177 – 201, 2000.
- [DAT 01] P. Datta, G.S. Upadhyaya, *Materials Chemistry and Physics* 67, 234, 2001.
- [DEN 09] B. Deng, Z. Wang, Y. Jiang, H. Wang, J. Gao, J. Li, Evaluation of localized corrosion in duplex stainless steel aged at 850 °C with critical pitting temperature measurement. *Electrochim. Acta* , 54, 2790–2794, 2009.
- [DOM 06] M.A. Domínguez-Aguilar, R.C. Newman, Detection of deleterious phases in duplex stainless steel by weak galvanostatic polarization in halide solutions. *Corros. Sci.* 48, 2577–2591, 2006.
- [DON 11] C. Dong et al., Effect of Temperature and Cl⁻ Concentration on Pitting of 2205 Duplex Stainless Steel, *Journal of Wuhan University of Technology-Mater. Sci. Ed.* Aug. 2011.
- [EBR 11] N. Ebrahimi, M.H. Moayed, A. Davoodi , Critical pitting temperature dependence of 2205 duplex stainless steel on dichromate ion concentration in chloride medium, *Corrosion Science* 53, 1278–1287, 2011.
- [EBR 12] N. Ebrahimi, M. Momeni, A. Kosari, M. Zakeri, M.H. Moayed, A comparative study of critical pitting temperature (CPT) of stainless steels by electrochemical impedance spectroscopy (EIS), potentiodynamic and potentiostatic techniques. *Corros.Sci.*, 59, 96–102, 2012.

- [EGH 11] F. Eghbali, M.H. Moayed, A. Davoodi, N. Ebrahimi, Critical pitting temperature (CPT) assessment of 2205 duplex stainless steel in 0.1 M NaCl at various molybdate concentrations, *Corrosion Science* 53, 513–522, 2011.
- [ELM 06] J. W. Elmer, T. A. Palmer, E. D. Specht, Direct Observations of Sigma Phase Formation in Duplex Stainless Steels using In Situ Synchrotron X-Ray Diffraction, *Metallurgical Transactions A*, UCRL-JRNL-222558, 2006.
- [ELM 07] J.W. Elmer, T.A. Palmer, E.D. Specht: *Metall. Mater. Trans. A*, vol. 38A, pp. 464–75, 2007.
- [ESC 09] D.M. Escriba, E. Materna-Morris, R..L. Plaut., A.F. Padilha, Chi-phase precipitation in a duplex stainless steel. *Mater Charact* ,60:1214–1219, 2009.
- [EZU 07] H. M. Ezuber, A. El-Houd, F. El-Shawesh, Effects of sigma phase precipitation on seawater pitting of duplex stainless steel, *Desalination*, Vol. 207, 2007, p. 268–275, 2007.
- [FAR 19] C.R. de Farias Azevedo et al, An overview of the recurrent failures of duplex stainless steels, *Engineering Failure Analysis* 97, 161–188, 2019.
- [FER 12] P. Ferro, F. Bonollo, G. Timelli, Sigma phase precipitation modelling in a UNS S32760 superduplex stainless steel, *La Metallurgia Italiana* - n. 5, 2012
- [FER 17] P. Ferro, A. Fabrizi, J.O. Nilsson, Intermetallic Phase Precipitation in Duplex Stainless Steels: Considerations on the Use of Johnson-Mehl-Avrami-Kolmogorov Equation, *Res Rep Metals*, 1:2, 2017.
- [FIE 89] J. W. Fielder, D. R. Johns, Pitting corrosion engineering diagrams for stainless steels, *Corrosion* 89, Blackpool, U.K, November 8-10, vol 1, pp. 1.33-1.49, 1989.
- [GAB 07] P. Gabbott, Chapter 1: A Practical Introduction to Differential Scanning Calorimetry, 2007.
- [GHA 15] M. Ghahari et al., Synchrotron X-ray radiography studies of pitting corrosion of stainless steel: Extraction of pit propagation parameters, *Corrosion Science* 100, 23–35, 2015.
- [GLO 20] <http://www.globalsino.com/EM/page3882.html>
- [GOO 87] P. D. Goodman, Effect of chlorination on materials for sea water cooling systems: a review of chemical reactions, *British Corrosion Journal*, vol. 22 (1), pp. 56-62, 1987.
- [GOW 42] J. T. Gow and O. E. Harder, Balancing the composition of cast 25 per cent chromium-12 per cent nickel type alloys, *Transactions of the American Society for*

Metals, vol. 30, pp.855–935, 1942.

- [GUN 03] R.N. Gunn, Duplex stainless steels Microstructure, properties and applications, Published by Abington Publishing, England, 2003.
- [GUO 16] W. Guo et al, An atom probe perspective on phase separation and precipitation in duplex stainless steels, Nanotechnology 27, 254004, 2016.
- [HAI 95] P.J. Haines and F.W. Wilburn, Differential thermal analysis and differential scanning calorimetry, Springer, Dordrecht, 1995.
- [HAS 79] Hashimoto K, Asami K, Teramoto K: An X-ray photo-electron spectroscopic study on the role of molybdenum in increasing the corrosion resistance of ferritic stainless steels in HCl, Corrosion Science, 1979, 19,3-14, 1979.
- [HER 06] E. HERNY, Caractérisation mécanique et étude des mécanismes de vieillissement thermique et thermomécanique de l'acier inoxydable martensitique 15-5 PH, soudé par faisceau d'électrons, thèse de doctorat en Science et Génie des matériaux, Institut National Polytechnique de Toulouse, 2006.
- [HOC 50] Hochmann J: Aciers inoxydables a structure austeno-ferritique - Revue du Nickel,7,8,9, 53-60, 1950.
- [HOF 94] H. Hoffmeister, G. Lothongkum, Quantitative effects of nitrogen contents and cooling cycles on δ - γ transformation, chromium nitride precipitation and pitting corrosion after weld simulation of duplex stainless steels, Proc. of the Duplex Stainless Steels 94, Glasgow, Scotland 1994.
- [HUA 05] C.S. Huang, C.C. Shih, Effects of nitrogen and high temperature aging on σ phase precipitation of duplex stainless steel. Materials Science and Engineering 402, 66-75, 2005.
- [IMO 09] Practical Guidelines for the Fabrication of Duplex Stainless Steels, Published by the International Molybdenum Association (IMOA), London, UK, 2009.
- [JOH 00] R. B. Johansen, B. H. Leinum, S. Karlsen, H. A. Trandem, G. Valdø, A. O. Tjernæs, T. Helgesen, In: Proc. Conf. Duplex 2000, Edited by AIM. Associazione Italiana di Metallurgia, 405, 2000.
- [JOH 14] E. Johansson, S. H. Mameng, Long term corrosion test of stainless steel for water heater applications, Eurocorr 2014, Pisa, Italy, 2014.
- [KAI 14] W. Kai Chan, S.C. Tjong, Effect of Secondary Phase Precipitation on the Corrosion Behavior of Duplex Stainless Steels, Materials, 7, 5268-5304, 2014.

- [KAS 12] A. Kashiwar, N.P. Vennela, S.L. Kamath, R.K. Khatirkar, Effect of solution annealing temperature on precipitation in 2205 duplex stainless steel. *Materials Characterization* 74: 55-63, 2012.
- [KAS 17] S. Kasap, J. Málek, R. Svoboda, *Thermal Properties and Thermal Analysis*, Springer International Publishing AG, 2017.
- [KES 09] H. Keshmiri, A. Momeni, K. Dehghani, G. R. Ebrahimi, G. Heidari: Effect of Aging Time and Temperature on Mechanical Properties and Microstructural Evolution of 2205 Ferritic-Austenitic Stainless Steel, *Journal of Materials Science & Technology*, Vol. 25, No. 5, p. 597-602, 2009.
- [KOD 14] K.V. Kodre, S.R. Attarde, P.R. Yendhe, R.Y. Patil, V.U. Barge VU, *Differential Scanning Calorimetry: A Review*, RRJPA, Volume 3, Issue 3, 2014.
- [KOT 92] D.J. Kotecki, T.A. Siewert: WRC-1992 constitution diagram for stainless steel weld metals: a modification of the WRC-1988 diagram, *Welding Research Supplement*, 171-178, 1992.
- [LEA 92] T.R. LEAX, S.S. BRENNER, J.A. SPITZNAGEL, Atom Probe Examination of Thermally Aged CF8M Cast Stainless Steel, *METALLURGICAL TRANSACTIONS A, VOLUME 23A*, 2725, 1992.
- [LEE 90] E.S. Lee, Y.G. Kim, A transformation kinetic model and its application to Cu-Zn-Al shape memory alloys–I. Isothermal conditions. *Acta metal Mater* 38, 1669-1676, 1990.
- [LEF 97] Leffler B: Avesta Sheffield AB. Private communication dated 3 January 1997.
- [LEG 81] M.T. Leger, “Prévision et contrôle du taux de ferrite dans les moulages en acier inoxydable,” *Fonderie – Fondateur d’aujourd’hui*, vol. 10, 15–23, 1981.
- [LEG 88] M.T. Leger, P. Degas, J.C Plumerez, P. Ould and Y. Meyzaud, Caractéristiques physiques d’aciers inoxydables austénitiques moulés pour réacteurs à eau pressurisée, *Fonderie – Fondateur d’aujourd’hui*, vol. 78, 31–49, 1988.
- [LIA 01] J. Liao, “Nitride Precipitation in Weld HAZs of a Duplex Stainless Steel”, *ISIJ International*, Vol. 41, N°5, 460, 2001.
- [LIN 20] <https://www.linseis.com/en/properties/heat-flow/>
- [LIP 16] T. Lipinski Corrosion Rate of the X2CrNiMoN22-5-3 Duplex Stainless Steel Annealed at 500 C, *ACTA PHYSICA POLONICA A*, Vol. 130, 2016.
- [LON 18] M. Long et al., Using differential scanning calorimetry to characterize the precipitation and dissolution of V(CN) and VC particles during continuous casting

and reheating process, Materials Research Society, 2018.

- [LON 94] R.D. Longbottom, F.J. Hayes, “Effects of variations in alloying element content and temperature on the austenite-ferrite phase balance in duplex stainless steels.” In Proceedings of Duplex Stainless Steels 94, Glasgow, vol. 1, Materials and Properties, Abington Publishing, 1994.
- [LU 91] Y. C. Lu, J. L. Luo, M. B. Ives, The influence of chlorination of saline environments on localized corrosion of stainless steels, ISIJ International, vol. 31 (2), pp. 210-215, 1991.
- [MAE 14] J.Y. Maetz, Évolution de la microstructure d’un acier inoxydable lean duplex lors du vieillissement, Thèse de Doctorat en Sciences des Matériaux, l’Institut National des Sciences Appliquées de Lyon, 2014.
- [MAG 03] R. Magnabosco, L. E. Oiyé, C. K. Sutto : Microhardness of UNS S31803 (SAF 2205) duplex stainless steel after isothermal aging between 700°C and 900°C, In: 17th International Congress of Mechanical Engineering, São Paulo, November 10-14, p. 1-7, 2003.
- [MAG 05] R. Magnabosco, N. Alonso-Falleiros, Pit Morphology and its Relation to Microstructure of 850°C Aged Duplex Stainless Steel, CORROSION—Vol. 61, No. 2, 2005.
- [MAG 09] R. Magnabosco, Kinetics of Sigma Phase Formation In a Duplex Stainless Steel, Materials Research, Vol. 12, No. 3, 321-327, 2009.
- [MAI 18] G. Maistro, Low-temperature carburizing/nitriding of austenitic stainless steels - Influence of alloy composition on microstructure and properties, PhD Thesis, Gothenburg, Sweden 2018.
- [MAM 14] S.H. Mameng, R. Pettersson, Limiting conditions of pitting corrosion for lean duplex stainless steel as a substitute for standard austenitic grades, Proceedings of Eurocorr, Pisa, Italy, 2014.
- [MAM 19] S.H. Mameng, Localised corrosion and atmospheric corrosion of stainless steels, Doctoral Thesis, Division of Surface and Corrosion Science Stockholm, 2019.
- [MAR 09] M. Martins, L.C. Casteletti. Sigma phase morphologies in cast and aged super duplex stainless steel. Mater. Charact., 60, 792–795, 2009.
- [MAT 13] T. Mathiesen, C. Jensen: Rapid Corrosion Test for Detecting Intermetallic Phases in Duplex Stainless Steels, In: NACE Corrosion 2013, Orlando, FL, Paper 02583, ,

p. 1-12, 2013.

- [MEH 90] H. Mehrer, Ed. Landolt-Börnstein, New Series, Group III : volume 26, Diffusion In Solids Metals and Alloys, Springer, 1990.
- [MER 03] R. Merello, F.J. Botana, J. Botella, M.V. Matres, M. Marcos “Influence of chemical composition on the pitting corrosion resistance of non-standard low-Ni high-Mn–N duplex stainless steels”, Corrosion Science 45, 909, 2003.
- [MEY 11] N. Meyer, M. Mantel, A. Gauthier, C. Bourgin, Long term aging of various duplex stainless steels between 250°C and 400°C – relationship between toughness measurements and metallurgical parameters, Revue de Métallurgie, vol. 108, page 213–223, 2011.
- [MIC 06] J. Michalska J, M. Sozańska, Qualitative and quantitative analysis of σ and χ phases in 2205 duplex stainless steel. Mater. Charact., 56, 355–362, 2006.
- [MIK 09] A. Mikó, J. W. Erning, H. Schlerkmann, T. Mathiesen, Comparative investigation of stainless steels used in drinking water distribution systems, Electrochimica Acta, vol. 54, pp. 7507–7513, 2009.
- [MIL 95] M.K. Miller, J.M. Hyde , A. Cerezo, G.D.W. Smith, Comparison of low temperature decomposition in Fe-Cr and duplex stainless steels, Applied Surface Science 87/88, 323-328, 1995.
- [MIL 96] M.K. Miller, K.F. Russell, Comparison of the rate of decomposition in Fe-45%Cr, Fe-45%Cr-5%Ni and duplex stainless steels, Applied Surface Science 94–95, 398–402, 1996.
- [MIT 88] E.J. Mittemeijer, L. Cheng, P.J. Van der Schaaf, C.M. Brakman, B.M. Korevaar, Analysis of nonisothermal transformation kinetics; tempering of iron-carbon and iron-nitrogen martensites. Met Trans.19A:925–32, 1988.
- [MOU 08] V.S. Moura et al, Influence of microstructure on the corrosion resistance of the duplex stainless steel UNS S31803, Materials Characterization 59, 2008.
- [NA 00] Y. S. Na, N. K. Park, R. C. Reed, Sigma morphology and precipitation mechanism in Udimet 720Li, Scripta Materialia, vol. 43, no. 7, pp. 585–590, 2000.
- [NAN 20] <https://www.nanoimages.com/sem-technology-overview/>.
- [NIL 00] J.O. Nilsson, P. Kangas, T. Karlsson, A. Wilson, Mechanical properties, microstructural stability and kinetics of σ -phase formation in 29Cr-6Ni-2Mo-0.38N superduplex stainless steel. Metallurgical and Materials Transactions 31A,

35-45, 2000.

- [NIL 92] J.O. Nilsson, B. Wilson, B. Josefsson, T. Thorvaldsson, "Relationship between pitting corrosion, toughness and microstructure for isothermally heat-treated super duplex stainless steel", Applications of Stainless Steel '92, Stockholm, Sweden, 280, 1992.
- [NIL 95] J.O. Nilsson, L. Karlsson, J.O. Anderson, Secondary austenite formation and its relation to pitting corrosion in duplex stainless steel weld metal, Materials Science and Technology 11, pp. 276-283, 1995.
- [OBE 17] N.U. Obeyesekere, Pitting corrosion, Trends in Oil and Gas Corrosion Research and Technologies, Elsevier Ltd, 2017.
- [OGA 82] Ogawa T, Aoki S, Sakamoto T, Zaizen T, The Weldability of Nitrogen-Containing Austenitic Stainless Steel: Part I-Chloride Pitting Corrosion Resistance, Welding Journal 61(5), 139-148, 1982.
- [OUT 13] Handbook of Stainless Steel, Outokumpu Stainless AB Avesta Research Centre, 2013.
- [PAD 02] A. F. Padilha, P. R. Rios, "Decomposition of austenite in austenitic stainless steels," ISIJ International, vol. 42, no. 4, pp.325–337, 2002.
- [PAL 05] T.A. Palmer, J.W. Elmer, S.S. Babu, E.D. Specht, Direct Observations of Sigma Phase Growth and Dissolution in 2205 Duplex Stainless Steel, Trends in Welding Research Pine Mountain, GA, United States May 16, 2005 through May 20, 2005
- [PAR 05] C.J. Park, V.S. Rao, H.S. Kwon, Effects of sigma phase on the initiation and propagation of pitting corrosion of duplex stainless steel. Corrosion, 61, 76–83, 2005.
- [PAR 11] C. Pareige, S. Novy, S. SAILLET, P. Pareige, Study of phase transformation and mechanical properties evolution of duplex stainless steels after long term thermal ageing (>20 years), Journal of Nuclear Materials, vol. 411, p. 90-96, 2011.
- [PAR 15] C. Pareige, J. Emo, S. SAILLET, C. Domain, P. Pareige, Kinetics of G-phase precipitation and spinodal decomposition in very long aged ferrite of a Mo-free duplex stainless steel, Journal of Nuclear Materials 465, 383-389, 2015.
- [POH 07] M. Pohl et al, Effect of intermetallic precipitations on the properties of duplex stainless steel, Materials Characterization 58, 65–71, 2007.

- [POH 08] P. Pohjanne, L. Carpén, T. Hakkarainen, P. Kinnunen, A method to predict pitting corrosion of stainless steels in evaporative conditions, *Journal of Constructional Steel Research* 64, 1325, 2008.
- [PRA 15] P. Prabhuji, R.Garg, Effect Of Intermetallic Phases On Corrosion Behavior and Mechanical Properties of Duplex Stainless Steel And Super-Duplex Stainless Steel, *Advances in Science and Technology Research Journal* Vol. 9 (27), 2015.
- [PUM 90] P. H. Pumphrey, K. N. Akhurst, Aging kinetics of CF3 cast stainless steel in temperature range 300-400°C, *Materials Science and Technology*, Vol. 6/211, 1990.
- [QVA 89] R. Qvarfort, Critical pitting temperature measurements of stainless steels with an improved electrochemical method, *Corrosion Science*, vol. 29 (8), pp. 987-993, 1989.
- [REN 11] L. Ren, J. Zhu, L. Nan, and K. Yang: Differential scanning calorimetry analysis on Cu precipitation in a high Cu austenitic stainless steel. *Mater. Des.* 32, 3980, 2011.
- [RIV 18] B. Rivolta et al, The dilatometric technique for studying sigma phase precipitation kinetics in F55 steel grade, *Journal of Thermal Analysis and Calorimetry*, 2018.
- [ROB 94] C.V. Robino, P.W. Hochanadel, G.R. Edwards, M.J. CIESLAK, Heat Treatment of Investment Cast PH 13-8 Mo Stainless Steel: Part II. Isothermal Aging Kinetics, *Metallurgical and Materials Transactions A*, Volume 25A, APRIL 1994-697, 1994.
- [ROG 12] F. Roger, B. Glenn, G. Warburton, J. Wilson, QA/QC Tools to Ensure the Quality of Duplex Stainless Steel Components, *NACE Corrosion 2012*, C2012-0001096, 2012.
- [ROL 17] T.L. Roland, Study of the corrosion behaviour of S32101 duplex and 410 martensitic stainless steel for application in oil refinery distillation systems, *Journal of Materials Research and Technology*, Vol. 6, No.3, p. 203-212, 2017.
- [ROS 86] C.V. Roscoe, K.J. Gradwell: Proc conf Duplex Stainless Steels '86, The Hague, Nederlands Instituut voor Lastechniek, paper 34, 126-135, 1986.
- [RUI 89] G. Ruijin, S. C. Srivastava, M. B. Ives. Pitting corrosion behavior of UNS N08904 stainless steel in a chloride/sulfate solution, *Corrosion*, vol. 45, pp.874-882, 1989.
- [SAH 09] J.K. Sahu, U. Krupp, R.N. Ghosh, H.J. Christ, Effect of 475°C embrittlement on the mechanical properties of duplex stainless steel. *Mater. Sci. Eng. A*, 508, 1–14, 2009.

- [SAI 07] J.R. SAITHALA., Pitting and stress corrosion cracking of stainless steel, PhD Thesis, Sheffield Hallam University (United Kingdom), 2007.
- [SAI 12] J. R. Saithala, S. Mahajanam, H. S. Ubhi, J. D. Atkinson., Effect of Sigma Phase on the Environmental Assisted Cracking of Super Duplex Stainless Steel in Oil Field Environments, In: CORROSION 2012 Conference & Expo- NACE, C2012-0001272, 2012.
- [SAN 13] D.C. Dos Santos, R. Magnabosco, Carlos de Moura-Neto: Corrosion, Influence of Sigma Phase Formation on Pitting Corrosion of an Aged UNS S31803 Duplex Stainless Steel, vol. 69, pp. 900–11, 2013.
- [SAN 14] D.C. Dos Santos, R. Magnabosco, Influence of intermetallic phase content and microstructure on pitting potential of a duplex stainless steel, Conference Paper, EUROCORR 2014.
- [SAN 16] D.C. Dos Santos, R. Magnabosco, Kinetic Study to Predict Sigma Phase Formation in Duplex Stainless Steels, Metallurgical and Materials Transactions A, 1554—Volume 47A, April 2016.
- [SAT 99] Y. S. Sato, H. Kokawa, K. Okamoto, S. Hirano, M. Inagaki, Rapid formation of the sigma phase in 304 stainless steel during friction stir welding, Scripta Materialia, vol. 49, no. 12, pp. 1175–1180, 1999.
- [SAU 11] G. A. Saud, Corrosion Resistance Of Austenitic Stainless Steel In Acetic Acid Solution Containing Bromide Ions, PhD Thesis, The University of Manchester 2011.
- [SED 85] A.J. Sedriks, Conf proc Stainless Steels 84, Goteborg, Institute of Metals, 125-133, 1985.
- [SED 86] A. J. Sedriks, Effects of alloy composition and microstructure on the passivity of stainless steels, Corrosion, vol. 42 (7), pp. 376-386,1986.
- [SIK 83] V. K. Sikka, M. G. Cowgill, B. W. Roberts, Creep properties of modified 9Cr-1Mo Steel, in Proceedings of Topical Conference on Ferritic alloys for Use in Nuclear Energy Technologies, ASM International, 1983.
- [SMI 86] S. Smialowska et al., Pitting Corrosion of Metals. Houston, TX: NACE International, Inc., 1986.
- [SMI 98] G.W. Smith, Precipitation kinetics in an air-cooled aluminium alloy: a comparison of scanning and isothermal calorimetry measurements methods. *Thermochemica Acta.*, 313:27–36, 1998.

- [STE 12] D. Steiner et al, The effect of cooling rate on the solidification and microstructure evolution in duplex stainless steel, *J Therm Anal Calorim* 109:1185–1191, 2012.
- [STE 13] W. Sten, Applications of Computational Thermodynamics and Kinetics on Transformations in Stainless Steels, Doctoral Thesis in Engineering Materials Science Stockholm, Sweden 2013.
- [SUN 95] N.X. Sun, X.D. Liu, K. Lu, An explanation to the anomalous Avrami exponent, *Scr. Mater.* 34, 1201, 1995.
- [TRU 77] J.E. Truman, M.J. Coleman, K.R. Pirt, *British Corrosion Journal* 12, 236, 1977.
- [TRU 87] S.E. Truman, Effects of Composition on the Resistance to Pitting Corrosion of Stainless Steel, Proc. Conf. UK Corrosion 87. Brighton, England, Oct 26-28, 1987.
- [TUC 11] J.D. Tucker, A. Y. George A. Young, R.E. Daniel, Thermal Embrittlement of a Lean Grade of Duplex Stainless Steel: Alloy 2003, *Solid State Phenomena Vols.* 172-174, pp 331-337, 2011.
- [TUC 15] J.D. Tucker et al, Assessment of thermal embrittlement in duplex stainless steels 2003 and 2205 for nuclear power applications, *Acta Materialia* 87 (2015) 15–24.
- [VAR 18] B. Varbai, T. Pickle, K. Májlinger, Development and Comparison of Quantitative Phase Analysis for Duplex Stainless Steel Weld, *Periodica Polytechnica Mechanical Engineering*, paper 12234, 2018.
- [VEN 89] G. Ventura, E. Traverso, A. Mollica, Effect of NaClO Biocide additions in natural seawater on stainless steel corrosion resistance, *Corrosion*, vol. 45 (4), pp. 319-325, 1989.
- [VIL 06] D. M. E. Villanueva, F. C. P. Junior, R. L. Plaut, and A. F. Padilha, “Comparative study on sigma phase precipitation of three types of stainless steels: austenitic, superferritic and duplex,” *Materials Science and Technology*, vol. 22, no. 9, pp.1098–1104, 2006.
- [WAN 88] J. H. Wang, C. C. Su, Z. S. Smialowska, Effects of Cl⁻ Concentration and temperature on pitting of AISI 304 stainless steel, *Corrosion*, vol. 44 (10), pp. 733-737, 1988.
- [WEN 03] K. L. Weng, T. H. Chen, J. R. Yang, The High-Temperature and Low-Temperature Aging Embrittlement In A 2205 Duplex Stainless Steel, *Bulletin of the College of Engineering, N.T.U*, Vol. 89, p. 45-61, 2003.

-
- [WEN 04] K.L. Weng, H.R. Chen, J.R. Yang, The low-temperature aging embrittlement in a 2205 duplex stainless steel, *Materials Science and Engineering A* 379 (1–2) , 119–132, 2004.
- [WIL 94] M.E. Wilms, V.J. Gadgil, J.M. Krougmen, F.P. Ijsseling, The effect of σ -phase precipitation at 800 °C on the corrosion resistance in sea-water of a high alloyed duplex stainless steel, *Corros. Sci.* 36, 871, 1994.
- [YOU 11] M. Yousefieh, M. Shamanian, A. Saatchi, Influence of step annealing temperature on the microstructure and pitting corrosion resistance of SDSS UNS S32760 Welds. *J. Mater. Eng. Perform.*, 20,1678–1683, 2011.
- [ZOU 11] D. Zou et al, Sigma Phase Precipitation and Properties of Super-duplex Stainless Steel UNS S32750 Aged at the Nose Temperature, *Journal of Wuhan University of Technology-Mater. Sci. Ed.*, 2011.

Annex A

Miscellaneous information on the metallography of DSS

This informative annex contains some alternative etching reagents commonly used to characterize the microstructure of duplex stainless steel.

It is aimed also to show some typical micrographs and SEM images of DSS microstructures at different metallurgical conditions before and after corrosion tests from the best previous research works. Such micrographs can be considered as a good reference for a better understanding and analysis of the obtained results according to the observed morphologies.

A.1. Alternative recommended etching reagents used for Duplex stainless steel and their applications:

Table A.1: Recommended etchants for duplex stainless steels and their applications [VAR 18, MIC 06].

Etchant	Content	Application
Beraha	85 mL water 15 mL HCl 1g $K_2S_2O_5$	Colors ferrite but not austenite
Carpenter	85 mL ethanol 15 mL HCl	To reveal grain and phase boundaries
Electrochemical NaOH	100 mL water 10 g NaOH	Distinguish between chi and sigma phase
Grosbeck	100 mL water 4 g NaOH 4g $KMnO_4$	To reveal sigma phase and nitrides
Inhibited ferric chloride	100 mL water 5g $FeCl_3$ 1g $NaNO_3$	Detrimental phases in lean duplex steels
Murakami	100 mL water 10g NaOH 10g $K_3Fe(CN)_6$	Colors ferrite and sigma phase
Sodium Hydroxide	100 mL water 40g NaOH	Detrimental phases in duplex
Villela	5 ml HCl, 1g picric acid, 100 ml methanol (95%) or ethanol (95%)	Reveals ferrite, σ phase and carbides
Electrochemical KOH	10 N KOH	Reveals ferrite and σ phase

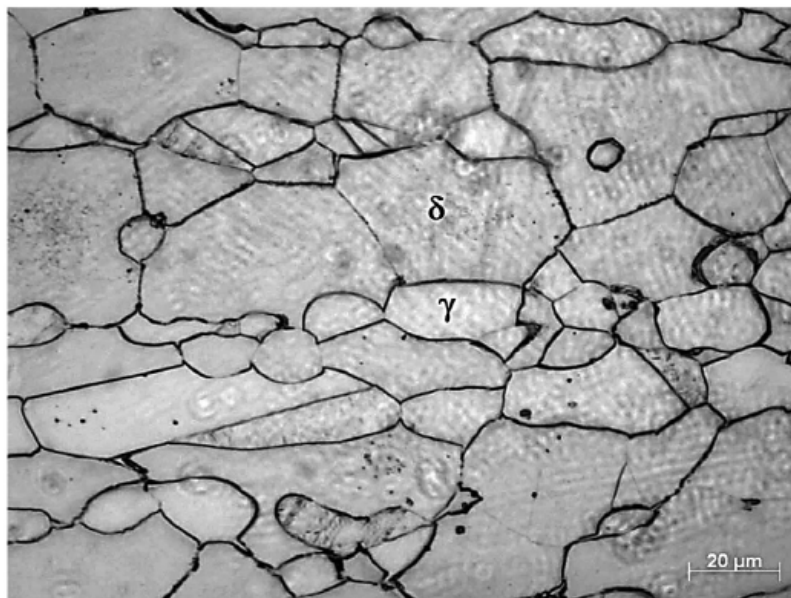
A.2. Typical metallography of DSS at different conditions:

Figure A.1: Optical micrograph of DSS at solution treated condition, after electrochemical etching is with a 32 N KOH [BAD 14].

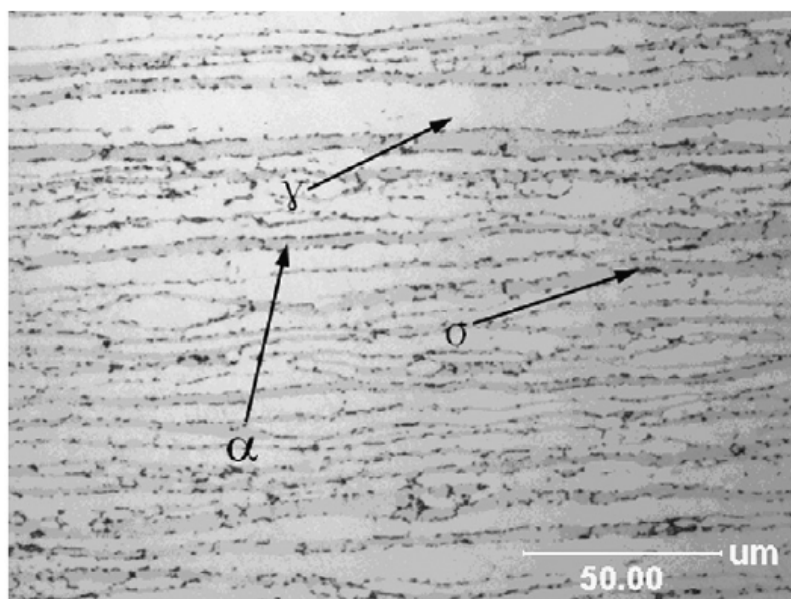


Figure A.2: Optical micrograph corresponding to a longitudinal section of aged DSS at 850°C for 2h, electrolytically etched in 30% KOH solutions [DEN09].

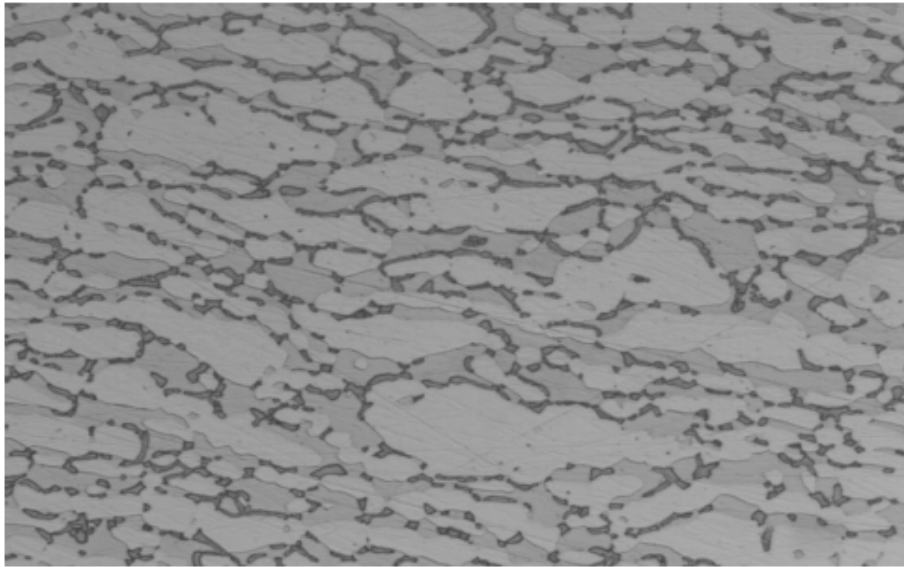


Figure A.3: Micro-section showing sigma phase precipitates in a super DSS fitting.

(electrolytically etched in oxalic acid then KOH; X500) [ROG 12].

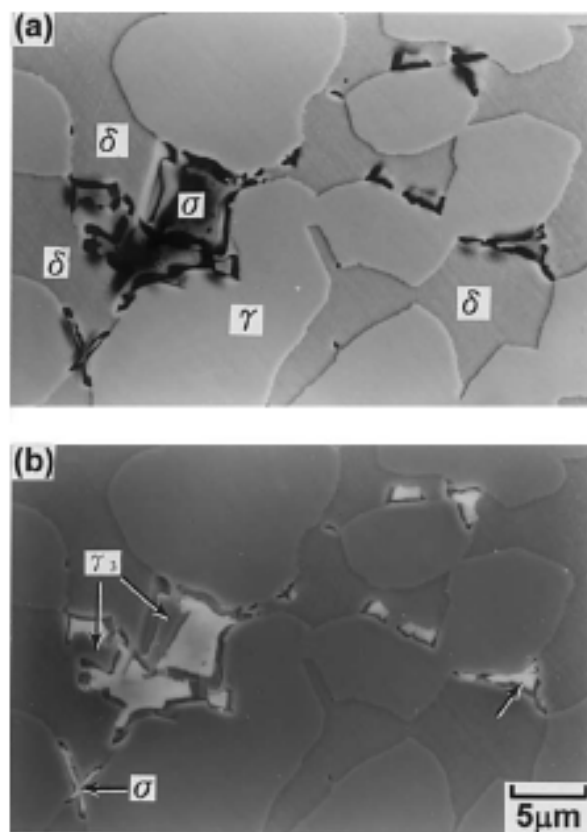


Figure A.4: Scanning electron micrographs showing σ phase located at the δ/γ interface, (a) SE and (b) BS images (electrolytically etched in 10 NNaOH solution) [CHE 01].

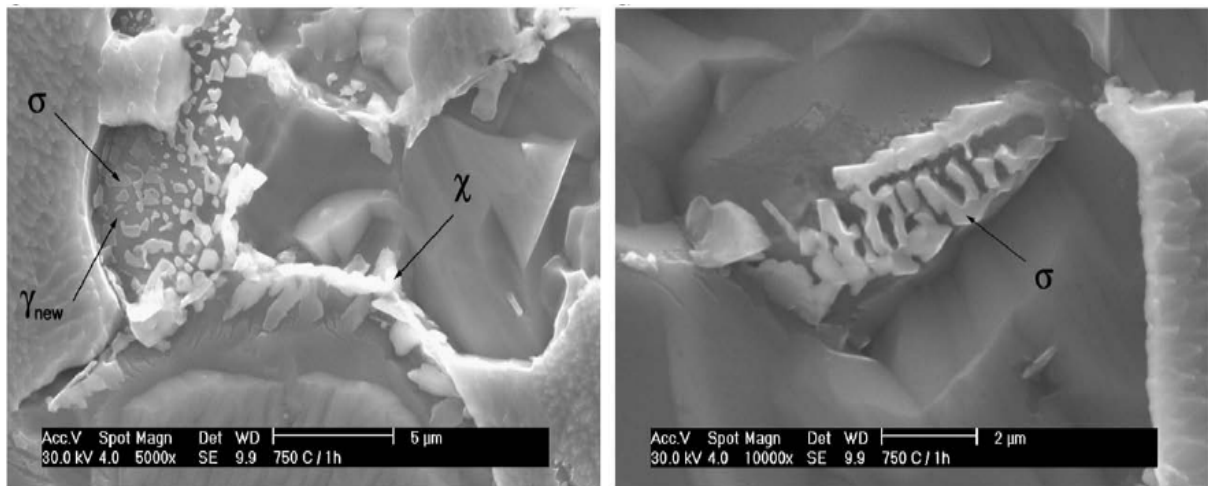


Figure A.5: SEM micrographs of the DSS after aging at 750 °C for 1 h. Etching: V2A-Beize [ESC 09].

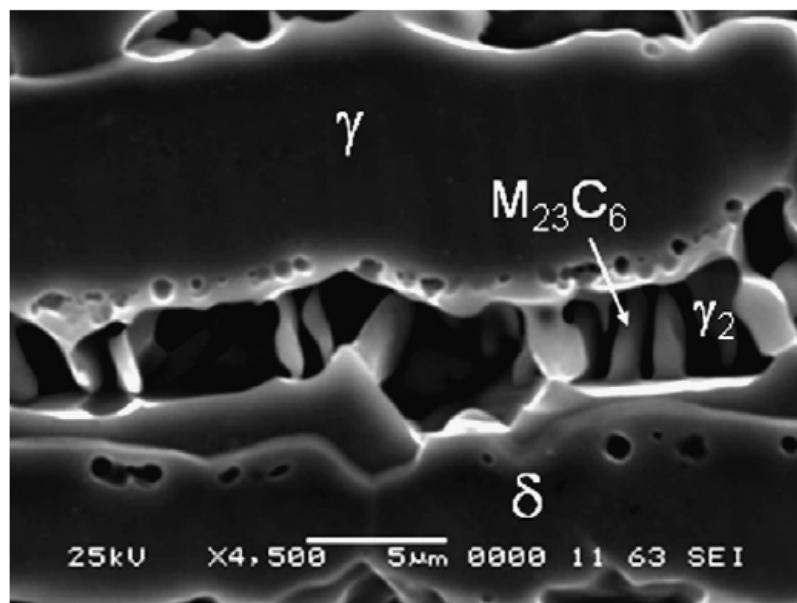


Figure A.6: SEM micrograph of HAZ solution treated at 1150 °C for 1 h then aged at 850 °C for 3 h [BAD 08].

A.3. Typical pitting morphologies of DSS after corrosion test:

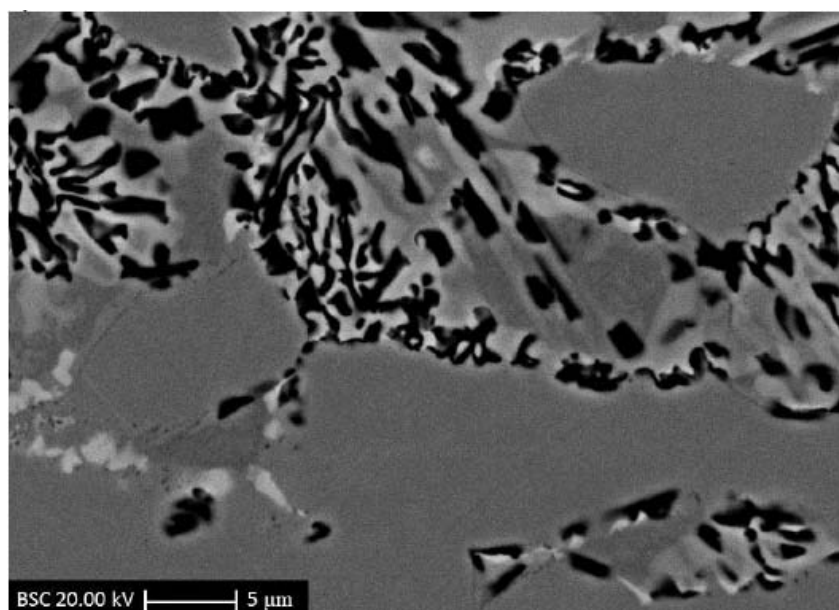


Figure A.7: Typical pitting morphologies of UNS S31803 DSS after polarization at 0.6M NaCl solution, aged for 6h@750°C [SAN 14].

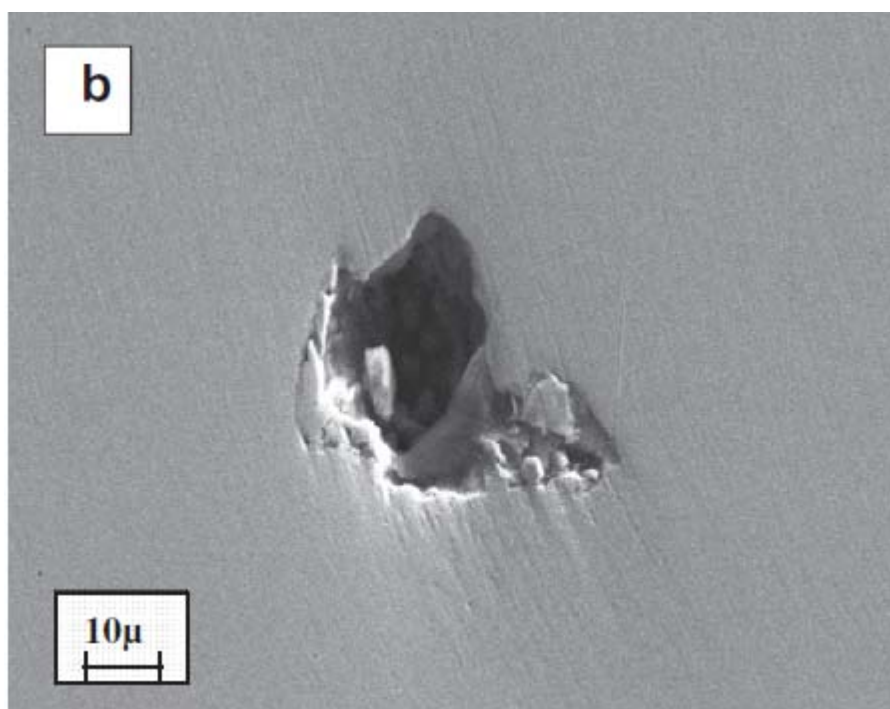


Figure A.8: Pit morphology of DSS 2205 after corrosion test in 0.1 M NaCl + 0.01 M MoO_4^{-2} at 80 °C [EGH 11].

ملخص

تم استخدام الفولاذ المقاوم للصدأ (DSS) على نطاق واسع في مختلف القطاعات الصناعية بسبب قوته العالية ، وقابلية اللحام الأفضل ، والمقاومة العالية للتآكل الناتج عن الإجهاد والحفر. ومع ذلك ، فإن تكوين أطوار معدنية بينية خطيرة مثل سيغما (σ) والتي تحدث في درجات حرارة تتراوح بين 600-1000 درجة مئوية والتقصف الحراري عند درجات حرارة متوسطة (~ 475 درجة مئوية) عبر فصل الطور ' α - α ' تحد من درجات حرارة الخدمة العليا لـ DSS في العديد من التطبيقات.

الغرض الرئيسي من هذا العمل هو التحقيق في سلوك التآكل الذي يحدث للفولاذ المقاوم للصدأ (DSS) عند تعريضه لبيئتين مختلفتين من الكلوريد: محلول محاكي لماء البحر ومحلول الماء المنتج. تم استخدام الفحوصات المعدنية جنباً إلى جنب مع تقنية حيود الأشعة السينية لمتابعة تطور البنية المجهرية. لقد ثبت أن DSS المعالج بمحلول يظهر مقاومة عالية للتآكل في كلا حل المحلولين ، في حين يحدث تدهور خطير في خصائص التآكل في وجود طور سيغما. لقد تم التوصل إلى أن كلاً من مقدار طور سيغما وتركيز الكلوريد يؤديان إلى تفاقم احتمال الحفر . أظهرت مراقبة SEM أن التآكل يحدث بشكل تفضيلي في انحاء طور سيغما بسبب تطور المناطق التي استنفد فيها عنصري الكروم والموليبدان. تم التأكد أيضاً على أن سلوك الصلابة يتأثر فقط بالعينات التي تم تعريضها لمعالجة حرارية لفترات طويلة.

تمت دراسة حركية عملية التقصف الحراري المرتبطة بفصل طور α - α أيضاً في الدراسة الحالية باستخدام تقنية DSC مقترنة بتحليل كينسجر. تم استخدام طاقة التنشيط التي تحكم عملية التقصف كأداة للتنبؤ من خلال نموذج JMA لتقدير نهاية عمر مكونات DSS التي تعمل في درجات حرارة متوسطة.

كلمات مفتاحية: الفولاذ المقاوم للصدأ (DSS) ، سيغما، الصدأ، محلول محاكي لماء البحر، الماء المنتج.

Abstract

The Duplex Stainless steels (DSS) have been widely used in various industrial sectors due to their higher strength, better weldability, and higher resistance to stress corrosion and pitting. However, the formation of dangerous intermetallic phases such as sigma (σ) which occurs at temperatures between 600-1000°C and the thermal embrittlement at intermediate temperatures (~475°C) via α - α' phase separation limit the upper service temperatures of DSS for many applications.

The main purpose of this work is to investigate the pitting corrosion behavior of sigmatized duplex stainless steel (DSS) exposed to two different chloride environments: simulated seawater solution and produced water solution. . The sigmatized samples were obtained by aging treatment at 850°C during various holding times to introduce varied levels of sigma phase. The microstructural evolutions after ageing were examined and the kinetic of sigma phase has been studied through the simplified and the modified JMA model.

It was established that solution treated DSS shows a high pitting corrosion resistance in both test solutions, while serious deterioration of corrosion properties occurs in presence of sigma phase. It was concluded that both sigma phase amount and chloride concentration worsen the pitting potential, the higher sigma content, the lower pitting potential and the higher chloride concentration, the lower pitting potential. SEM observation showed that pitting nucleation occurs preferentially at sigma phase interfaces due to the development of Cr- and Mo-depleted regions around sigma phase. It was also confirmed that the hardness behavior is only affected for long term aged samples.

The kinetic of thermal embrittlement process associated with α - α' phase separation was also investigated in the current study using DSC technique coupled with Kissinger analysis. The activation energy governing the embrittlement process has been used as "Prediction Tool" through the JMA model to estimate the end of life of DSS components operating at intermediate temperatures.

Key words: Duplex Stainless Steels (DSS), Sigma, Pitting Corrosion, Simulated Seawater, Produced Water.

Résumé:

Les aciers inoxydables duplex (DSS) ont été largement utilisés dans des divers secteurs industriels en raison de leur résistance supérieure, de leur meilleure soudabilité et de leur résistance à la corrosion sous contrainte et aux piqûres. Cependant, la formation de phases intermétalliques dangereuses telles que sigma (σ) qui se produit à des températures comprises entre 600 et 1000 ° C et la fragilisation thermique à des températures intermédiaires (~ 475 ° C) via la démixtion de phases α - α' limitent les températures maximales de service des DSS dans de nombreuses applications.

L'objectif principal de ce travail est d'étudier le comportement à la corrosion par piqûre de l'acier inoxydable duplex (DSS) vieillis exposé aux deux environnements de chlorure différents: une solution d'eau de mer simulée et une solution de l'eau produite. Les échantillons sigmatisés ont été obtenus par traitement de vieillissement à 850 ° C pendant divers temps de maintien pour introduire des taux variés de phase sigma. Les évolutions microstructurales après vieillissement ont été examinées et la cinétique de la phase sigma a été étudiée à travers le modèle de JMA simplifié et JMA modifié.

Il a été établi que le DSS hypertrempé présente une résistance élevée à la corrosion par piqûre dans les deux solutions d'essai, alors que les propriétés de corrosion se détériorent sérieusement en présence de la phase sigma. Il a été conclu que plus la teneur en sigma plus élevée, plus que le potentiel de piqûre est plus faible et de même pour la concentration en chlorure. Les observations par le MEB ont montré que la nucléation des piqûres se produisent préférentiellement aux interfaces de la phase sigma en raison du développement de régions appauvries en Cr et Mo autour de la phase sigma. Il a également été confirmé que la dureté n'est affectée que pour les échantillons vieillis à long terme.

La cinétique du processus de fragilisation thermique associée à la séparation des phases α - α' a été également examinée dans la présente étude en utilisant la technique DSC couplée avec l'analyse de Kissinger. L'énergie d'activation régissant le processus de fragilisation a été utilisée comme «outil de prédiction» à travers le modèle JMA pour estimer la durée de vie des composants DSS fonctionnant à des températures intermédiaires.

Mots clés: Acier inoxydable duplex (DSS), sigma, corrosion par piqure, l'eau de mère simulée, l'eau produite.